THE UNIVERSITY OF CHICAGO

DIRECT DETECTION OF HARMONIC GRAVITATIONAL WAVES FROM GALACTIC COSMIC STRING LOOPS

A DISSERTATION SUBMITTED TO
THE FACULTY OF THE DIVISION OF THE PHYSICAL SCIENCES
IN CANDIDACY FOR THE DEGREE OF
DOCTOR OF PHILOSOPHY

DEPARTMENT OF PHYSICS

BY
ZIMU LI

CHICAGO, ILLINOIS
JUNE 2020

To Jing and our Little Midou.

Out of Tao, One is born;

Out of One, Two;

Out of Two, Three;

Out of Three, the created universe.

The created universe carries the yin at its back and the yang in front;

Through the union of the pervading principles it reaches harmony.

– Lao-Tze "Tao Te Ching"

(Lin Yutang Translation, 1948)

TABLE OF CONTENTS

LIST OF FIGURES

LIST OF TABLES

ACKNOWLEDGMENTS

I would like to first and foremost offer my sincere gratitude to my advisor, Professor Craig J. Hogan, for offering his profound insight, unrelenting patience, and deep compassion that have propelled me to overcome formidable obstacles one after another throughout the process of bringing this project to fruition. Should future advancement in our understanding of quantum gravity bring us the technology of turning back time, one of the first things I will do with it is to make sure that I would meet Professor Hogan earlier during my time at the University of Chicago.

I would like to offer my heartfelt appreciation to the rest of my thesis committee, Professor Daniel E. Holz, Professor Paolo Privitera, and Professor LianTao Wang, for offering constructive comments, uplifting encouragement, and most importantly, inspiring and stimulating questions which have ceaselessly motivated me to strive for continual improvement.

Last but not least, I owe immeasurable gratitude to my wife, Jing, whose support both physical, mental, and spiritual, has been the pivotal stabilizing force at a time when both my inner and the outer worlds appear to be in a state of great turmoil.

ABSTRACT

Rapid advancement in the observation of cosmic strings has been made in recent years placing increasingly stringent constraints on their properties, with $G\mu \lesssim 10^{-11}$ from Pulsar Timing Array (PTA). Cosmic string loops with low string tension clump in the dark matter halo of the Galaxy due to slow loop decay and low gravitational radiation recoil, resulting in great enhancement to loop abundance in the Galaxy. The power of gravitational wave emission from loops is dominated by harmonic modes spanning a wide angular scale. Loops located in proximity to the solar system are powerful, persistent, highly monochromatic sources of gravitational waves with a harmonic signature not replicated by any other sources, making them prime targets for direct detection by the upcoming Laser Interferometer Space Antenna (LISA), whose frequency range is well-matched. At $G\mu = 10^{-20}$, there can be more than 10^8 loops contained in a narrow LISA frequency bin $\Delta f \sim 3 \times 10^{-8}$ Hz, with an average separation of just a fraction of a kpc at solar system orbit. Unlike burst signal detection where detection rate simply scales with loop abundance, detection rate for harmonic signal is the result of a complex interplay between strength of gravitational wave emission by a loop, loop abundance, and other sources of noise, and is best investigated through numerical simulations. We develop a robust and flexible framework for simulating cosmic string loops in the Galaxy for the purpose of predicting direct detection of harmonic signal from resolved loops by LISA. Our simulations reveal that the most accessible region in the parameter space for direct detection consists of large loops $\alpha = 0.1$ with low string tension $10^{-21} \lesssim G\mu \lesssim 10^{-19}$. Direct detection of field theory strings by LISA is unlikely, with the probability for detection $\lesssim 10\%$ under best circumstances, and $\lesssim 2\%$ with a more conventional configuration. Extension of our results predicts that direct detection by LISA of cosmic superstrings with low intercommutation probability is very promising, even unavoidable with optimal parameters. Searching for harmonic gravitational wave signal from resolved cosmic string loops in the Galaxy through LISA observation will place physical constraints on string theory.

CHAPTER 1

INTRODUCTION

1.1 Creation of Cosmic Strings

The Standard Model of particle physics consists of gauge theories where at high energy, the associated gauge fields exhibit the full SU(3)×SU(2)×U(1) gauge symmetry. Low energy physics at energy scales commonly found in the universe today, however, does not exhibit this full symmetry. In order to transition from the full field theory at high energy to the effective field theory that describes low energy physics, gauge symmetries exhibited by the former must be broken. The key mechanism in the Standard Model which enables this transition is through the process of spontaneous symmetry breaking (SSB) of high energy gauge symmetries as the energy scale of the theory is lowered.

SSB is achieved by incorporating a nonzero potential term into the Lagrangian of the full theory corresponding to the symmetry breaking energy scale. At energy scales much higher than the symmetry breaking scale, this additional potential has no effect, and the full symmetry of the high energy theory remains intact. When the energy scale falls below the symmetry breaking scale, the additional potential term shifts the minimum of the field, i.e. the field develops a vacuum expectation value. With this vacuum expectation value, the Lagrangian of the field is rewritten to describe motion of the field about this new minimum, which automatically becomes the Lagrangian of the low energy effective field theory without the symmetry exhibited by the high energy field theory above symmetry breaking scale. Through this process, the symmetry exhibited by the high energy field theory is "spontaneously" broken as the energy scale transitions below the symmetry breaking scale.

We can illustrate a good picture of the process of SSB and the associated production of effectively one-dimensional (1D) topological defects by presenting the simplest example[2] where a U(1) global symmetry is spontaneously broken, by inserting the potential η into the

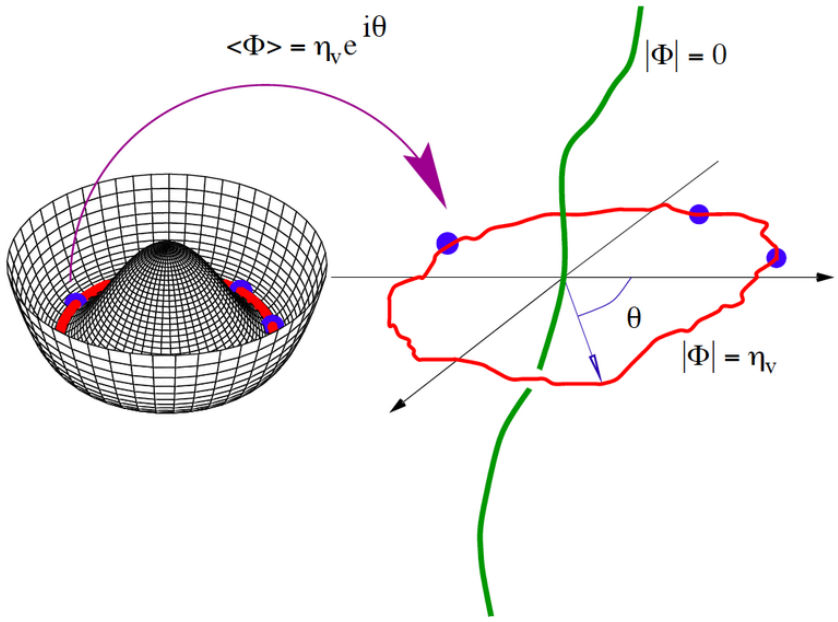

Figure 1.1: Schematic diagram of the SSB of U(1) symmetry. The left panel displays the low energy effective potential after SSB. The right panel displays the resultant creation of a 1D topological defect. Figure from ref. [1].

Lagrangian of a field exhibiting U(1) global symmetry, i.e. a ϕ^4 theory,

$$\mathcal{L} = |\partial_\mu \phi|^2 - \frac{\lambda}{4}(|\phi|^2 - \eta^2)^2. \tag{1.1}$$

At energy scales much higher than η, this additional potential in the Lagrangian can simply be ignored, and we just have a ϕ^4 theory with global U(1) symmetry oscillating about the minimum $\langle\phi\rangle_{\rm h} = 0$. As the energy scale of the field is lower to below η, this additional term in the Lagrangian becomes important, and the minimum of the field is no longer at $\langle\phi\rangle_{\rm h} = 0$. The field settles into the new minimum developing a vacuum expectation value $|\langle\phi\rangle_{\rm l}| = \eta$, meaning that

$$\langle\phi\rangle_{\rm l} = \eta e^{i\theta}. \tag{1.2}$$

The phase θ can take on any value without affecting $|\langle\phi\rangle_{\rm l}| = \eta$, and therefore the potential now has a shape similar to that of a Mexican hat, with a ring of minima, as shown in the

left panel of the schematic diagram[1] fig. 1.1.

The interesting feature to notice from the simple example of spontaneously breaking the global U(1) symmetry in a ϕ^4 theory is the fact that the phase θ acquired by the vacuum expectation value of the field eq. 1.2 is arbitrary, and therefore should be different for uncorrelated parts of the field as dictated by causality. This means that around a central point, the vacuum expectation value acquired by the field at various uncorrelated angular locations after SSB should have different values of θ. Then the only way that the field can remain well-defined at the central point is for it to retain $\langle\phi\rangle = 0$, the minimum of the high energy field theory, as can be seen from the right panel of the schematic diagram[1] fig. 1.1. The collection of such points then forms an effectively 1D object retaining the symmetry breaking energy which is higher than that of low energy physics. This is an example of a 1D topological defect created by the SSB process. These objects are not purely theoretical constructs, and for example, have been produced during phase transition of liquid crystals[8].

Just as in the case of the SSB of a global symmetry described above, SSB of a gauge symmetry can also create topological defects[2]. The most common example is a scalar field theory with U(1) gauge symmetry which is spontaneously broken by the addition of the Higgs potential[1],

$$\mathcal{L} = \frac{1}{2}|D_\mu\Phi|^2 - \frac{1}{4}H_{\mu\nu}H^{\mu\nu} - \frac{\lambda}{8}(|\Phi|^2 - \eta^2)^2, \tag{1.3}$$

with the gauge derivative

$$D_\mu = \partial_\mu + igB_\mu. \tag{1.4}$$

At energy scales below η, the U(1) gauge symmetry of the scalar field is broken, and a 1D topological defect is created with energy per unit length[1]

$$\mu = C\left(\frac{\lambda}{g^2}\right)\eta^2, \tag{1.5}$$

where $C\left(\frac{\lambda}{g^2}\right) \sim \mathcal{O}(1)$ is the winding number which depends only on coupling strengths.

In fact, in general the SSB of a higher symmetry to a lower symmetry $\mathcal{G} \to \mathcal{H}$ generates $(2-n)$-dimensional topological defects if the nth homotopy group is nontrivial $\pi_n(\mathcal{M}) \neq I$, where $\mathcal{M} = \mathcal{G}/\mathcal{H}$ is the vacuum manifold[2]. This means that 1D topological defects are created as a result of the SSB if $\mathcal{M}$ is not simply connected. For fields in the universe, we immediately see that such 1D topological defects must be either in loops or infinitely long.

In the cosmological context, such 1D topological defects can be produced at the end of inflation when the energy scale of the universe drops very rapidly[2, 1]. The energy density of 1D topological defects created from SSB of a gauge symmetry decreases exponentially away from the core[2], with the length-scale depending on coupling strengths. However, this thickness is negligible compared to cosmological length-scales, and therefore these can be treated as 1D objects and are called cosmic strings. Causality dictates that the correlation length-scale of the field undergoing SSB, $L(t)$, must be less than the horizon

$$L(t) \lesssim t. \tag{1.6}$$

Thus, infinite cosmic strings are naturally created in the universe. This process is called the Kibble mechanism[9]. From the energy per unit length of a field theory string eq. 1.5, we see that cosmic strings have tension

$$G\mu \sim \left(\frac{\eta}{m_{\rm pl}}\right)^2, \tag{1.7}$$

where $m_{\rm pl}$ is the Planck mass.

An interesting coincidence is the fact that if one assumes that the presence of cosmic strings is responsible for primordial density perturbation in the universe, and therefore seeding large-scale structure formation in the universe, the required string tension actually corresponds to the Grand Unified Theory (GUT) energy scale $G\mu \sim 10^{-6}$[2, 10, 1, 11]. However, the expected perturbation spectrum does not agree with the observed spectrum of temper-

ature fluctuations of the Cosmic Microwave Background (CMB)[1]. Moreover, this string tension has long been ruled out by various direct and indirect observations constraining cosmic strings, from CMB anisotropy[12, 13], microlensing of stars and galaxies[14, 15, 16, 17], Big Bang Nucleosynthesis (BBN)[18, 19], Pulsar Timing Array (PTA)[20, 21], and ground-based interferometer gravitational wave observatories[22, 23].

Alternatively, macroscopic string-like objects can be created as F-strings and D1-strings at the end of various brane inflation scenarios under the framework of string theory[24]. While these objects arise from a very different theoretical origin from that of cosmic strings produced by field theories, the former can be studied and constrained with astrophysical observations in a similar fashion to that of the latter. Due to the richness of the string theory framework, there really is very little theoretical restriction on the characteristics of such cosmic superstrings.

Cosmic string loops much smaller than the horizon are created as a result of intercommutation of infinite strings[2]. In fact, we can see that as 1D infinite objects which stretch with cosmic expansion, the energy density of infinite strings is only diluted by $\rho_\infty \propto a(t)^{-2}$. This means that the total energy of infinite strings grows with cosmic expansion $E_\infty \propto a(t)$. Infinite strings will therefore quickly dominate the universe without a mechanism for losing energy. Loop formation is the dominant energy loss mechanism for the infinite string network in the universe[2, 25].

1.2 Direct Observation of Cosmic Strings

Other topological defects such as domain walls and monopoles can also be created as results of SSB[2]. However, they easily run into conflict with various observations without extensive and unnatural fine tuning[2, 1]. They are therefore most likely created before inflation and hence are no longer relevant today. In fact, part of the purpose of inflation is exactly to inflate away undesirable topological defects created from SSBs during the very early

universe[26, 27, 28]. Cosmic strings on the other hand, are naturally created at the end of inflation[2, 1, 24] and can easily be made compatible with all current observations[24], making their existence in the universe a very real possibility. Thus, instead of being avoided like other topological defects, cosmic strings are essentially natural relics of the early universe likely to still be in existence today, whose characteristics should be studied and constrained with observations.

We can see from eq. 1.7 that cosmic strings are objects which preserve the physics at the much higher SSB energy scale. They therefore serve as a window through which one can get a direct glimpse at the high energy theory describing physics far beyond the energy scale accessible to us through colliders today. Or, cosmic strings can be macroscopic remnants created directly from string theory, as we discussed previously. Detecting cosmic strings can therefore open a gateway towards understanding new physics beyond the Standard Model.

As massive objects moving at relativistic velocities[2], cosmic strings are powerful sources of gravitational waves in the universe. Detecting their gravitational wave emission is therefore an important method for the direct observation of cosmic strings. Both cosmic string loops and the infinite string network emit gravitational waves. But the dominant emission comes from cosmic string loops smaller than the horizon[2, 29]. Gravitational waves are emitted from vibrational modes of a loop, with the frequency of the fundamental mode simply determined by the size of the loop.

The possibility of detecting the unresolved stochastic background from the collective emission of gravitational waves from all cosmic string loops in the universe over all time has been studied extensively in the literature, and considerable progress on constraining the string tension has been made recently[29], with the current constraint $G\mu \lesssim 10^{-11}$ coming from PTA observations[21]. For the upcoming space-based gravitational wave observatory, the Laser Interferometer Space Antenna (LISA)[5, 6, 30], the recent comprehensive study in the work of ref. [29] has concluded that LISA can detect the stochastic background from

cosmic string loops down to at least $G\mu \sim 10^{-17}$.

Cosmic string loops with such low string tension have weaker gravitational wave emission and therefore decay very slowly. Such long lived loops have the potential to survive to the present time without being significantly affected by loop decay, while they also have had time for their originally relativistic velocity at creation to be essentially damped away by cosmic expansion[2, 4]. An interesting implication then arises, that these loops which already have high abundance in the universe due to slow loop decay, should clump in the dark matter halo of the Galaxy more or less following the dark matter density profile[14, 31, 4]. Loop clumping results in a significant enhancement of loop abundance in the dark matter halo of the Galaxy, estimated to be at least by a factor of 10^5[14, 4, 11]. Thus, detecting gravitational waves emitted by loops currently present in the Galaxy could be an even more promising approach to directly observing cosmic strings than trying to detect the stochastic background consisting of gravitational waves emitted by very distant loops distributed across the universe throughout its history.

For cosmic string loops that have clumped in the Galaxy, the ones with gravitational wave emission at very low frequency in the PTA frequency range have lower abundance, because they are larger loops which are created later in time, when the horizon is larger. On the other side of the spectrum, unless the string tension is very low $G\mu \lesssim 10^{-22}$, loops emitting gravitational waves at high frequency in the frequency range of ground-based interferometer gravitational wave observatories such the Laser Interferometer Gravitational-Wave Observatory (LIGO) have decayed significantly, and therefore also have low abundance. Loops which do have very low string tension $G\mu \lesssim 10^{-22}$ have very weak gravitational wave signal which also presents a challenge for LIGO-like ground-based gravitational wave observatories. The LISA frequency range and sensitivity are therefore very well suited for further extending observational bounds on cosmic strings by observing loops that have clumped in the Galaxy.

While the total unresolved gravitational wave signal from loops in the Galaxy forms

the Galactic background which adds to the stochastic background from loops, the more interesting prospect raised by the clumping of cosmic string loops and the resultant high abundance of loops in the Galaxy is the possibility of direct detection of gravitational waves from individual loops, essentially direct observation of single loops. In addition to the direct discovery of cosmic string loops such a detection will entail, the stronger signal from such loops over the Galactic and the stochastic backgrounds can enable deeper probes into the characteristics of cosmic strings. These are true soloists in this grand cosmic symphony surrounding us. By listening to these soloists piercing through the background directly, we may gain a better understanding of cosmic strings themselves.

There are two approaches for attempting to resolve gravitational wave signal from individual loops. One can try to resolve highly beamed high frequency gravitational wave bursts emitted by small-scale features on the loops such as cusps and kinks[2, 32, 33]. Here, the rate of detection clearly just scales with loop abundance in the Galaxy. The possibility for detection of such burst signals from cosmic string loops in the Galaxy has been estimated theoretically in the work of ref. [11].

The alternative approach first proposed by ref. [31] but has never been explored in detail before takes advantage of the high loop abundance in the Galaxy in a different way. We note that due to clumping of loops in the Galaxy, at $G\mu = 10^{-20}$, even considering loop ejection from the Galaxy due to recoil caused by anisotropy in gravitational wave emission by loops[4], there can be more than 10^8 loops in the Galaxy emitting harmonic gravitational waves in just one narrow LISA frequency bin $\Delta f = 1/T_{\rm obs} \sim 3 \times 10^{-8}$ Hz for a one-year mission, in the sensitive region of the LISA frequency range $10^{-3} \lesssim f \lesssim 10^{-1}$ Hz. The expected distance from the solar system to the closest such loop emitting harmonic gravitational waves in just one narrow frequency bin is then just a fraction of a kpc. This raises the prospect that some loops may be located in extreme proximity to the solar system, that the low frequency harmonic modes of their gravitational wave

emission can overwhelm all other sources of gravitational waves and be detected directly. Such harmonic gravitational waves are persistent, highly monochromatic, emitted over a wide angular scale, and dominant over the total power of gravitational wave emission by loops, while carrying the unmistakable harmonic signature that can differentiate them from other sources of gravitational waves. In the Fourier transform of the LISA strain signal, this harmonic signature of low frequency gravitational wave emission from loops will appear as tall spikes towering over the background at frequencies that are exact integer multiples of the fundamental frequency. Such functional forms of the signal are not replicated by signal from any other source of gravitational waves, including other persistent and monochromatic sources such as white dwarf (WD) binaries in the Galaxy, and therefore make them extremely easy to search for in the LISA signal. Cosmic string loops in the neighborhood of the solar system are therefore highly tantalizing targets for LISA. Unlike in the case of burst signal detection where the event rate is simply proportional to loop abundance in the Galaxy[11], detection of harmonic signal from individual loops relies on loops being located sufficiently closely to the solar system in relation to other loops in the Galaxy, and the detection rate is the result of a complex interplay between the strength of gravitational wave emission from a loop, loop abundance in the Galaxy, and fixed sources of noise such as LISA instrumental noise. Thus, detection of harmonic signal from individual loops is best understood through numerical simulations. The objective of this study is to explore the possibility of directly detecting harmonic gravitational wave signal from nearby individual cosmic string loops in the Galaxy through numerical simulations of loops in the Galaxy.

We organize the rest of this manuscript in the following order. After introducing cosmic strings and the observation of their gravitational wave emission in this chapter, in chapter 2, we continue our introduction of theoretical background behind this study, focusing on those aspects which make direct contribution to and are essential for comprehending the meaning and significance of this study. We develop the framework and all the methodologies necessary

for performing the numerical simulations in our study by analyzing toy models in chapter 3, where we are able to make predictions on the expectation of results from simulating cosmic string loops in the physical Galaxy based on results from simulations of toy models. In chapter 4, we present results from simulations of the physical Galaxy. We conclude in chapter 5, and discuss some implications of our results as well as potential extension for future studies.

CHAPTER 2

THEORETICAL BACKGROUND

2.1 Cosmic String Loop Formation

2.1.1 The One-Scale Model

Motion of cosmic strings in the network of infinite strings formed in the early universe as discussed in chapter 1 on superhorizon scales is effectively frozen, and the network stretches with the expansion of the universe. On subhorizon scales, the infinite string segments move freely, and therefore their movements can be characterized as Brownian motion in space[2]. This subhorizon motion gives rise to the possibility of collisions between segments of infinite strings. When string segments collide, there is a probability $P_{\rm int}$ that they intercommute. Canonical cosmic strings formed as a result of SSB of a gauge field are basically always assumed to have $P_{\rm int} = 1$. This is especially true when an U(1) gauge symmetry is broken, which is almost always thought to be the case in the various formation scenarios of cosmic strings in the field theory framework[2, 29]. Cosmic superstrings arising from various brane inflation scenarios can have much lower $P_{\rm int}$[24]. In this work, we adopt canonical Nambu-Goto cosmic strings formed in the field theory framework with $P_{\rm int} = 1$. Discussions concerning other models of cosmic strings can be found in chapter 5. Intercommutation of

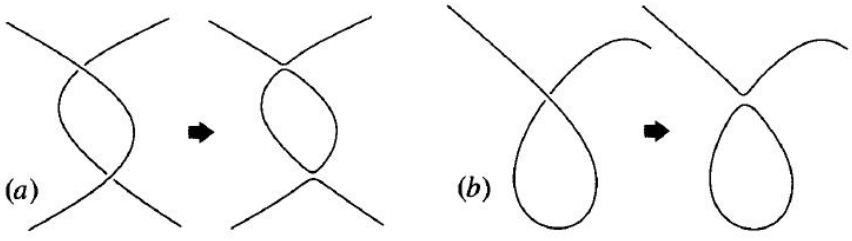

Figure 2.1: Schematic diagrams of the two simplest possible scenarios of cosmic string loop formation as a result of intercommutation of infinite string segments. A loop is created by (a) two infinite strings intercommuting at two points; (b) an infinite string intercommuting with itself. Figure from ref. [2].

cosmic string segments gives rise to the possibility of loop formation. This can happen e.g. when a point on an infinite string intercommutes with another point on the same infinite string, or when two infinite strings intercommute at two points, as illustrated by schematic diagrams[2] in fig. 2.1.

The basic idea that the entire process of cosmic string loop formation, including evolution of initial loop sizes, loop formation rates, energy density of the infinite string network, converges to a scaling solution with respect to the cosmic horizon originates from Kibble[34]. This elegant idea called the one-scale model essentially dictates that given physical quantities such as $G\mu$ and P_{int}, there really is just one phenomenological free parameter in the model called the chopping efficiency c which encapsulates effects of all physical processes involved in the eventual loop creation from a potentially complex series of cosmic string intercommutations, for an overall efficiency of loop formation by "chopping" infinite strings[29].

We now present a simple argument outlining the theoretical motivation behind the one-scale model[2]. Collisions between segments of infinite strings occur at the characteristic length-scale of the infinite string network $L(t)$, which is a function of time as the infinite string network is stretched by cosmic expansion. Then when considering only the effect of cosmic expansion, comparing with some reference initial time t_i, the characteristic length-scale

$$L(t) \sim \frac{a(t)}{a(t_i)} L_i. \tag{2.1}$$

Differentiate,

$$\frac{dL(t)}{dt} = \frac{\dot{a}(t)}{a(t)} L(t) = H(t)L(t). \tag{2.2}$$

The energy density of the infinite string network in the characteristic volume is

$$\rho_\infty = \frac{E_\infty}{L^3} = \frac{\mu L}{L^3} = \frac{\mu}{L^2}. \tag{2.3}$$

Differentiate, we have

$$\left.\frac{d\rho_\infty}{dt}\right|_{\text{exp}} = -2\frac{dL}{dt}\frac{\mu}{L^3} = -2H(t)\rho_\infty. \tag{2.4}$$

This is the loss in the energy density of the infinite string network due to dilution by cosmic expansion. On average, a string segment travels L before colliding with another string segment, and therefore the collision rate is just $\frac{1}{L}$. The loss in energy density of the infinite string network due to loop formation is then

$$\left.\frac{d\rho_\infty}{dt}\right|_{\text{loop}} = -\frac{\rho_\infty}{L}. \tag{2.5}$$

Combining eqs. 2.4 and 2.5, the total loss in the energy density of the infinite string network is

$$\frac{d\rho_\infty}{dt} = -2H(t)\rho_\infty - \frac{\rho_\infty}{L}. \tag{2.6}$$

To motivate a scaling solution with the horizon, define $L(t) \equiv \gamma(t)t$, and eq. 2.6 for the radiation era $a(t) \propto \sqrt{t}$ can be written as

$$\frac{\dot{\gamma}}{\gamma} = -\frac{1}{2t}\left(1 - \frac{1}{\gamma}\right). \tag{2.7}$$

Clearly, $\dot{\gamma} > 0$ when $\gamma < 1$ and $\dot{\gamma} < 0$ when $\gamma > 1$. Thus, the differential equation has a stationary solution $\gamma(t) = 1$, i.e. we have a scaling solution with respect to the horizon

$$L \sim t. \tag{2.8}$$

Comparing eqs. 2.1 and 2.8, we see that $L(t)$ now grows faster than when being stretched by cosmic expansion alone, due to loop formation. The scaling of the characteristic length-scale with the horizon is significant as this is the length-scale of colliding infinite string segments, which determines initial sizes of cosmic string loops created. Thus, the solution eq. 2.8

motivates a scaling solution of the initial sizes of loops created with the horizon. As we will see below, the loop formation rate for a given initial loop size is determined by ρ_∞, and therefore it is also a scaling solution.

The network of infinite strings have always been assumed to predominantly lose energy through loop production based on theoretical grounds[2], and this assumption has also been confirmed by numerical simulation[25]. Then the full differential equation governing its evolution[29] takes a very similar form to that derived heuristically above, eq. 2.6,

$$\frac{d\rho_\infty}{dt} = -2H(t)\left(1+\bar{\nu}^2\right)\rho_\infty - \mu\int_0^\infty l f(l,t)dl, \tag{2.9}$$

where $\bar{\nu}$ is the root-mean-squared velocity of the string segments, and $f(l,t)$ is the distribution of loop production function. For the simple one-scale model, $f(l,t)$ is a Dirac delta function, and eq. 2.9 reduces to

$$\frac{d\rho_\infty}{dt} = -2H(t)\left(1+\bar{\nu}^2\right)\rho_\infty - c\frac{\rho_\infty}{L}, \tag{2.10}$$

where c is the chopping efficiency discussed above. The conventional approach is to go ahead and solve the equation of motion eq. 2.9 or eq. 2.10, and obtain the distribution of number density $n(l,t)$ which already includes effects of cosmic expansion, and then integrate $\int_{l_i}^{l_{i+1}} n(l,t)dl$ to obtain the loop number density for a set of bins in loop sizes. This approach is necessary when the loop production function $f(l,t)$ includes a range of loop sizes. However, for the simple one-scale model, there is a much simpler method of obtaining the loop number density using arguments based on the characteristics of the scaling solution. This method essentially allows us to treat effects on loop number density due to loop production and cosmic expansion separately.

First we focus on loop production. The loss in energy density of the infinite string network

goes into string loop formation, and therefore from eq. 2.10,

$$\frac{d\rho_{\rm l}}{dt} \propto c\frac{\rho_\infty}{L}, \tag{2.11}$$

where $\rho_{\rm l}$ is the energy density of string loops. As we discussed above, ρ_∞ also reaches a scaling solution as can be seen from the heuristic argument eqs. 2.3 and 2.8, and this has been confirmed by simulations of string loop formation. The scaling solution is therefore[2]

$$\rho_\infty t^2 = \text{const.} \tag{2.12}$$

Then $\rho_\infty \propto t^{-2}$, and given that $L \propto t$ from eq. 2.8, eq. 2.11 means

$$\frac{d\rho_{\rm l}}{dt} \propto \frac{1}{t^3}. \tag{2.13}$$

This means that for the energy density of string loops, we also have

$$\rho_{\rm l} \propto \frac{1}{t^2}. \tag{2.14}$$

The total energy of string loops is

$$E_{\rm l} = \mu L_{\rm t} = \rho_{\rm l} t^3, \tag{2.15}$$

where $L_{\rm t}$ is the total length of string loops. Combine eqs. 2.14 and 2.15, and differentiate,

$$\frac{dL_{\rm t}}{dt} = \text{const.} \tag{2.16}$$

Or

$$\frac{dL_{\rm t}}{d\ln t} \propto t. \tag{2.17}$$

We see from eq. 2.17 that the total length of cosmic string loops produced in a Hubble volume over a log time interval scales with the horizon, meaning that in terms of the horizon, the total length is constant. The nice thing about this is that now the loop number density in log-scale of loop creation time $t_{\rm c}$ can be written down naturally with just an overall normalization. Incorporating effects of dilution due to cosmic expansion, the cosmic string loop number density is[35, 36]

$$n(t_{\rm c}, t) = \frac{l_{\rm t}}{\alpha} H(t_{\rm c})^3 \left(\frac{a(t_{\rm c})}{a(t)} \right)^3, \tag{2.18}$$

where $\alpha = \frac{l}{t}$ is the size of loops at formation in terms of the horizon, the overall normalization $l_{\rm t}$ is the total length of cosmic string loops in terms of the horizon created in a log creation time interval, t is the time of observation. To be consistent with previous studies, we adopt $l_{\rm t} = 8.111$ with the log binning in loop creation time $\Delta t_{\rm c} = 0.1 t_{\rm c}$[35, 36, 37, 38]. From eq. 2.11, we see that this normalization factor of the formation rate is really determined by c and ρ_∞. These quantities are obtained from numerical simulations and do not have arbitrary degrees of freedom for adjustment[2, 39].

We can confirm the scaling of our loop number density eq. 2.18 by comparing with results derived from the more traditional approach in refs. [2, 29]. To do this, we first set $l = \alpha t$ in their expressions to eliminate effects of cosmic expansion after loop formation. This is equivalent to setting $t_{\rm c} = t$ in eq. 2.18. Then we notice that their loop number densities in log bins $ln(l, t) \propto t^{-3}$, which is the same scaling as our loop number density eq. 2.18.

2.1.2 Initial Loop Sizes

The only parameter in eq. 2.18 left to be discussed is the scaling initial loop size α. Various attempts have been made in the literature to deduce the scaling solution of the initial loop size from numerical simulations. Very early simulations usually produced only very small

cosmic string loops bound by simulation resolutions[2, 40, 41, 42]. This continued until the problems caused by simulation resolutions were overcome by the works in refs. [43, 44, 45], where for the first time a physically meaningful loop production function was obtained. They conclude that the process of loop formation does indeed converge to scaling solutions, and is dominated by formation of very large loops with $\alpha \sim 0.1$. In fact, they observe that these big loops account for most of the length of loops created.

Gravitational wave emission causes smoothing of small-scale features on infinite strings on the gravitational backreaction length-scale $l_{\rm br} \sim \Gamma G\mu t$[44], where $\Gamma \sim 50$[35, 29] parametrizes the power of gravitational wave emission by cosmic strings and will be discussed in section 2.2.2. This should strongly suppress loop formation below the gravitational backreaction length-scale, $\alpha \lesssim \Gamma G\mu$. Later loop formation simulations [46, 25] have observed this cutoff for the formation of smaller loops, and in fact the scaling solution with the cutoff for the formation of small loops has been observed even without introducing gravitational radiation into the loop formation simulation[25]. We call simulations producing such distributions of initial loop sizes the big-loop paradigm.

A radically different approach is taken in the theoretical work of refs. [47, 48, 49] in deriving the loop production function, where the gravitational backreaction length-scale is also reduced. The loop formation simulation based on these theoretical results[50] produces a very different picture from those of the big-loop paradigm above. The gravitational backreaction length-scale is reduced to[50, 51] $l_{\rm br} \sim 20(G\mu)^{1+2\chi}$, with $\chi_{\rm r} = 0.200^{+0.07}_{-0.10}$ and $\chi_{\rm m} = 0.295^{+0.03}_{-0.04}$ for radiation and matter eras, respectively. The more important feature of this model is that with loop production functions derived in refs. [47, 48, 49], the loop formation simulation predicts that loop production is little affected by gravitational backreaction[50]. The overall loop production is still scaling with a similar cutoff for large loops, however the lack of a cutoff for small loops results in a great overabundance of very tiny cosmic string loops at formation compared to simulations in the big-loop paradigm. We

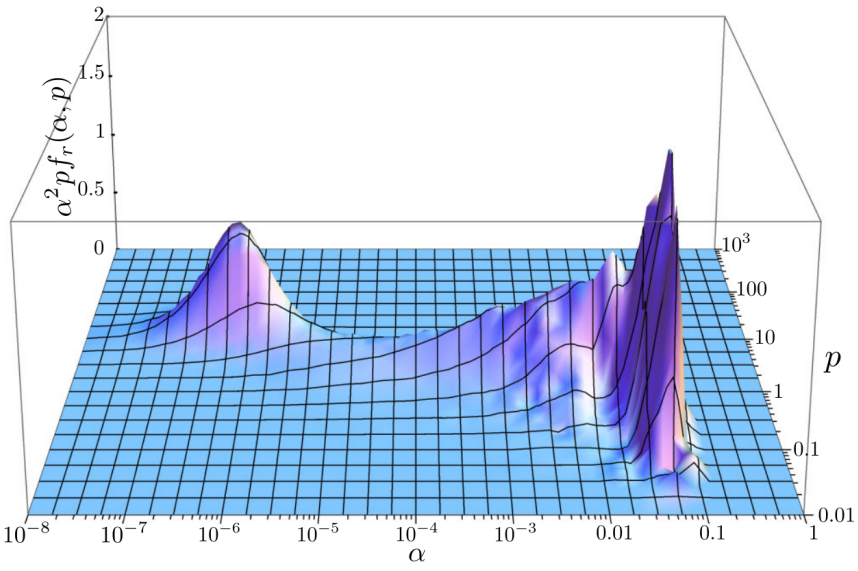

Figure 2.2: Cosmic string loop production in the radiation era from a recent loop formation simulation, where p is momentum per unit mass. Figure from ref. [3].

call this the small-loop paradigm.

The current most state-of-the-art loop formation simulations[52, 3] still produce a distribution of cosmic string loops from $\alpha \sim 0.1$ down to the gravitational backreaction scale $\alpha \sim \Gamma G\mu$. Result from a recent such simulation[3] is presented in fig. 2.2, where the small peak at $\alpha \sim 10^{-6}$ is said to be non-scaling. The most standard one-scale model of cosmic strings adopted by studies in the literature on detection of their gravitational waves has $\alpha \sim 0.1$[35, 31, 29]. For such studies, the important factor is actually not the distribution of initial loop sizes itself, but the fact that the scaling solution of cosmic string loop production has a cutoff for large loops at $\alpha \sim 0.1$. This is because these largest loops with $\alpha \sim 0.1$ essentially represent the best-case scenario for detecting gravitational waves from cosmic strings[29]. We will see in section 3.3.7 that at a given frequency, decreasing α actually decreases the loop number density despite α appearing in the denominator in eq. 2.18. The reason is that with a lower α, the loops emitting such gravitational waves are created later in time, with a reduced number density due to the larger horizon.

Additionally, comparing results in ref. [29], we see that the difference between gravita-

tional waves emitted by loops modeled by the simple one-scale model and those emitted by loops modeled by a full distribution of initial loop sizes obtained from the most recent loop formation simulation is not very significant. In particular, any difference mostly manifests in the high frequency flat region of the stochastic background, which for the values of string tension of interest in this study as we will discuss in section 3.3.8, exists outside of the LISA frequency range. We therefore adopt the simple one-scale model of cosmic string loop number density at formation eq. 2.18 with $\alpha = 0.1$ and $\alpha = 10^{-5}$ for our simulation. Results from the latter can help shed light on models with small cosmic string loops.

We can compare normalization factors in the loop number density of the simple one-scale model eq. 2.18 with those from the distribution of initial loop sizes produced by the most state-of-the-art loop formation simulation[3]. At $\alpha = 0.1$, their simulation produces a normalization factor of ~ 0.57 when binned the same way as eq. 2.18, while the normalization factor from eq. 2.18 is ~ 81. We see that the simple one-scale model overestimates the loop number density by two orders of magnitude at $\alpha = 0.1$. At $\alpha = 10^{-5}$, the comparison is between $\sim 5.7 \times 10^5$ and $\sim 8.1 \times 10^5$. The two models provide similar estimates of the loop number density at $\alpha = 10^{-5}$. This is in fact part of the reason $\alpha = 10^{-5}$ is also chosen for this study, as we will discuss in section 3.3.8 and chapter 5.

2.2 Gravitational Radiation from Cosmic String Loops

2.2.1 Loop Dynamics

As cosmic strings are effectively 1D objects with linear mass density μ, gravitational waves are emitted as a result of movements of string segments. Thus, some understanding of the motion of cosmic string loop segments is necessary in order to analyze gravitational radiation from these loops. Motion of an effectively 1D Nambu-Goto cosmic string loop traces out a worldsheet in spacetime, in analogy to the worldline traced out by the motion of a particle.

The dynamics of such a loop is governed by the Nambu-Goto action[2]

$$S = -\mu \int d^2\sigma \sqrt{-\gamma}, \tag{2.19}$$

where γ is the determinant of the worldsheet metric. When background spacetime is essentially flat, i.e. $\frac{l}{\mathcal{R}} \sim 0$, where $\mathcal{R}$ is the scale of curvature of background spacetime, and utilizing the transverse gauge, the Nambu-Goto action eq. 2.19 gives rise to the following equations of motion:

$$\dot{\mathbf{X}} \cdot \mathbf{X}' = 0; \tag{2.20}$$

$$\dot{\mathbf{X}}^2 + \mathbf{X}'^2 = 1; \tag{2.21}$$

$$\ddot{\mathbf{X}} - \mathbf{X}'' = 0, \tag{2.22}$$

where $\mathbf{X}(t, \sigma)$ is the trajectory of the loop parametrized by timelike and spacelike parameters t and σ, respectively. The first equation of motion eq. 2.20 means that the time derivative $\dot{\mathbf{X}}$ is always perpendicular to the tangent vector $\mathbf{X}'$, and is simply a consequence of the transverse gauge, and the reason this gauge is convenient for this purpose. This means that the time derivative $\dot{\mathbf{X}}$ can be interpreted as the physical velocity of the loop segment. The second equation of motion eq. 2.21 can be rewritten as

$$\frac{d\sigma}{|d\mathbf{X}|} = \frac{1}{\sqrt{1 - \dot{\mathbf{X}}^2}}. \tag{2.23}$$

With the discussion of the first equation of motion above, we recognize the right hand side of eq. 2.23 as simply the relativistic γ factor. Thus, the second equation of motion eq. 2.21 specifies conservation of energy. A simple expression of the total energy of the cosmic string

loop can be obtained by integrating eq. 2.23 around the loop,

$$E = \mu \oint \frac{|d\mathbf{X}|}{\sqrt{1-\dot{\mathbf{X}}^2}} = \mu \int d\sigma. \tag{2.24}$$

This expression means that in the transverse gauge, the spacelike parameter σ can be identified nicely as the length parameter along the loop. With the discussion of the first equation of motion above, the last equation of motion eq. 2.22 simply says that the acceleration of a string loop segment is proportional to its local curvature, in the direction which tends to reduce the local curvature. Thus, motion of the cosmic string loop tends to straighten curvature along the loop, which is a very intuitive behavior.

Trajectories of a cosmic string loop are obtained by solving the cosmic string equations of motion eqs. 2.20 through 2.22. The general solution consists of left- and right-moving components[2]

$$\mathbf{X}(t,\sigma) = \frac{1}{2}\left(\mathbf{X}_-(t-\sigma) + \mathbf{X}_+(t+\sigma)\right). \tag{2.25}$$

The only constraint on the general solution can be derived by expanding equations of motion eqs. 2.20 and 2.21 with the solution eq. 2.25, and using the relations

$$\dot{\mathbf{X}}_\pm = \pm \mathbf{X}'_\pm. \tag{2.26}$$

The derivation gives us the only constraint on the general solution eq. 2.25,

$$\mathbf{X}'^2_\pm = 1. \tag{2.27}$$

For a cosmic string loop, the left- and right-moving components are periodic along the length of the loop

$$\mathbf{X}_\pm(\sigma + l) = \mathbf{X}_\pm(\sigma). \tag{2.28}$$

However, this means that oscillations of the fundamental mode are periodic with $\frac{l}{2}$, because from eqs. 2.25 and 2.28,

$$\mathbf{X}_{\pm}(t+\frac{l}{2},\sigma+\frac{l}{2})=\mathbf{X}_{\pm}(t,\sigma). \tag{2.29}$$

Thus, the frequency of the fundamental mode of oscillations on a cosmic string loop is

$$f=\frac{2}{l}. \tag{2.30}$$

The magnitude of the average velocity of segments along the loop can be estimated by averaging the squared velocity of segments along the loop over time,

$$\langle v^2\rangle=\frac{1}{Tl}\oint\int_0^T\dot{\mathbf{X}}^2dtd\sigma. \tag{2.31}$$

Using equations of motion eqs. 2.20 through 2.22, the average eq. 2.31 can be evaluated to have the value[2]

$$\langle v^2\rangle=0.5. \tag{2.32}$$

We see that oscillations along a cosmic string loop are relativistic.

The constraints eq. 2.27 on the general solution mean that $\pm\mathbf{X}'_{\pm}$ can be interpreted as curves on a unit sphere called the Kibble-Turok sphere[53]. Additionally, the periodicity of the left- and right-moving components along the loop eq. 2.28 imposes the condition on the tangent vectors

$$\oint d\sigma\mathbf{X}'_{\pm}=0. \tag{2.33}$$

These conditions imply that with the geometric interpretation outlined above, each curve on the Kibble-Turok sphere, $\pm\mathbf{X}'_{\pm}$, is not permitted to be contained within one hemisphere in order to have the cancellation that satisfies eq. 2.33. The magnitude of velocity of loop

segments can be obtained by differentiating the general solution eq. 2.25 and using eq. 2.26,

$$\dot{\mathbf{X}}^2(t,\sigma) = \frac{1}{4}\left(\mathbf{X}'_+(t+\sigma) - \mathbf{X}'_-(t-\sigma)\right)^2. \tag{2.34}$$

We see that loop segments can move at the speed of light $\dot{\mathbf{X}}^2 = 1$ when the two curves on the Kibble-Turok sphere intersect

$$\mathbf{X}'_+ = -\mathbf{X}'_-. \tag{2.35}$$

Recall that each of the two curves must occupy both hemispheres of the Kibble-Turok sphere, it is therefore rather difficult to avoid satisfying the condition eq. 2.35 for curves $\pm\mathbf{X}'_\pm$ that are continuous functions on the Kibble-Turok sphere.

Cusps arise along the cosmic string loop where the motion of a loop segment locally becomes luminal[2]. As the two curves on the Kibble-Turok sphere in general intersect at points, adjacent loop segments on both sides of a cusp do not have luminal motion. Then from the last equation of motion of the loop eq. 2.22, we see that indeed the loop must acquire a cuspy shape when a loop segment moves at the speed of light. Another interesting feature that can develop along the loop consists of kinks. These are basically bends along the loop, i.e. discontinuities along the curves $\pm\mathbf{X}'_\pm$ on the Kibble-Turok sphere which are really tangent vectors on the loop. The condition derived above eq. 2.35 coupled with the fact that $\pm\mathbf{X}'_\pm$ must occupy both hemispheres of the Kibble-Turok sphere, means that cusps are generally present along cosmic string loops. Another interesting implication is that when the curves $\pm\mathbf{X}'_\pm$ have discontinuities, i.e. when there are kinks on the loop, it becomes easier to avoid intersections of these curves, and therefore cusps along the loop should be reduced. It therefore appears that the presence of kinks along the loop, especially a large number of them, will tend to inhibit cusps. This has been confirmed theoretically[54, 33, 51] as well as through numerical simulations[55]. Though kinks along the loop are expected to be produced during string intercommutation which is usually not a smooth process[54, 2, 51], we should,

however, note that as kinks are small-scale features on the cosmic string loop, they should be smoothed out by gravitational backreaction on timescales far shorter than the loop decay timescale[2], meaning that they are expected to be reduced and eliminated relatively quickly. This has been observed to indeed take place through numerical simulations[56] at a timescale $t_{\text{kink}} \sim \frac{l}{n_{\text{k}}\Gamma G\mu}$, where $n_{\text{k}} = \frac{l}{l_{\text{kink}}}$. Thus the kink smoothing timescale can be much shorter than the loop decay timescale $t_{\text{decay}} \sim \frac{l}{\Gamma G\mu}$. The general expectation is therefore that cusps should be the dominant feature along cosmic string loops over kinks[35, 57]. However, some recent numerical simulations suggest that cusps may not dominate over kinks when the latter are present along the loop in large numbers[58, 59]. We therefore consider both cases in our simulation of harmonic gravitational waves from Galactic cosmic string loops.

2.2.2 Gravitational Wave Emission Spectrum

Both cusps and kinks are associated with highly relativistic motions of segments of cosmic string loops, and are therefore expected to produce bursts of powerful gravitational radiation at frequencies much higher than the fundamental mode[33, 35, 11] eq. 2.30. From the discussion in section 2.2.1, we noted that both cusps and kinks, and especially the former, are common features along cosmic string loops and are expected to be generally present. The constant presence of cusps and kinks on loops means that gravitational waves at high frequencies emitted by these features effectively modify the high frequency spectrum of gravitational waves emitted by cosmic string loops, from a typical quadrupole spectrum where the power of gravitational radiation in higher modes decreases exponentially, to one with more power distributed into high frequency modes[2].

Functional forms of the general solution for trajectories of cosmic string loops eq. 2.25 satisfying the constraint eq. 2.27 have to be found in order to study gravitational radiation from cosmic string loops, which is exactly generated by loop oscillations described by these solutions. However, finding such solutions analytically is very difficult[2]. The simplest

nontrivial loop trajectory involving the lowest two harmonic modes has been discovered by the works of ref. [53, 60], and is found to contain the 1st and 3rd harmonic modes,

$$\begin{aligned}\mathbf{X}(t,\sigma) = \frac{l}{4\pi}\Bigg[&\hat{e}_1\left((1-k)\sin\sigma_- + \frac{k}{3}\sin 3\sigma_- + \sin\sigma_+\right)\\ &-\hat{e}_2\left((1-k)\cos\sigma_- + \frac{k}{3}\cos 3\sigma_- + \cos\varphi\cos\sigma_+\right)\\ &-\hat{e}_3\left(2\sqrt{k(1-k)}\cos\sigma_- + \sin\varphi\cos\sigma_+\right)\Bigg],\end{aligned} \tag{2.36}$$

where $\sigma_\pm = \frac{2\pi}{l}(t \pm \sigma)$, $0 \leq k \leq 1$, $-\pi \leq \varphi \leq \pi$. Taking the time derivative of the trajectory eq. 2.36, we see that at $t = \left(m + \frac{1}{2}\right)\frac{l}{2}$, $m \in \mathbb{Z}$, motion of the loop at the points $\sigma = \frac{l}{4}$ and $\frac{3l}{4}$ is luminal[32], and therefore the solution has cusps along the loop. As we discussed in section 2.2.1, cusps are general features of solutions for loop trajectories. The 2nd harmonic mode is excluded from the solution eq. 2.36 because it has been shown that solutions involving the 1st and 2nd or the 2nd and 3rd harmonic modes are not permitted mathematically[61].

Having a functional form for the trajectory solution of a cosmic string loop, its gravitational radiation can now be derived. We start with the energy-momentum tensor of a cosmic string loop. In the transverse gauge, this has been shown to take on a simple form[32]

$$T^{\mu\nu}(t,\mathbf{X}) = \mu\int d\sigma\left(\dot{x}^\mu\dot{x}^\nu - x'^\mu x'^\nu\right)\delta^{(3)}(\mathbf{X} - \mathbf{X}(t,\sigma)). \tag{2.37}$$

Then the power of gravitational waves emitted by the loop in the frequency modes per solid angle can be calculated using the Fourier transform of the loop energy-momentum tensor $T^{\mu\nu}(f_n,\mathbf{k})$[62],

$$\frac{d\dot{E}_n}{d\Omega} = 4\pi G f_n^2\left(T^*_{\mu\nu}(f_n,\mathbf{k})T^{\mu\nu}(f_n,\mathbf{k}) - \frac{1}{2}\left|T^\nu_\nu(f_n,\mathbf{k})\right|^2\right). \tag{2.38}$$

Then the total power of gravitational wave emission from a cosmic string loop can be obtained

by integrating over the solid angle and summing over all frequency modes[2, 35],

$$P = \sum_{n=1}^{\infty} \int d\Omega \frac{d\dot{E}_n}{d\Omega} \equiv \Gamma G\mu^2 \equiv \sum_{n=1}^{\infty} P_n G\mu^2, \tag{2.39}$$

where the dimensionless parameters Γ and P_n parametrize the total power and power in each frequency mode of gravitational wave emission from the loop, respectively, with

$$\Gamma = \sum_{n=1}^{\infty} P_n. \tag{2.40}$$

As we will see later in this section, loops with cusps and kinks have power-law gravitational wave emission spectra, $P_n \propto n^{-s}$. Then the power of emission in each frequency mode in terms of the total power is

$$P_n = \frac{\Gamma}{\zeta(s)} n^{-s}, \tag{2.41}$$

where $\zeta(s)$ is the Riemann zeta function. From eq. 2.47, we see that cosmic string loops decay slowly compared to the periods of their gravitational wave emission. This means that such emission should have very well defined frequency modes. We can see this from the power of emission eq. 2.39[31],

$$Q_n = 2\pi f_n \frac{E}{\dot{E}_n} = \frac{4\pi n}{l} \frac{\mu l}{P_n G\mu^2} = \frac{4\pi n}{P_n G\mu}. \tag{2.42}$$

We see that indeed gravitational wave emission from the loops is highly monochromatic in each frequency mode.

The parameter Γ is independent of the size of the loop, but does depend on loop trajectories[2]. Early derivations and numerical simulations have produced a range of values $44 \lesssim \Gamma \lesssim 100$[2, 63, 3]. More recent studies tend to converge at around $\Gamma \sim 50$[33, 35, 31, 36, 64, 11, 29], and that the values for cusps- and kinks-dominated spectra do not differ very significantly. The range of possible values of Γ is at most a factor of ~ 2, and therefore a

detailed estimate of this parameter is not important for our purpose. Thus, we use the value predominantly adopted by recent studies of gravitational waves from cosmic string loops, $\Gamma = 50$ for this study.

Using the solution for loop trajectories eq. 2.36, the work of ref. [32] first derived the gravitational wave emission spectrum of a cosmic string loop with cusps. Instead of an exponentially decreasing spectrum for the power of gravitational radiation in frequency modes expected from the quadrupole formula, contribution of power by cusps to high frequency modes has turned the spectrum into a power-law, with

$$P_n \propto n^{-\frac{4}{3}}. \tag{2.43}$$

These gravitational waves are emitted over an angular scale

$$\theta_n \sim n^{-\frac{1}{3}}. \tag{2.44}$$

Even though this spectrum is derived using the particular solution for loop trajectories eq. 2.36, the spectrum has been shown to be generic for all cuspy loop trajectories where cusps dominate small-scale features along the loop[2, 33]. In fact, the general solution[65] to the loop trajectory eq. 2.25 with constraint eq. 2.27 involving the first two harmonics has been discovered, and has been shown not to make qualitative changes to results derived using the simple solution[65, 61]. The spectrum eq. 2.43 has been confirmed by later theoretical works[2, 66, 64, 51] as well as numerical simulations[67, 57] of trajectories of cosmic string loops. Mathematical pursuits of more general solutions to loop trajectories continue[68]. However, higher harmonic terms in loop trajectories are likely unimportant physically, since they are expected to be damped by cosmic expansion soon after loop formation[2]. As we discussed in section 2.2.1, cusps are generic features of loop trajectories and usually dominate over kinks as the latter are smoothed by gravitational backreaction. Thus, the

cusps-dominated spectrum eq. 2.43 is frequently adopted by studies of gravitational wave emission by cosmic string loops[35, 31, 36, 4, 69, 70, 3, 11].

We discussed in section 2.2.1 that kinks are produced during string intercommutation, and that their presence tends to inhibit cusps. Recent numerical simulations[58, 59] suggest that kinks domination over cusps along the loop may not be an impossibility when kinks are sufficiently numerous. We therefore also consider the kinks-dominated spectrum of gravitational waves emitted by cosmic string loops in our study. Early calculations of kinks-dominated loop trajectories suggest a steeper power-law gravitational wave spectrum $P_n \propto n^{-2}$[54, 2, 66]. However, more recent calculations conclude that the kinks-dominated gravitational wave spectrum is described by the power-law[33, 64]

$$P_n \propto n^{-\frac{5}{3}}. \tag{2.45}$$

The angular scale of gravitational wave emission is the same as that of the cusps-dominated spectrum eq. 2.44, with the exception that the angular scale of emission for the kinks-dominated spectrum only applies to one angular direction, while the power of emission is distributed isotropically in the orthogonal angular direction. Thus, gravitational wave emission from kinks-dominated loops covers a much larger solid-angle in a "fan-like" pattern than does that from cusps-dominated loops. This kinks-dominated gravitational wave spectrum eq. 2.45 has since been adopted by studies in the literature[57, 11]. Comparing this spectrum with the cusps-dominated one eq. 2.43, we see that when cusps are present, their shallower emission spectrum tends to dominate over the steeper kinks-dominated emission spectrum[51].

We see from the angular scale of gravitational wave emission eq. 2.44 and the discussion above that though not exactly isotropic, gravitational waves emitted by both cusps- and kinks-dominated loop trajectories are beamed only for high frequency burst modes. Our study focuses on low frequency harmonic modes of gravitational waves emitted by cosmic

string loops where the power of emission is distributed over a large solid angle, and considering high frequency burst signals is not congruent with our main objective. We should note that from the spectra eqs. 2.43 and 2.45, it is clear that gravitational wave bursts from cosmic string loops account for a very small fraction of the total power of gravitational radiation from these loops. Using eq. 2.40, we can easily estimate that in fact close to half of the total power of gravitational waves emitted by loops goes into the fundamental mode alone. Also, from eqs. 2.43 and 2.44, we see that the enhancement to the gravitational wave burst signal from beaming is actually not high at all compared to the reduction due to the power-law emission spectrum. Moreover, for a given detector frequency range, burst signals are emitted by loops with very low fundamental frequencies, i.e. very large loops. These loops are created later in time and therefore have low number densities compared to those of loops emitting harmonic signals in the frequency range, as can be seen from eq. 2.18. Lastly, there exists the possibility that the orientation of a loop can change over time, turning detecting burst signals into transient detections. We refer the interested reader to the work of ref. [33] for detection of gravitational wave bursts from cosmic string loops in the universe, and to the work of ref. [11] for theoretically estimating detection of burst signals from loops in the Galaxy.

2.2.3 The Stochastic Background

Having an understanding of the power of gravitational waves emitted by cosmic string loops eq. 2.39 as well as the number density of these loops in the universe eq. 2.18, we can compute the stochastic background of gravitational radiation from cosmic string loops in the LISA frequency range. This is the total background gravitational radiation from unresolved loops in the universe that either exist presently or have existed throughout the history of the universe. In this sense, the stochastic background is best characterized as a constant energy density in the universe in the form of gravitational radiation. For our objective of

directly detecting harmonic gravitational waves from individual nearby loops, the stochastic background serves as a source of background noise.

Recall from eq. 2.39 the total power of gravitational wave emission by a loop, and assuming that gravitational radiation is the only loop decay mechanism, then loops decay at the timescale[2]

$$t_{\rm d} \sim \frac{E}{P} = \frac{l\mu}{\Gamma G\mu^2} = \frac{l}{\Gamma G\mu}. \tag{2.46}$$

We immediately identify $\Gamma G\mu$ as the loop decay rate. This means that at time t, the size of a cosmic string loop created at time $t_{\rm c}$ with size $l_{\rm c} = \alpha t_{\rm c}$ is[35]

$$l(t_{\rm c}, t) = \alpha t_{\rm c} - \Gamma G\mu(t - t_{\rm c}). \tag{2.47}$$

Loops with other decay mechanisms have higher decay rates and so are less abundant, emitting weaker gravitational wave signals for detection. They are therefore not considered in our study. Using eqs. 2.30 and 2.47, we can rewrite the loop number density eq. 2.18 in terms of the frequency of gravitational wave emission by the loops, observed at time t, $n(f, t)$. To obtain the energy density of gravitational waves emitted by cosmic string loops in the universe today t_0, we need to redshift and integrate the power of gravitational waves emitted by all loops over all times in the history of the universe, from the formation time of the earliest loops whose gravitational waves become relevant to the LISA frequency range, t_i. Using eq. 2.39, the stochastic background energy density from cosmic string loops is[35]

$$\rho(f) = \Gamma G\mu^2 \int_{t_i}^{t_0} dt \left(\frac{a(t)}{a(t_0)}\right)^4 n\left(f\frac{a(t_0)}{a(t)}, t\right), \tag{2.48}$$

where f is the frequency observed by the detector today. Being a constant energy density in the universe, the stochastic background is usually expressed[35, 71] as a energy density

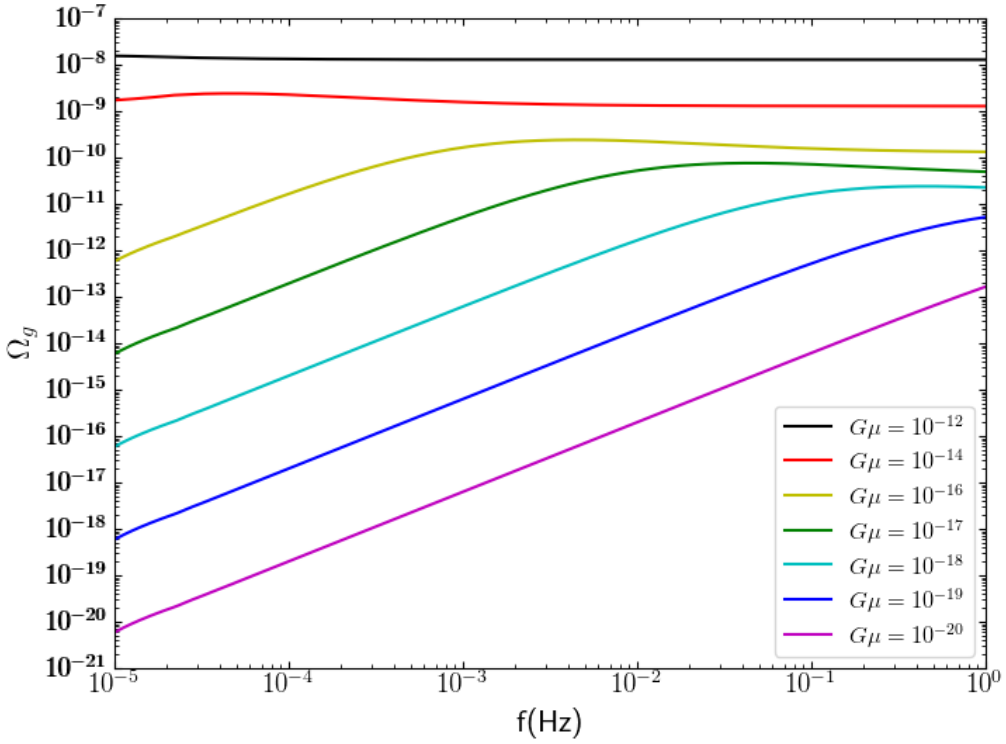

Figure 2.3: The energy density spectrum of the stochastic background from cosmic string loops with initial loop size $\alpha = 0.1$ for $G\mu$ from 10^{-12} to 10^{-20}, in the LISA frequency range.

spectrum in terms of the critical density of the universe $\rho_c = \frac{3H_0^2}{8\pi G}$,

$$\Omega_g(f) = \frac{8\pi G}{3H_0^2} \frac{d\rho(f)}{d\ln f}. \tag{2.49}$$

The expression for the energy density of the stochastic background eq. 2.48 does not distribute power of gravitational wave emission into higher frequency modes, and instead, concentrates the total power of emission in the fundamental mode. As we discussed in section 2.2.2, this should nevertheless serve as a good approximation. It has been confirmed by the comparison in ref. [35] that the stochastic background is not significantly changed by distributing power of gravitational radiation into higher frequency modes.

We present in fig. 2.3 the stochastic background from cosmic string loops computed

from eqs. 2.48 and 2.49 using our one-scale model of loop number density eq. 2.18 with initial loop size $\alpha = 0.1$ for $G\mu$ from 10^{-12} to 10^{-20}, in the LISA frequency range. First, we note that our results are in good agreement with those from ref. [35]. We have verified that the difference in the overall normalization is attributed to the cosmology of massive neutrinos, as we will discuss in sections 3.1.1 and 4.2. The curves in fig. 2.3 also exhibit clearly characteristics expected from the stochastic background from cosmic string loops.

For loops with a given string tension, there are two regions in the stochastic background. First, there is a low-frequency region where the energy density spectrum increases as a power-law. This region is dominated by gravitational waves emitted in the matter era from loops created in the radiation era[3]. That is to say, the dominant contribution to this low-frequency region with a rising power-law comes from larger loops created later in time that are mostly still around in the universe today. As we go to higher frequency, this power-law region gradually transitions into the high-frequency flat region. The stochastic background in this region is dominated by gravitational waves emitted in the radiation era[3]. This means that the dominant contribution to this region is made by smaller loops with very early formation times. These loops have experienced significant loop decay today and in fact many have already completely evaporated. Thus, the low-frequency power-law region consists primarily of contribution from loops outside of the decay regime, whereas contribution to the high-frequency flat region mostly comes from loops that are already in the decay regime. For all values of string tension considered with $\alpha = 0.1$, loops created in the matter era are very large and emit gravitational waves at frequencies far below the LISA frequency range, as we will see in section 3.1.4.

We see from eq. 2.39 that the power of gravitational wave emission by cosmic string loops is higher for loops with higher string tension. This contributes to a stronger stochastic background in general for loops with higher string tension. However the stronger power of gravitational wave emission also enhances loop decay as can be seen from eq. 2.47. In fact,

we can see that loops with $G\mu = 10^{-12}$ and 10^{-14} emitting gravitational waves in the LISA frequency range are essentially all in the decay regime. The beginning of the decay regime characterized by the transition in the curves in fig. 2.3 shifts towards higher frequency for loops with lower string tension, because of the weaker gravitational wave emission and hence slower decay. With low string tension, even small loops emitting gravitational waves at high frequencies with very early creation times have not decayed significantly.

The fact that the high-frequency region of the stochastic background is flat is a feature of the decay regime. These significantly decayed loops with very different sizes and therefore frequencies of gravitational wave emission are in fact created at approximately the same time, with initial loop sizes that are very close fractionally. However, from eq. 2.46 we see that the process of loop decay amplifies fractional differences in loop sizes over time. The fact that their creation times are very close means that these loops have similar number densities, and hence the flat high-frequency region of the stochastic background. Comparing the shapes of our results in fig. 2.3 to those[3, 57, 29] computed using a distribution of initial loop sizes obtained from the most state-of-the-art loop formation simulation[52, 3], we see that additional contribution is made to this region by loops created with smaller initial sizes in the distribution. The drop off as frequency increases past the transition of the two regions is therefore more gradual than that with the one-scale model. Still, the high-frequency region eventually flattens when production of loops with small initial sizes is cut off at the gravitational backreaction length-scale. This additional contribution to the high-frequency region is not important for our purpose, because the possibility of detection in our simulation comes from loops that are outside of the decay regime, as we will see in section 3.3.6. We also note that excluding the difference due to the cosmology of massive neutrinos, our estimates of the stochastic background in the low-frequency region are greater than those in refs. [3, 29] by about two orders of magnitude. This should be expected from the discussion at the end of section 2.1.2, where we noted that at $\alpha = 0.1$, our normalization

factor of the loop number density eq. 2.18 is greater than the effective one estimated from the distribution of initial loop sizes produced by that loop formation simulation by about that factor. This overestimation becomes smaller in the high-frequency region because the distribution of loops with small initial loop sizes from the loop formation simulation makes additional contribution in that region. As we discussed in section 2.1.2, we are making predictions for the best-case scenario by using the one-scale model.

As we will discuss in section 3.3.2, contributions from higher harmonic modes for both cusps- and kinks-dominated gravitational wave emission spectra eqs. 2.43 and 2.45 are eventually incorporated into our simulation through postprocessing. This is nevertheless unimportant for the stochastic background because first all, we discussed above that distributing power of gravitational wave emission into higher frequency modes does not significantly change the stochastic background, and more importantly, the stochastic background is not a dominant source of noise in our simulation for the region of the parameter space where detection of harmonic gravitational waves emitted by nearby individual cosmic string loops can potentially be made, as we will see in sections 3.3.1 and 4.1.2.

2.3 Cosmic String Loops in the Galaxy

2.3.1 Loop Clumping

As we mentioned in chapter 1, the original motivation for the existence of cosmic strings in the universe comes from the expectation that such 1D topological defects are created from SSB at the end of inflation with high string tension $G\mu \sim 10^{-6}$ corresponding to the GUT scale. Cosmic string loops with such high string tension lose energy rapidly through gravitational radiation and therefore decay away quickly as shown by eq. 2.47. Thus, the primary effect such cosmic strings may have on the galactic length-scale is to possibly seed structure formation through the density perturbation they cause[2, 4].

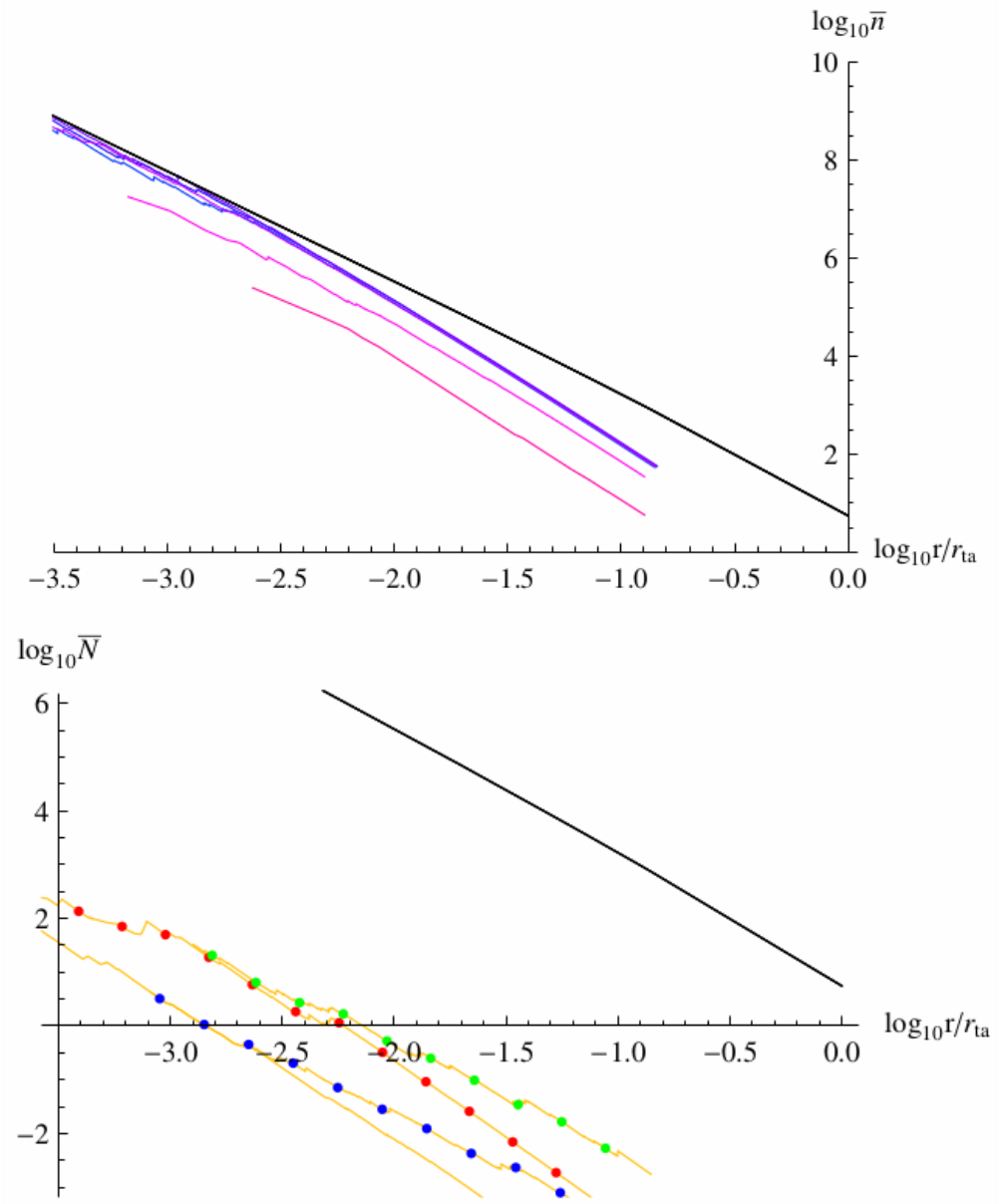

Figure 2.4: Overdensity of cosmic string loops in the Galaxy as a result of loop clumping in the dark matter halo, for loops created from loop formation models in the large- (upper panel) and small-loop paradigm (lower panel). The black line represents cold dark matter overdensity. Purple curves in the upper panel represent overdensity of loops created with $\alpha = 0.1$, with $G\mu = 10^{-10}$ to 10^{-15} from bottom to top. Yellow curves in the lower panel represent overdensity of loops created with $\alpha = 20(G\mu)^{1+2\chi}$ for various common values of χ, and $G\mu = 10^{-15}$. Figure from ref. [4].

In the modern picture of cosmic strings with very low values of string tension, loops decay slowly and can survive for many Hubble times. Even though motion of cosmic string loops has relativistic velocities as we discussed in section 2.2.1, the center-of-mass (COM) velocity of the loops is damped over time by cosmic expansion as[2]

$$p \propto a^{-1}, \tag{2.50}$$

where p is the momentum of the loop. This means that the COM velocities of these long-lived loops with low string tension created in the very early universe during the radiation era will have been completely non-relativistic for a long time by now. Such cosmic string loops with low string tension should therefore behave similarly to cold dark matter on the galactic scale, and clump in the dark matter halo of the Galaxy following the halo density profile, resulting in a great overdensity of cosmic string loops in the Galaxy. The idea that loops with low string tension clump in the dark matter halo of the Galaxy is first proposed by the works of refs. [14, 31], and the corresponding overdensity of loops in the Galaxy is estimated to be at least a factor of 10^5.

A detailed analysis of the physical process of clumping of cosmic string loops in the Galaxy is carried out in the work of ref. [4], and key findings are presented in fig. 2.4. Loop overdensities in the Galaxy expected for loops created with loop formation models from the large- and small-loop paradigms are presented in the upper and lower panels, respectively, for string tension down to $G\mu = 10^{-15}$, with the dark matter halo density profile also plotted as a reference.

We see from eqs. 2.32 and 2.50 that it takes many Hubble times to sufficiently damp the peculiar velocity of a loop so that it becomes non-relativistic. Thus, the process of loop clumping in the Galaxy prefers loops with earlier creation times, meaning that the process favors loops with larger α and lower $G\mu$. This fact is clearly reflected by fig. 2.4, where loops in the upper panel created with $\alpha = 0.1$ all clump very well following the dark matter

density profile of the Galactic halo, with clumping becoming increasingly complete as string tension decreases. Loops created with $\alpha = 20(G\mu)^{1+2\chi}$ in the lower panel on the other hand, do not clump well at all. Thus, loops created with small initial sizes are not relevant for this study, as they do not clump well in the Galaxy, and therefore cannot contribute to potential detection of harmonic gravitational wave signal from nearby cosmic string loops. Detection of loops in the Galaxy requires loops created with large initial sizes from loop formation models in the large-loop paradigm.

One more feature to note from the upper panel of fig. 2.4 is the fact that the curves representing loops with $G\mu \lesssim 10^{-13}$ are basically identical. This indicates that loops with such low string tension are created early enough to have experienced sufficient damping of their peculiar velocity by cosmic expansion that allows them to fully complete the clumping process[4]. This is to say that these loops simply clump like dark matter on the scale of the Galactic halo. We therefore assume complete clumping of cosmic string loops in the Galaxy in our study. This is somewhat of an overestimation of loop abundance in the Galaxy for loops created with $\alpha = 10^{-5}$, and may overestimate detection statistics for these loops, if there are any detections at all that is. We can see from the upper panel of fig. 2.4 that the assumption of complete clumping also slightly overestimates loop number density for loops with $\alpha = 0.1$ in the Galaxy at very large radii. The effect should be insignificant as the contribution from gravitational waves emitted by loops in such far away regions is very small, especially given that the loop number density itself is very low in these regions. The reason that even with complete clumping, overdensity of loops at large radii does not fully follow that of the dark matter is because of the rocket effect. This is in fact another reason that this region is unimportant in this study. In many cases there simply are no loops at all at these large radii due to the rocket effect. We will discuss the rocket effect in the context of this study in section 2.3.2.

Enhancement of loop number density in the Galaxy as a result of clumping is indeed

very significant in our simulation. For loops created with $G\mu = 10^{-20}$ and $\alpha = 0.1$, when complete loop clumping is considered alone, the number density in the Galaxy can be so high that just for loops emitting gravitational waves in the single very narrow LISA frequency bin $\Delta f = \frac{1}{T_{\rm obs}} \sim 3 \times 10^{-8}$ Hz for a 1-year mission duration, their distance to the solar system can be only ~ 0.1 kpc on average. Knowing that this is just for one frequency bin, this fact really raises the hope that the harmonic gravitational wave signal emitted over a wide angular scale and which dominates the total power of emission can be resolved individually from a nearby small loop, instead of relying on the highly beamed burst signal carrying only a small fraction of the total power of emission from distant large loops which are created with lower number density.

From the power of gravitational wave emission by a cosmic string loop in eq. 2.39, the flux of the gravitational wave received by the detector is

$$F(r') = \frac{\Gamma G\mu^2}{4\pi r'^2}, \tag{2.51}$$

where r' is the distance from the loop to the solar system, and we always treat gravitational wave emission from loops as isotropic in our simulation. As we will discuss in section 3.1.4, for our purpose, this treatment is reasonable for low frequency harmonic modes where the angular scale of gravitational wave emission is wide. We can integrate over the Galaxy to obtain the total flux of gravitational waves in each frequency bin emitted by all loops in the Galaxy,

$$F_{\rm g}(f) = \int F(r') n_{\rm g}(r, f) dV, \tag{2.52}$$

where $n_{\rm g}(r, f)$ is the loop number density in the Galaxy for the frequency bin f, r is the distance from the loop to the center of the Galactic halo. Low frequency harmonic modes of gravitational waves emitted by cosmic string loops are weak perturbations of spacetime, and are well represented by plane-wave solutions of linearized gravity[33, 31]. The maximum

wavelength of gravitational waves in the LISA frequency range is less than the size of the solar system, and therefore it is appropriate to take the short wavelength approximation where the curvature of background spacetime is essentially flat on the scale of these gravitational waves, $\frac{\lambda}{\mathcal{R}} \sim 0$, where $\mathcal{R}$ is the scale of curvature of background spacetime. Then in the transverse traceless gauge with harmonic gauge condition, the Isaacson stress-energy tensor simplifies to[72, 73]

$$T_{\mu\nu} = \frac{1}{32\pi G} \left\langle \frac{\partial h_{ij}}{\partial x^\mu} \frac{\partial h^{ij}}{\partial x^\nu} \right\rangle . \tag{2.53}$$

We immediately identify the time component of the Isaacson stress-energy tensor in the direction of propagation of the wave as corresponding to the flux of the gravitational wave. Substituting the plane-wave solution into eq. 2.53, the flux is[73]

$$F = T^{03} = \frac{\pi f^2}{8G} \langle h_{ij} h^{ij} \rangle = \frac{\pi f^2 h^2}{8G}, \tag{2.54}$$

where h is the strain amplitude of the gravitational wave. The total strain amplitude of gravitational waves in each frequency bin from all loops in the Galaxy can then be obtained by calculating eq. 2.52 and inverting eq. 2.54. Also, from eqs. 2.39, 2.51 and inverting eq. 2.54, the strain amplitude of a harmonic mode of gravitational wave emitted by a cosmic string loop can be calculated,

$$h_n = \frac{1}{f_n} \sqrt{\frac{8GF_n}{\pi}} = \frac{\sqrt{2P_n} G\mu}{\pi r f_n}. \tag{2.55}$$

We present in fig. 2.5 the total background strain amplitude of gravitational waves emitted by all loops created with $\alpha = 0.1$ and $G\mu = 10^{-12}$ to 10^{-20} that have clumped in the Galaxy subject to the rocket effect. Similar to plots of the stochastic background in fig. 2.3, there are two regions in the Galactic background. Loops emitting gravitational waves in the lower frequency region have not decayed significantly, while loops in the steeper higher frequency region have decayed substantially. We call the latter the decay regime. The

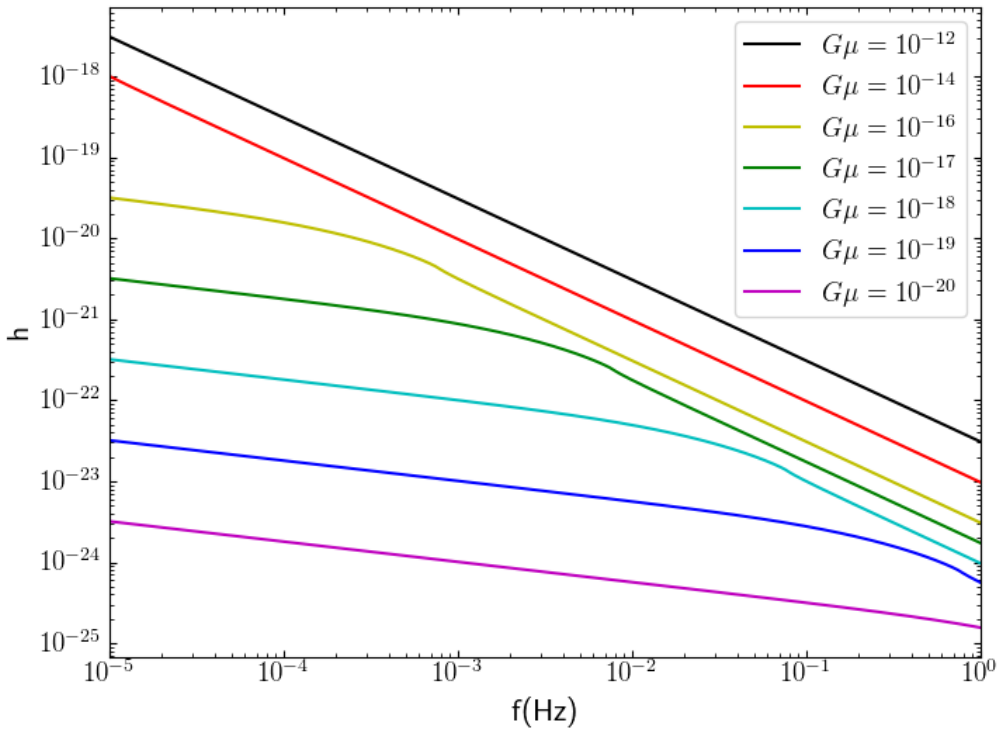

Figure 2.5: The total strain amplitude from all cosmic string loops in the Galaxy in the toy models described in chapter 3. The loops are created with $\alpha = 0.1$, and have string tension from $G\mu = 10^{-12}$ to 10^{-20}. They clump in the Galaxy subject to the rocket effect.

steepness of the decay regime is actually partially due to the rocket effect which becomes significant at about the same frequency, as we will discuss in section 2.3.2. There is a break in the transition which indicates that the rocket effect has become significant for loops orbiting at around the solar system orbit in the Galaxy. The Galactic background is the major confusion noise in our study which acts to prevent harmonic gravitational waves emitted by nearby individual loops from being resolved.

Clearly, the Galactic background strain amplitudes presented in fig. 2.5 are consistent with those in ref. [31] up to cosmology as we discussed in section 2.2.3. However, we should stress that these plots of the Galactic background model the physical Galaxy only when binned according to the log bins of eq. 2.18, and therefore should not be compared directly

with the LISA sensitivity curve. They do, however, represent the Galactic background in the toy models described in chapter 3. The physical Galactic background strain amplitudes are presented in fig. 4.3.

2.3.2 The Rocket Effect

In the context of clumping of cosmic string loops in the Galaxy, there is a competing physical process to the damping of loop peculiar velocity by cosmic expansion. We discussed in section 2.2.2 that gravitational wave emission by the loops, especially for high frequency modes, is associated with a high degree of anisotropy, as shown by eq. 2.44. As gravitational waves also carry momentum, the loops therefore experience a recoil from gravitational wave emission, as if being constantly propelled by a rocket. This physical process is hence named the rocket effect. The rocket effect experienced by cosmic string loops in the Galaxy with the cusps-dominated gravitational wave emission spectrum eq. 2.43 is analyzed in detail in the work of ref. [4].

It is reasonable to make the simplifying assumption that the direction of the gravitational wave recoil on a loop remains constant[4, 11]. Recall from section 2.2.2 that the power of gravitational wave emission from a loop remains constant throughout its life regardless of the decrease in loop size due to decay. This means that as a result of the rocket effect, a loop experiences a constant force per unit mass

$$a_{\rm r} = \frac{\Gamma_P G\mu}{l}, \tag{2.56}$$

where Γ_P parametrizes the total momentum carried by the gravitational wave. With $\Gamma \sim 50$, the value of this parameter has been estimated to be $\Gamma_P \sim 10$[4]. Since gravitational wave emission from loops spans a wide angular scale for low frequency harmonic modes which dominate the total power of emission, the resultant cancellation means that $\Gamma_P < \Gamma$. In the

absence of other forces on the loop, the quantity in eq. 2.56 is the acceleration of the loop caused by the rocket effect.

As an external force on the loop, the rocket effect certainly works against damping of loop peculiar velocity by cosmic expansion, and hence reduces loop clumping in the Galaxy. This is the reason that even for loops that are completely clumped, their density profile in the Galaxy at large radii is still slightly below that of dark matter in the Galactic halo, as can be seen in the upper panel of fig. 2.4. In fact, it has been calculated that the increase in loop peculiar velocity due to the rocket effect makes loop capture by the gravitational potential of the Galactic dark matter halo impossible outside of the capture radius[4]

$$r_{\rm cap} = r_{\rm ta}\left(\frac{5H_0 r_{\rm ta}\alpha t_{\rm c}}{2\Gamma_P G\mu t_0}\right)^{\frac{4}{5}}. \tag{2.57}$$

We see that the longer the loop has experienced the constant recoil due to the rocket effect, the harder it becomes for it to be captured by the Galactic dark matter halo. Of course capture is also more difficult when string tension is high, causing stronger gravitational wave emission and therefore a larger recoil.

In addition to the reduction in the process of loop capture by the Galactic dark matter halo, the more important consequence of the rocket effect experienced by loops in the Galaxy is the ejection of already captured loops from the Galaxy as a result of the constant force on the loop due to the recoil of gravitational wave emission. The equivalent problem of analyzing the behavior of an object in an r^{-2} potential well subject to a constant external force is well known with electromagnetic interaction on the quantum scale, i.e. the Stark effect. The behavior of cosmic string loops in the Galaxy subject to the rocket effect is essentially the classical counterpart of the Stark effect, called the Stark problem in the field of celestial mechanics. Complete solutions[74, 75, 76] have been found for the Stark problem which indicate that unlike the behavior on the quantum scale where stable bound states can exist, classically, the orbit of the object always becomes parabolic in the limit of $t \to \infty$[74],

i.e. the object is always eventually ejected from the potential well.

We can motivate an intuitive understanding of the characteristics of the solution to the Stark problem described above by considering the simple case of an object in a circular initial orbit experiencing a constant force in the plane of the orbit. It is clear that during the first half of the orbit, the force accelerates the object and increases the aphelion (in this example we consider orbits around the Sun). During the other half of the orbit where the projection of the velocity of the object onto the direction of the force is in the opposite direction, the force decelerates the object and actually reduces the perihelion. Thus, the overall effect of the constant force on the orbit of the object is to gradually increase its orbital eccentricity over many orbits, which eventually turns the orbit parabolic, resulting in the ejection of the object.

The Stark problem in the context of captured cosmic string loops in the Galaxy has been studied in detail in the work of ref. [4]. Loops already captured by the gravitational potential of the dark matter halo will be ejected from the Galaxy before the present time outside the truncation radius

$$r_{\rm tr} = r_{\rm ta}\left(\frac{1.575 H_0 r_{\rm ta}\alpha t_{\rm c}}{\Gamma_P G\mu t_0}\right)^{\frac{4}{5}}. \tag{2.58}$$

We see that the truncation radius takes on a very similar form to that of the capture radius eq. 2.57, with the only difference being the more stringent numerical factor. Clearly, $\lim_{t_0\to\infty} r_{\rm tr} = 0$, which is consistent with the general solution of the Stark problem dictating that all string loops should be ejected from the Galaxy eventually. Even though α appears in the expression of the truncation radius eq. 2.58, the quantity itself does not actually depend on α for a given loop size, i.e. frequency of gravitational wave emission. When loop size is fixed, varying α has no effect on $r_{\rm tr}$ because $\alpha t_{\rm c}$ stays constant, and we are simply selecting loops created at different times.

The rocket effect acts over time and gradually ejects loops over many orbits. Thus, older

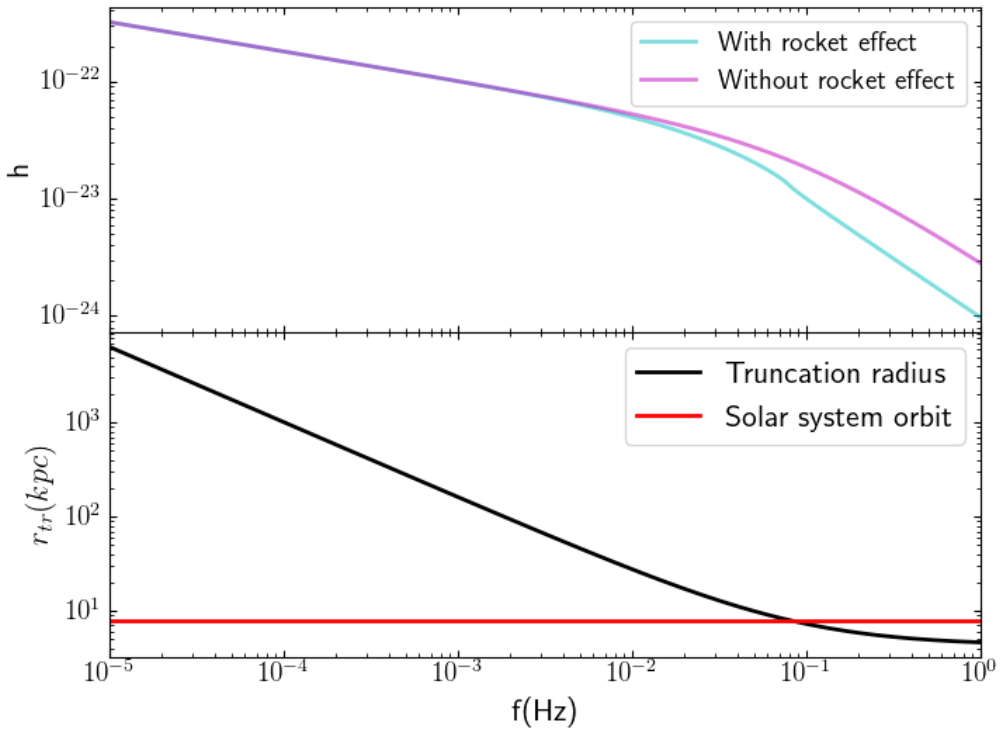

Figure 2.6: The background strain amplitude from cosmic string loops in the Galaxy in the toy models described in chapter 3, with $\alpha = 0.1$, $G\mu = 10^{-18}$, is plotted in the upper panel, for both with (cyan) and without (magenta) incorporating the rocket effect. The corresponding truncation radius as a function of frequency is plotted in the lower panel.

loops have smaller truncation radii. This means that for loops created with a given α, smaller loops have smaller truncation radii. In terms of the frequency of gravitational wave emission, truncation due to the rocket effect is more severe for loops emitting gravitational waves at higher frequencies. The truncation radius is therefore an implicit function of the frequency of gravitational wave emission. We can therefore define a truncation frequency $f_\odot$ such that

$$r_{\rm tr}(f_\odot) \equiv r_\odot, \tag{2.59}$$

where $r_\odot \sim 8$ kpc[31] is the solar system orbit. The truncation frequency is significant for our purpose because when $r_{\rm tr} < r_\odot$, there simply cannot exist nearby loops to the solar

system. This severely restricts the possibility of resolving harmonic gravitational wave signal from an individual loop for $f > f_\odot$. On the other hand, when $f \lesssim f_\odot$, detection of signal from individual nearby loops can be enhanced, because there the loop distribution in the Galaxy is such that the confusion background near the solar system is reduced while loops are still permitted to be located very nearby. Cosmic string loops with higher string tension emit gravitational waves more strongly and experience stronger recoils. They therefore have smaller truncation radius. This means that as $G\mu$ increases, $f_\odot$ decreases. As we will see in section 3.3.6, in the LISA frequency range, the rocket effect strongly favors loops created with low string tension. Comparing the truncation radius eq. 2.58 to loop decay eq. 2.47, we see that the relations between αt_c and $\Gamma G\mu t_0$ (or $\Gamma_P G\mu t_0$) mean that the rocket effect has a similar dependence on the age of the loop as that of loop decay. In fact, as the frequency of gravitational wave emission increases, it happens that at solar system orbit in the Galaxy, the rocket effect always becomes significant at about the frequency where such loops enter the decay regime.

We present an illustration of the truncation of cosmic string loops in the Galaxy due to loop ejection by the rocket effect in fig. 2.6. The cyan curve in the upper panel is the same Galactic background strain amplitude with $\alpha = 0.1$, $G\mu = 10^{-18}$ found in fig. 2.5. When compared to the truncation radius as a function of frequency plotted in the lower panel, we see that the Galactic background strain amplitude displays the characteristic break we mentioned in section 2.3.1 at exactly the truncation frequency, representing the qualitative change to loop distribution around the solar system. The more interesting feature shown by the upper panel of fig. 2.6 is the fact we discussed above, that as frequency increases, significant background reduction begins in advance of the truncation frequency, potentially enhancing detection of harmonic gravitational wave signal from nearby individual loops in this region.

2.4 LISA Orbital Modulations

The LISA spacecraft is composed of three orbiters forming an equilateral triangle in space tilted at 60° with respect to the ecliptic. Each orbiter is in a separate Earth-trailing heliocentric orbit, resulting in an overall full rotation of the spacecraft over the course of a complete one-year orbital period. Additionally, the unit vector perpendicular to the plane of the triangular spacecraft projected onto the ecliptic always points towards the Sun, meaning that the sweep of the unit vector itself forms a cone with a 60° opening angle over the course of a complete one-year orbit[30, 5]. Schematic diagrams[5] of the basic orbital configuration of the LISA spacecraft are shown in fig. 2.7.

Gravitational waves can be interpreted as ripples of spacetime itself, and therefore one of the most directly measurable effects caused by a gravitational wave passing through, consists of changes to the spatial distance between two reference points. An interferometer can be used for measuring tiny distance changes through shifts in the relative phases of the emitted and reflected light beams caused by variations in the lengths of its arms. It is therefore sensitive to distance variations on the order of the wavelength of the light beam used, giving rise to extremely high sensitivities when very long arm lengths are used, and hence the idea of detecting gravitational waves using interferometers going back to 1962[77].

As an interferometer measures relative phase shifts of light beams and therefore relative variations in the lengths of its arms, its response to an incoming gravitational wave depends on the direction of propagation as well as polarizations of the wave. The detector response can therefore be quantified by the detector pattern functions for the two polarization eigenstates of gravitational waves, $F_+(\theta, \phi)$ and $F_\times(\theta, \phi)$, where $\hat{n} = (\theta, \phi)$ is the direction of propagation of the wave. Then the strain measured by the detector is just

$$h(t) = h_+(t)F_+(\theta, \phi) + h_\times(t)F_\times(\theta, \phi). \tag{2.60}$$

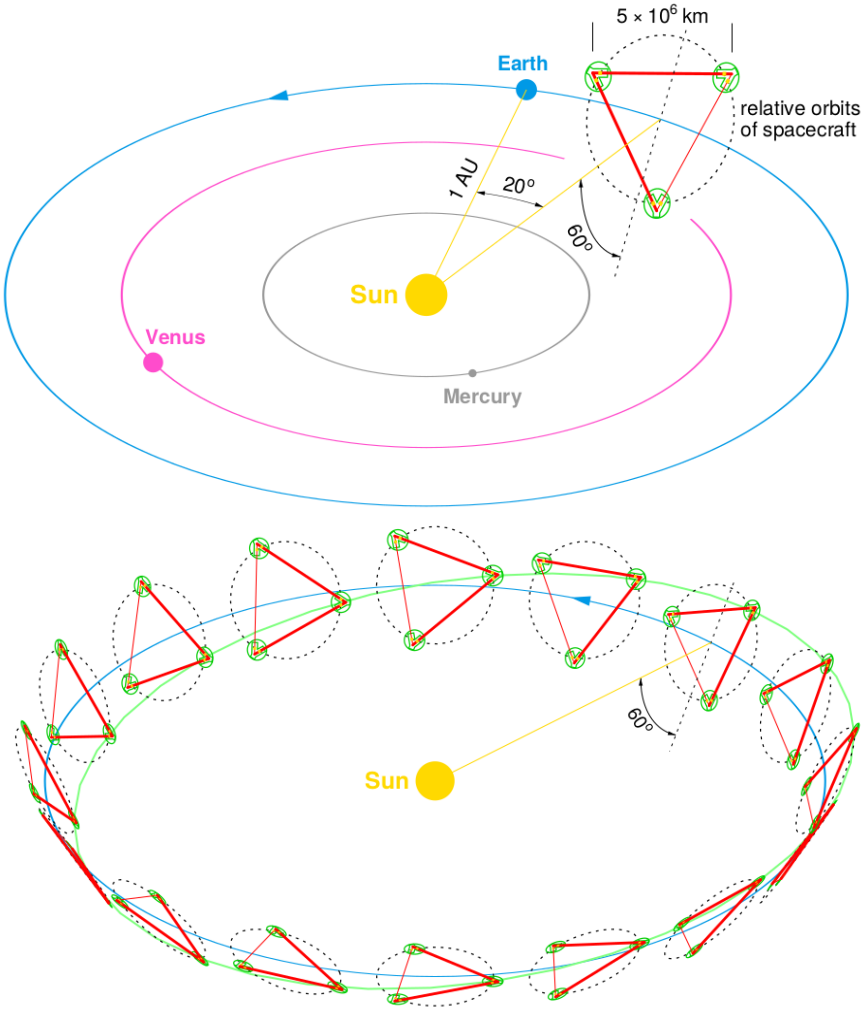

Figure 2.7: Schematic diagrams of the three orbiters of the LISA spacecraft in their Earth-trailing heliocentric orbits over the course of a complete one-year orbital period. Figure from ref. [5].

For a Michelson-type interferometer gravitational wave detector, the detector patterns functions have the simple form[77]

$$F_{+,\mathrm{M}}(\theta,\phi) = \frac{1}{2}\left(1+\cos^2\theta\right)\cos 2\phi; \tag{2.61}$$

$$F_{\times,\mathrm{M}}(\theta,\phi) = \cos\theta \sin 2\phi, \tag{2.62}$$

where without loss of generality, we used the alignment of the interferometer to define the polarization eigenstates. We see that

$$F_{+,\mathrm{M}}(0,0) = 1; \tag{2.63}$$

$$F_{\times,\mathrm{M}}(0,0) = 0. \tag{2.64}$$

This should be obvious given that when the incident gravitational wave is perpendicular to the plane of the interferometer with $\phi = 0$, a plus-polarized wave is exactly aligned with the arms of the interferometer and therefore produces maximal relative variations in the lengths of its arms, while a cross-polarized wave is exactly off by 45° and therefore produces the same variations in the lengths of both arms.

The three orbiters of the LISA spacecraft act simultaneously as emitters and reflectors of laser beams[30, 5], and in this way, the working principles of LISA are not very different from other interferometer gravitational wave detectors. In fact, even though the configuration of an equilateral triangle appears to be very different from that of Michelson-type interferometers, the detector patterns only differ from those in eqs. 2.61 and 2.62 by a very intuitive factor of $\frac{\sqrt{3}}{2}$[78, 79],

$$F_{+\times} = \frac{\sqrt{3}}{2} F_{+\times,\mathrm{M}}(\theta,\phi), \tag{2.65}$$

where again the detector is assumed to align with the polarization eigenstates.

Obtaining the detector patterns functions is mostly sufficient to characterize detector

response with respect to directions of propagation and polarizations of incident gravitational waves for ground-based detectors. However, LISA is a space-based gravitational wave detector, and its heliocentric orbital motion introduces major complications to its detector response characteristics. In particular, the orbital motion of LISA induces three types of modulations on the detected signal[80, 81]:

1. Amplitude modulations due to the sweeping of the antenna patterns of LISA, with the unit vector perpendicular to the plane of the spacecraft tracing out a cone shape as described previously;

2. Frequency modulations due to Doppler shifts in the gravitational wave signal caused by the relative motion between LISA and the source;

3. Phase modulations due to the fact that detector responses of LISA to the two polarizations of gravitational waves are different as can be seen from the detector patterns functions eq. 2.65.

All signal modulations due to LISA orbital motion described above are periodic over a complete one-year orbit.

Tracking LISA orbital motion and the associated signal modulations in real time in the simulation is far beyond current computational capabilities, nor is it necessary since the simulation makes predictions for a LISA mission duration of $T_{\rm obs} = 1$ year. Only the total effect of signal modulations averaged over the complete orbit is needed. This has been calculated by ref. [81] for monochromatic sources. The total correction factor of the detected gravitational wave strain amplitude of a monochromatic source due to signal modulations caused by LISA orbital motion averaged over a complete orbit is

$$\Upsilon = \sqrt{\frac{1}{2}\left(\left(1+\cos^2\iota\right)^2\langle F_+^2\rangle + 4\cos^2\iota\langle F_\times^2\rangle\right)}, \tag{2.66}$$

where $\iota \in [0,\pi]$ is the inclination of the source, and the detector patterns averaged over a

complete orbit are

$$\langle F_{+,\times}^2 \rangle = \frac{1}{4}\left(\cos^2 2\psi \langle D_{+,\times}^2 \rangle \mp \sin 4\psi \langle D_+ D_\times \rangle + \sin^2 2\psi \langle D_{\times,+}^2 \rangle\right); \quad (2.67)$$

$$\langle F_+ F_\times \rangle = \frac{1}{8}\left(\sin 4\psi \left(\langle D_+^2 \rangle - \langle D_\times^2 \rangle\right) + 2\cos 4\psi \langle D_+ D_\times \rangle\right), \quad (2.68)$$

where $\psi \in [0, \pi]$ is the polarization angle of the incident gravitational wave, and the Doppler modulations averaged over a complete orbit are

$$\langle D_+^2 \rangle = \frac{3}{2048}\left(487 + 158\cos^2\theta + 7\cos^4\theta - 162\sin^2 2\phi\left(1 + \cos^2\theta\right)^2\right); \quad (2.69)$$

$$\langle D_\times^2 \rangle = \frac{3}{512}\left(120\sin^2\theta + \cos^2\theta + 162\sin^2 2\phi\cos^2\theta\right); \quad (2.70)$$

$$\langle D_+ D_\times \rangle = \frac{243}{512}\cos\theta\sin 2\phi\left(2\cos^2\phi - 1\right)\left(1 + \cos^2\theta\right), \quad (2.71)$$

where ϕ is the longitude of the source in heliocentric ecliptic coordinates, and $\theta = \frac{\pi}{2} - b$, where b is the latitude of the source in heliocentric ecliptic coordinates.

CHAPTER 3

THE SIMULATION DEVELOPED WITH TOY MODELS

We develop the methodology necessary to successfully perform simulations of cosmic string loops in the Galaxy with the goal of making predictions on the possibility of LISA directly detecting harmonic gravitational wave emissions from nearby individual loops by considering toy models of the cosmic string loop number density. Computationally, the toy models come rather naturally by taking the original cosmic string loop number density eq. 2.18, and directly evaluating the expression at LISA frequency resolution $\Delta f = \frac{1}{T_{\text{obs}}}$. This direct rebinning is certainly not physical, and for the LISA frequency range $f \in \left[10^{-5}, 1\right]$ Hz, it results in a significantly inflated loop number density, by several orders of magnitude for higher frequencies. Such toy models correspond to a galaxy where there is a great overabundance of cosmic string loops compared to the one we find ourselves in.

One of the advantages of using toy models is that the loop number density is well behaved and easy to understand at all $G\mu$ for all frequencies. The real meaning of this statement will become clear in section 4.2.2 where we discuss loop abundance in the physical Galaxy. The great overabundance of cosmic string loops in the toy models seemingly presents a challenge for performing simulations. But this also means that the toy models serve as suitable training wheels for developing a robust set of simulation methods. It is also important to note that even though the toy models themselves are not physical, they are nevertheless based on a physical model. As will become apparent in section 3.3.9, the results from the toy models are far from meaningless, and they can, in fact, point us in the right direction which avoids the ill-behaved part of the parameter space, and therefore enable us to significantly reduce efforts and resources needed to obtain the physical results we ultimately seek.

3.1 Simulation Configuration

3.1.1 Cosmological and Astrophysical Parameters

For the cosmological model in this chapter, we adopt the standard ΛCDM cosmology with Planck 2015 cosmological parameters [82]:

$$H_0 = 67.74\text{km/s/Mpc}, \tag{3.1}$$

$$\Omega_{\text{m},0} = 0.3075, \tag{3.2}$$

$$\Omega_{\Lambda,0} = 0.6910, \tag{3.3}$$

$$\Omega_{\gamma,0} = 5.389 \times 10^{-5}, \tag{3.4}$$

$$\Omega_{\nu,0} = 1.436 \times 10^{-3}. \tag{3.5}$$

Neutrinos are regarded as massive, and their density value today eq. 3.5 is estimated by refs. [83, 84] using the method described in ref. [85]. Due to considerations of computational performance, they are treated as relativistic particles and therefore contribute to the radiation density of the universe. Compared to regarding neutrinos as massless throughout the history of the universe, this treatment enhances loop number density for loops included in our simulation which are mostly created in the very early universe during the radiation era. Again, results from our simulation represent optimistic estimates for the detection of harmonic gravitational wave signal from individual nearby loops.

Cosmic string loops clump in the Galaxy following the gravitational potential of its dark matter halo. N-body simulations of dark matter halos in the ΛCDM framework have produced a simple universal profile for the spatial distribution of cold dark matter, the Navarro-Frenk-White (NFW) profile [86]. The Milky Way dark matter halo is well modeled by the NFW profile [87, 88], and the distribution of number density of cosmic string loops

in the Galaxy is

$$n_{\rm g}(r,f) = \frac{n_{\rm g,0}(f)}{\frac{r}{R_s}\left(1+\frac{r}{R_s}\right)^2}. \tag{3.6}$$

The scale radius R_s is related to the virial radius $R_{\rm vir}$ by the concentration parameter C,

$$R_{\rm vir} = CR_s. \tag{3.7}$$

For the Milky Way, we follow the common definition of the virial radius [89, 90, 91], $R_{\rm vir} \sim R_{200}$, and

$$\bar{n}_{200}(f) = \frac{N\left(R_{200},f\right)}{V_{200}} = 200n(f), \tag{3.8}$$

where $n(f)$ is the cosmic string loop number density in the universe given by eq. 2.18. The normalization number density $n_{\rm g,0}(f)$ can therefore be obtained from

$$N\left(R_{200},f\right) = \int_0^{R_{200}} 4\pi r^2 n_{\rm g}(r,f)dr = 4\pi n_{\rm g,0}(f)R_s^3\left(\ln(1+C) - \frac{C}{1+C}\right) = 200n(f)V_{200}. \tag{3.9}$$

To be consistent with ref. [31], the following parameters for the NFW profile are adopted

$$R_s = 21.5 \text{ kpc} \tag{3.10}$$

$$C = 10 \tag{3.11}$$

For consistency with ref. [4], we set the turnaround radius for the Milky Way

$$R_{\rm ta} = 1.1 \text{ Mpc}. \tag{3.12}$$

3.1.2 Gravitational Wave Interference

As discussed in section 2.3.1, we always work with plane wave solutions of linearized gravity in the so-called short wavelength approximation where the curvature of background spacetime

is essentially flat on the scale of gravitational waves relevant to this study, i.e. $\frac{\lambda}{\mathcal{R}} \sim 0$, where $\mathcal{R}$ is the scale of curvature of background spacetime. Then for the purpose of accounting for superposition of gravitational waves emitted by cosmic string loops in the Galaxy at frequency f, we assume without loss of generality the gravitational wave emitted by the ith loop in the frequency bin

$$h_i(t) = h_i \sin\left(2\pi f t + \delta_i\right), \tag{3.13}$$

where h_i is given by eq. 2.55. The phases $\delta_i \in (-\pi, \pi]$ are completely uncorrelated. By the harmonic addition theorem[92], the total signal as a result of superposition of gravitational waves from all loops in the Galaxy emitting at frequency f is also a plane wave

$$h(t) = h \sin\left(2\pi f t + \delta\right). \tag{3.14}$$

The harmonic addition theorem enables us to perform the simulation efficiently by directly computing the total strain amplitude h and the overall phase δ from individual strain amplitudes h_i and phases δ_i of loops emitting gravitational waves in the frequency bin. The total strain amplitude of the frequency bin is

$$h = \sqrt{\left(\sum_{i=1}^{N} h_i \sin\delta_i\right)^2 + \left(\sum_{i=1}^{N} h_i \cos\delta_i\right)^2}, \tag{3.15}$$

where N is the total number loops emitting gravitational waves in this frequency bin. The overall phase of the frequency bin from the harmonic addition theorem is expressed as

$$\tan\delta = \frac{\sum_{i=1}^{N} h_i \sin\delta_i}{\sum_{i=1}^{N} h_i \cos\delta_i}. \tag{3.16}$$

The naive inversion of eq. 3.16

$$\delta_{1,2} = \tan^{-1} \frac{\sum_{i=1}^{N} h_i \sin \delta_i}{\sum_{i=1}^{N} h_i \cos \delta_i} \tag{3.17}$$

implies a range for the overall phase $\delta_{1,2} \in \left[-\frac{\pi}{2}, \frac{\pi}{2}\right]$, and is correct only for two quadrants of the complex plane when the phase is formulated using the complex notation. The real phase for the other two quadrants is shifted by π in either directions depending on conditions, i.e. $\delta_{3,4} = \delta_{1,2} \pm \pi$ depending on conditions. The overall phase of the frequency bin correct for all quadrants of the complex plane is

$$\delta = \tan^{-1} \frac{\sum_{i=1}^{N} h_i \sin \delta_i}{\sum_{i=1}^{N} h_i \cos \delta_i} + \begin{cases} 0, & \sum_{i=1}^{N} h_i \cos \delta_i \geq 0; \\ \pi, & \sum_{i=1}^{N} h_i \cos \delta_i < 0 \text{ and } \sum_{i=1}^{N} h_i \sin \delta_i > 0; \\ -\pi, & \sum_{i=1}^{N} h_i \cos \delta_i < 0 \text{ and } \sum_{i=1}^{N} h_i \sin \delta_i \leq 0. \end{cases} \tag{3.18}$$

We note that the frequency bins are independent of each other, and there is an entirely different distribution of cosmic string loops in the Galaxy for each bin. The simulation repeats the superposition computational process above for each frequency bin.

3.1.3 The Closest Loops Method

All cosmic string loops with $\alpha = 0.1$ in the Galaxy today emitting gravitational waves with frequencies in the LISA frequency range $f \in \left[10^{-5}, 1\right]$ Hz are created in the radiation era, with $G\mu = 10^{-12}$ having the youngest loops created at $z \sim 2.3 \times 10^5$. With $\alpha = 10^{-5}$, loops created in the matter era at $z \sim 2.3 \times 10^3$ are included only when $G\mu = 10^{-12}$, in which case the loop number density eq. 2.18 is overestimated[45]. However, we will see in section 3.3.8 that this has no significance for our purpose. During radiation era, the scale factor

$$a \propto t_c^{\frac{1}{2}}. \tag{3.19}$$

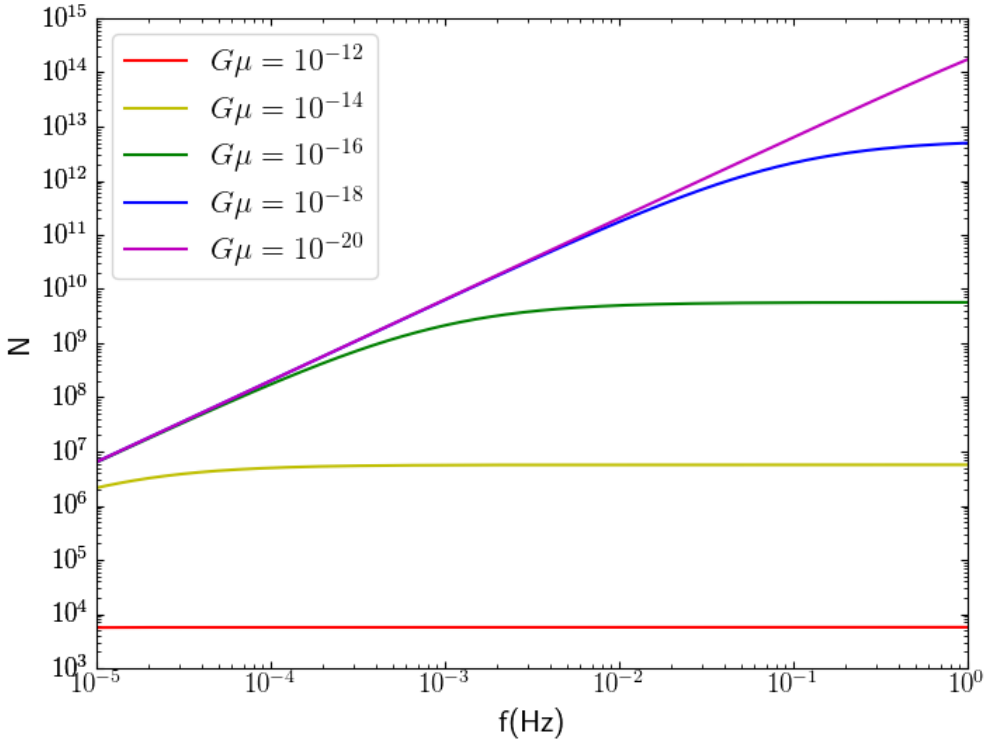

Figure 3.1: The number of cosmic string loops in the Galaxy at each frequency for $G\mu \in \left[10^{-12}, 10^{-14}, 10^{-16}, 10^{-18}, 10^{-20}\right]$ with $\alpha = 0.1$ and without the rocket effect.

Then from eq. 2.18,

$$n(f) \propto \left(aH\left(t_{\mathrm{c}}\right)\right)^{3} \propto t_{\mathrm{c}}^{-\frac{3}{2}}. \tag{3.20}$$

When loop decay is not significant, the gravitational wave emission frequency

$$f \propto \frac{1}{l} \propto \frac{1}{H\left(t_{\mathrm{c}}\right)} \propto \frac{1}{t_{\mathrm{c}}}. \tag{3.21}$$

Thus

$$N(f) \propto f^{\frac{3}{2}}. \tag{3.22}$$

When loop decay is not significant, the number of cosmic string loops in the Galaxy is simply a power-law of frequency. We can see clearly from fig. 3.1 that this is generally the case

at lower frequencies, where the loops are bigger and are created later, and therefore have not yet experienced significant loop decay. As loop decay is caused by energy loss through gravitational wave emission, loops with lower $G\mu$ experience slower decay and therefore enter the decay regime at a higher frequency. In fact, for the LISA frequency range, the decay regime is entirely absent for $G\mu \lesssim 10^{-20}$.

The flat region in fig. 3.1 represents the decay regime. We see that at $G\mu = 10^{-12}$ and 10^{-14}, loops emitting gravitational waves in the entire frequency range have decayed. Loops in the decay regime are created at about the same time, and therefore have similar number densities and sizes initially. However, from eq. 2.47, it is clear that the decay rate is independent of loop size, and therefore loops in the decay regime have very different sizes today, while their number densities remain similar. In the decay regime, loops with higher $G\mu$ are created much later in time, and so their number densities are lower.

The important point to note from fig. 3.1 is that cosmic string loops can be extremely abundant in the Galaxy, especially at lower $G\mu$. This is clearly not only true in the toy model, but is also the case in the physical model, as rebinning the number density decreases $N(f)$ by at most a factor of $\frac{1}{T_{\rm obs}}/0.1f \lesssim 3 \times 10^{-7}$. Tracking all cosmic string loops in the entire Galaxy is certainly far beyond current computational capabilities.

The solution here is to cleverly implement the Monte Carlo simulation such that only cosmic string loops closest to the solar system at $R_\odot = 8$ kpc are considered, i.e. only loops that matter the most are included in the simulation. For our purpose, it is then possible to recover the statistics for the entire Galaxy based on the outcome of the limited-scale simulation. We call this the "closest loops method". We verify both theoretically (below) and through simulations (section 3.2.1) that indeed statistics for the entire Galaxy can be recovered by utilizing the closest loops method.

Simulations of cosmic string loops in the Galaxy in search of harmonic gravitational wave signals from nearby loops have a signal side where the focus is on accounting for gravitational

wave signal from individual nearby loops, as well as a noise side, where the focus is on correctly generating gravitational waves from loops in the Galaxy that are not sufficiently close to the solar system to the point that their signals stand out individually. The latter population of loops are the background loops, and their gravitational wave emissions form the Galactic confusion for detecting signal from individual nearby loops.

The Galactic confusion at a given frequency is the result of superposition of gravitational waves emitted by all background cosmic string loops at that frequency. When simulated, this can vary significantly across nearby frequency bins even though the theoretical Galactic background is a slowly varying function of frequency as shown in fig. 2.5, because of the uncorrelated phases of gravitational waves from background loops. This variation in the Galactic confusion across nearby frequency bins can mimic to a certain extent signal from nearby individual loops. Thus, there are two components to the Galactic confusion for which our simulations need to account for. We call these the Galactic confusion background and the Galactic confusion noise. The former is the mean of the Galactic confusion $\bar{h}$ which is essentially the theoretically calculated Galactic background shown in fig. 2.5. The latter, $h_{\mathrm{n,c}}$, is the amount of variation in the Galactic background across nearby frequency bins due to interference of gravitational waves with uncorrelated phases.

For the closest loops method to work, it has to correctly account for both signal from individual nearby cosmic string loops, and the two components of the Galactic confusion. The method works in theory because of the following characteristics of the simulation:

First on the signal side, the likelihood of detecting signal from nearby individual loops at a given frequency, even with the toy model, is so low that most detections are attributed to just the single closest loop. These truly are soloists in the cosmic symphony. This is justified in section 3.3.1. Because of this fact, simulating a few nearby loops at each frequency is sufficient to account for the signal side of the simulation.

On the noise side of the simulation, we first discuss the Galactic confusion background

$\bar{h}$. Note that since overall the power of gravitational wave emission from background loops adds. Then from eq. 2.55, the mean strain amplitude

$$\bar{h} \propto \sqrt{N}. \tag{3.23}$$

For the Galactic confusion noise $h_{\mathrm{n,c}}$, it is a result of superposition of gravitational waves with uncorrelated phases, and therefore the overall amplitude

$$h_{\mathrm{n,c}} \propto \sqrt{N}, \tag{3.24}$$

because the interference of gravitational waves from background loops is effectively a 1D random walk on the noise strain amplitude.

Of course both the Galactic confusion background and the Galactic confusion noise are modulated by the geometry of spatial distribution of background loops in the Galaxy. However, when comparing eqs. 3.23 and 3.24, geometry cancels, and we are left with

$$\bar{h} \propto h_{\mathrm{n,c}}. \tag{3.25}$$

Notwithstanding the theoretical arguments above, eq. 3.25 is verified through simulation in section 3.2.1. As the Galactic mean $\bar{h}$ is known through theoretical calculations, eq. 3.25 enables us to recover the Galactic confusion noise $h_{\mathrm{n,c}}$ for the entire Galaxy by tracking only the closest subset of background loops. This completes the closest loops method, and as the rest of the chapter will show, it proves to be especially powerful for the interesting part of the parameter space where $N(f)$ is very large.

3.1.4 Simulation Setup

We vary both $G\mu$ and α with and without the rocket effect to produce simulation sets that cover the parameter space. Simulations are performed with initial loop sizes of the one-scale model at $\alpha = 0.1$ and $\alpha = 10^{-5}$. Generally, we run simulations with values of the string tension from $G\mu = 10^{-12}$ down to $G\mu = 10^{-20}$. These values are decreased in steps of $\Delta \log G\mu = 2$ for the case of $\alpha = 10^{-5}$. In the case of $\alpha = 0.1$, we include additional values of string tension $G\mu = 10^{-17}$ and 10^{-19}. Together, they span 24 parameter combinations.

We discussed in section 2.1.2 the reason these values of α are selected. The upper limit in tension of $G\mu = 10^{-12}$ is set initially because as discussed in chapter 1, as of the time of preparation of this manuscript, observational constraints have already eliminated cosmic string tension above $G\mu \sim 10^{-11}$ [93]. As it will become clear in the rest of this chapter, this upper limit in tension is in fact still far too high for the purpose of detecting harmonic gravitational waves from individual nearby loops. Our simulations stop at $G\mu = 10^{-20}$ because as discussed in sections 2.3.2 and 3.1.3, for string tension this low, both decay and rocket effect regimes are already outside of LISA frequency range, and further decreasing string tension only results in reduced strain amplitude of gravitational wave emission from loops without significantly increasing loop number density. Thus the possibility of detecting individual nearby cosmic string loops by LISA at tension below $G\mu = 10^{-20}$ only decreases and can in fact be inferred from results at $G\mu = 10^{-20}$.

We consider the three main sources of noise in our simulation:

1. The Galactic confusion due to gravitational waves emitted by background Galactic loops;

2. The stochastic background which is the unresolved background due to gravitational waves emitted by all cosmic string loops in the universe over all time;

3. LISA instrumental noise including both laser shot noise and position noise with the

Galactic WD binaries background.

We set $T_{\rm obs} = 1$ year for the noise level regardless of the frequency resolution that a given simulation set employs due to computational constraints, as our ultimate goal is to generate predictions for the possibility of detection over a 1-year mission period.

All simulation sets are performed in the peak LISA sensitivity frequency range $f \in \left[10^{-5}, 1\right]$ Hz, with frequency resolution $\Delta f = \frac{1}{T_{\rm obs}}$. For each simulation set, we run both signal side and noise side simulations with frequency resolution corresponding to $T_{\rm obs} =$ 1 month. For signal side, we run 100 realizations for each simulation set including the closest 10 loops to the solar system at each frequency to generate detection candidates. These loops form the "decet" of the cosmic symphony. Recall from section 3.1.3 that most detections are due to just the single closest loop, the decet simulations are sufficient to cover all possible detections. For noise side, we run 10 realizations for each simulation set including the closest 1000 loops to the solar system at each frequency to estimate the Galactic confusion utilizing the closest loops method discussed in section 3.1.3.

Additionally, we run 100 signal realizations with the rocket effect at $G\mu = 10^{-18}$, $\alpha = 0.1$, with frequency resolution corresponding to $T_{\rm obs} = 1$ year. Note that this simulation set effectively constitutes a different toy model from the 24 simulation sets above. It helps clarify the physical implications of simulating the toy models, while at the same time also serves as a consistency test when we renormalize results from the toy models in section 3.3.9.

We also run 5 low-resolution simulation sets with the rocket effect at $G\mu = 10^{-18}$, $\alpha = 0.1$, with frequency resolution corresponding to $T_{\rm obs} = 1$ day, including the closest 10 to 10^5 cosmic string loops to the solar system in log increments of 1 to verify the closest loops method discussed in section 3.1.3.

Gravitational wave emissions are modeled as isotropic in our simulation for simplicity. As directionality in gravitational wave emission by a cosmic string loop uncorrelated to our detector antenna pattern both enhances its signal and at the same time reduces detection

probability, this simplification should not have a significant impact on the results from our simulations for harmonic gravitational waves emitted by cosmic string loops which have a wide angular scale of emission as can be seen from eq. 2.44 and the discussion below eq. 2.45. The reader can refer to the works of refs. [33, 11] for studies on the possibility of detecting gravitational wave bursts from high frequency modes emitted by cosmic string loops.

We include higher harmonic modes of gravitational waves emitted by the loops through postprocessing for both cusps- and kinks-dominated emission spectra as discussed in section 2.2.2.

We incorporate the full effects of gravitational wave signal modulations due to LISA orbital motion discussed in section 2.4. The full location of each simulated cosmic string loop in the Galaxy (r, θ, ϕ) is randomly generated according to the distribution of loop number density in the Galaxy, as discussed in section 3.1.1. As the loops in the Galaxy are independent from each other, their orientations with respect to the solar system are random and uncorrelated. Thus, random inclinations ι are assumed for the loops, and they also emit gravitational waves with random polarization angles ψ. With these parameters, the full signal modulations due to LISA orbital motion averaged over a complete orbit are computed using eqs. 2.66 through 2.71.

3.2 Data Analysis

3.2.1 The Galactic Confusion

Fig. 3.2 presents an example of computing the Galactic confusion background $\bar{h}$ and the Galactic confusion noise $h_{\rm n,c}$ from a particular noise side realization at $G\mu = 10^{-18}$, $\alpha = 0.1$ including the 1000 closest loops to the solar system.

The first striking characteristic of the plot is the dramatic cliff-like feature at $f \sim 0.1$ Hz. This happens at the truncation frequency $f_{\odot}$, and the cliff is in fact the same dip barely

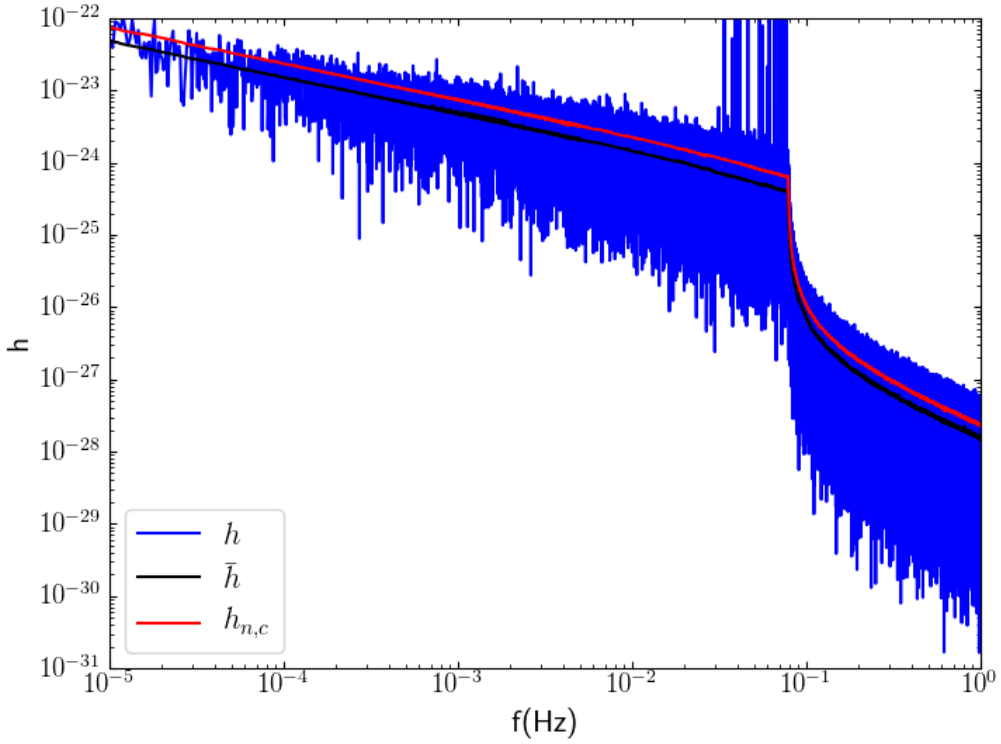

Figure 3.2: Snapshot of a noise side realization with the rocket effect at $G\mu = 10^{-18}$, $\alpha = 0.1$ including the 1000 closest loops to the solar system. The black line is the Galactic confusion background $\bar{h}$, and the red line is the Galactic confusion noise $h_{\mathrm{n,c}}$.

visible in fig. 2.5 caused by the rocket effect. The dip becomes very pronounced in fig. 3.2 and morphs into a cliff because the gravitational wave background from a majority of loops in the Galaxy is absent, as the realization only includes the closest 1000 loops. In this case, the drop in strain amplitude above $f_{\odot}$ is very significant, because the entire population of observable loops is effectively shifted further away for $f > f_{\odot}$, where distances to these loops suddenly become large because they are bound by the truncation radius.

Another striking feature of fig. 3.2 consists of the tall vertical lines present in the frequency range 0.01 Hz $\lesssim f \lesssim$ 0.1 Hz. These are in fact harmonic gravitational waves emitted by individual loops that happen to be extremely nearby. They are effectively the signal we looking for. However, as this is a noise side realization, the presence of such signal actually

presents a challenge. This is because they can be several orders of magnitude higher than the Galactic confusion noise, and therefore have the potential to greatly skew estimates for the Galactic confusion if not carefully excluded.

As the Galactic confusion background is a slowly varying function of frequency. We compute $\bar{h}$ and $h_{\mathrm{n,c}}$ at a particular frequency bin by considering strain amplitude in the neighborhood of this frequency bin with a size of 1% of the total number of frequency bins. We generate a histogram of the strain amplitude for each neighborhood. The quantities are then estimated by performing Gaussian fits to the histograms of the neighborhoods. This procedure of Galactic confusion estimation eliminates the effects of signals which should not be included in calculating the Galactic confusion, because such signals are located in the far-off tails of the histograms and have little effect on the Gaussian fits. The Galactic confusion noise $h_{\mathrm{n,c}}$ thus estimated may appear low visually in fig. 3.2 because of the great abundance of frequency bins at higher frequencies, to the point that the true distribution of strain amplitudes over the frequency bins cannot be adequately resolved in the plot.

The Galactic confusion obtained from fig. 3.2 is only that of a particular noise side realization. The overall Galactic confusion for the simulation set is computed by averaging over all noise side realizations in the simulation set.

We directly test the closest loops method by computing the Galactic confusion noise $h_{\mathrm{n,c}}$ and the Galactic confusion background $\bar{h}$ for $G\mu = 10^{-18}$, $\alpha = 0.1$, for simulation sets including the closest $\left[10^1, 10^2, 10^3, 10^4, 10^5\right]$ cosmic string loops to the solar system, averaged over $[96, 96, 96, 96, 10]$ realizations in each simulation set, respectively. We present the result at $f = 0.05$ Hz in fig. 3.3 because this frequency is in the frequency range where signals from nearby individual loops are common. The relation represented by the figure itself is general for all frequencies.

The 5 data points in fig. 3.3 from lower to higher strain amplitudes corresponding to the growing number of loops included in the simulation sets display a good linear relationship

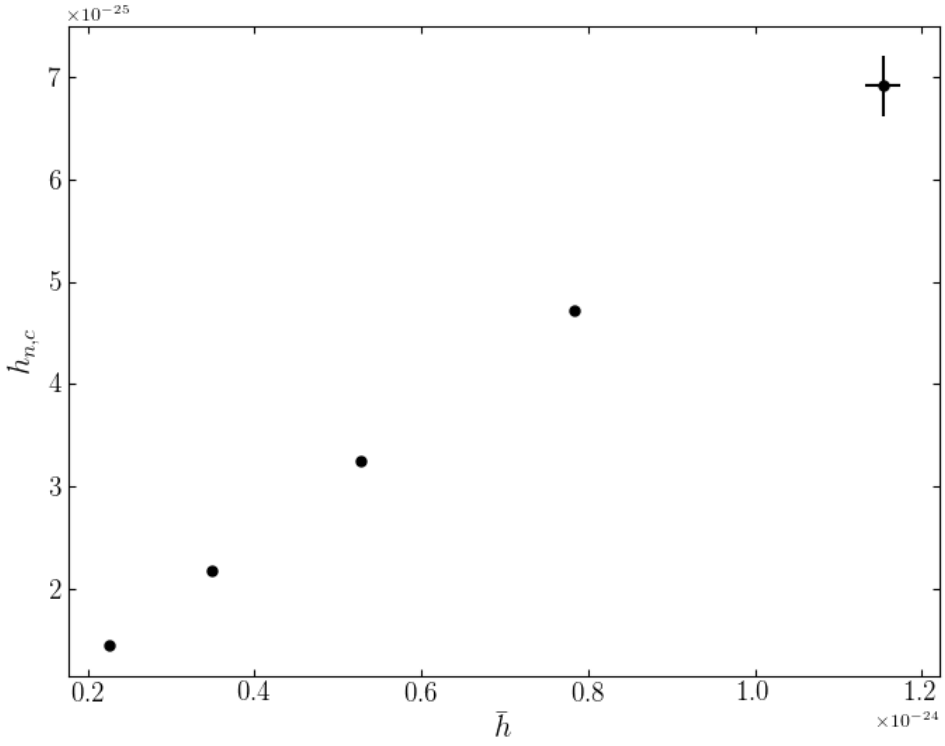

Figure 3.3: The Galactic confusion noise $h_{\rm n,c}$ as a function of the Galactic confusion background $\bar{h}$ for $G\mu = 10^{-18}$, $\alpha = 0.1$, at $f = 0.05$ Hz, computed for simulation sets including the closest $\left[10^1, 10^2, 10^3, 10^4, 10^5\right]$ cosmic string loops to the solar system, averaged over $[96, 96, 96, 96, 10]$ realizations in each simulation set, respectively.

as required by eq. 3.25. This test serves as a direct verification of the closest loops method in addition to the theoretical arguments presented in section 3.1.3.

By utilizing the closest loops method, we essentially extrapolate the line in fig. 3.3 at each frequency to compute the Galactic confusion noise $h_{\rm n,c}$ for the entire Galaxy. It is worth noting that the linear relationship holds down to a subset of just 10 loops and does start breaking down for even smaller subsets. Thus our noise side simulation sets which include 1000 loops are indeed sufficient for recovering the full Galactic confusion noise $h_{\rm n,c}$ through the closest loops method.

To recover the full $h_{\rm n,c}$, we first note that in a sense, the steep cliff in fig. 3.2 is an

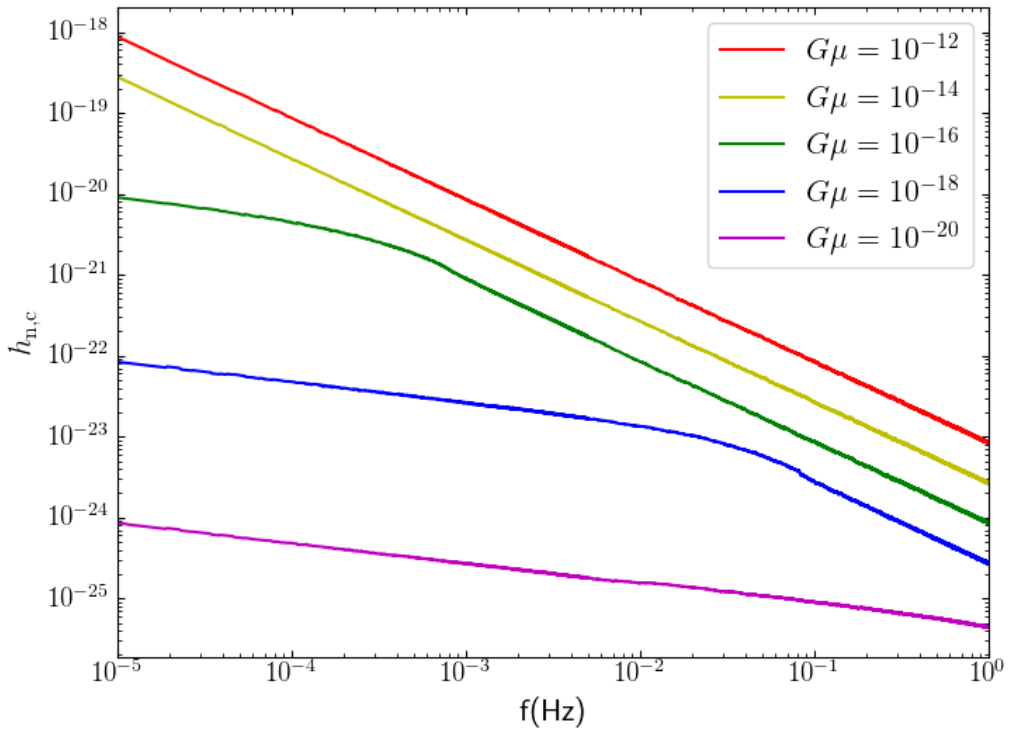

Figure 3.4: The full Galactic confusion noise $h_{\mathrm{n,c}}(f)$ with the rocket effect and $\alpha = 0.1$, computed using the closest loops method.

artificial feature caused by considering only a subset of cosmic string loops in the Galaxy. This feature therefore must go away if we correctly recover the true $h_{\mathrm{n,c}}$ through the closest loops method. This is indeed confirmed by fig. 3.4 showing the full Galactic confusion noise with the rocket effect and $\alpha = 0.1$ computed using the closest loops method. Clearly, the closest loops method fully recovers the small dips at $f_{\odot}$. In fact, notice how closely the shapes of the curves in fig. 3.4 resemble those in fig. 2.5, as required by eq. 3.25.

3.2.2 The Stochastic Background

Among the various quantities commonly used for expressing gravitational waves, the characteristic strain h_{c} is usually the most convenient quantity to work with for data analysis,

as it automatically incorporates the integration time over which the signal is observed. This is discussed in more detail in section 3.2.4 when we compute the signal-to-noise ratio.

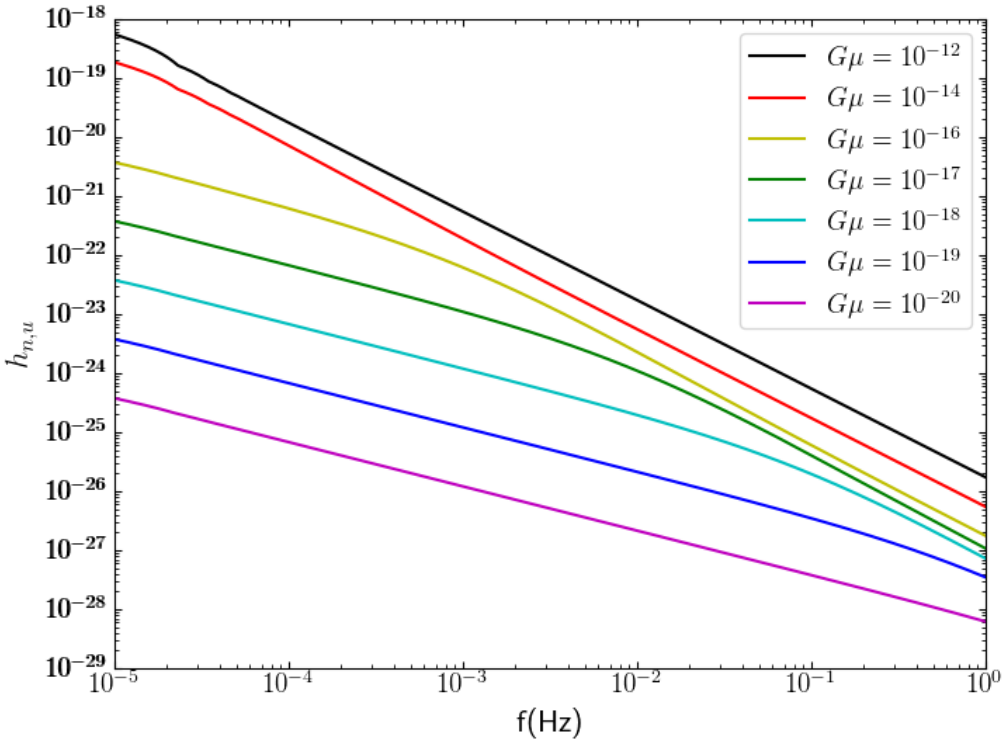

Figure 3.5: The effective strain amplitude $h_{\mathrm{n,u}}(f)$ of the stochastic background with $\alpha = 0.1$ and an integration time $T_{\mathrm{obs}} = 1$ year.

The stochastic background formed by unresolved gravitational waves emitted by all cosmic string loops in the universe over all time is computed in section 2.2.3, and displayed in fig. 2.3 as $\Omega_{\mathrm{g}}(f)$, the energy density spectrum in terms of the critical density of the universe ρ_c. This can be converted into the characteristic strain[71]

$$h_{\mathrm{c,u}}(f) = \frac{H_0}{\pi f}\sqrt{\frac{3\Omega_{\mathrm{g}}(f)}{2}}. \tag{3.26}$$

Since the stochastic background is really an unresolved gravitational wave background energy density, its actual strain amplitude cannot be simply defined, nor is that necessary as we

always work with the characteristic strain in our data analysis. However, as we will see in section 3.2.4, it is convenient for the practical purpose of carrying out the calculations to define an effective strain amplitude for the stochastic background

$$h_{\mathrm{n,u}}(f) \equiv \frac{h_{\mathrm{c,u}}(f)}{\sqrt{T_{\mathrm{obs}} f}}. \tag{3.27}$$

This quantity is plotted in fig. 3.5 with $\alpha = 0.1$ and an integration time $T_{\mathrm{obs}} = 1$ year. The change in slope in the figure comes from the transition displayed by the curves in fig. 2.3 characteristic of the stochastic background, with the steeper slope in fig. 3.5 at higher frequency corresponding to the flat region in fig. 2.3 where loop decay is significant.

3.2.3 Instrumental Noise and the Galactic WD Binaries Background

When a gravitational wave passes through the arms of the LISA spacecraft in the shape of an equilateral triangle formed by its three orbiters, it changes the lengths of the arms which translates into shifts in relative phases between emitted and reflected laser beams. LISA detects such gravitational waves by monitoring the relative phases of the beams in each arm. This working principle is not all that different from other laser interferometer gravitational wave detectors. The absolute floor of LISA instrumental sensitivity is therefore set by laser shot noise. However, unlike ground-based laser interferometer gravitational wave detectors, the orbiters of LISA are in separate heliocentric orbits and experience considerable variations in their relative positions capable of mimicking gravitational wave signals[30]. This is the position noise of the detector which dominates over the laser shot noise, and sets the floor of LISA instrumental sensitivity.

The level of signal necessary so that a signal-to-noise ratio of unity can be obtained from the LISA detector is defined to be its sensitivity curve. This is then interpreted as one of the sources of noise, i.e. the instrumental noise, in the data analysis for gravitational wave

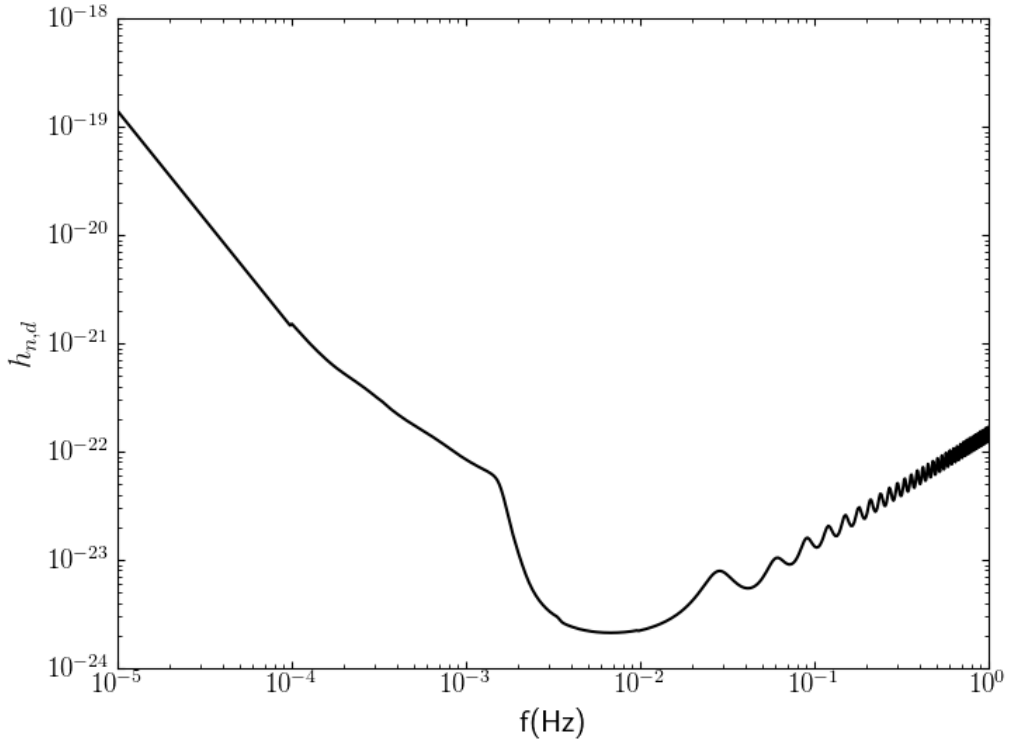

Figure 3.6: All-sky instrumental noise of LISA with standard detector configuration averaged over polarizations[6] merged with the Galactic WD binaries background[7] plotted as the strain amplitude $h_{\mathrm{n,d}}(f)$ with an integration time $T_{\mathrm{obs}} = 1$ year.

detection. We adopt standard all-sky LISA instrumental noise[6] averaged over polarizations with a standard triangular detector configuration with equilateral arms. Configuration parameters are listed in table 3.1. This LISA instrumental noise accounts for most of the features in fig. 3.6 which is plotted as the strain amplitude $h_{\mathrm{n,d}}(f)$ with an integration time $T_{\mathrm{obs}} = 1$ year, including the overall trend and the ringing at high frequency. The same as in section 3.2.2, the strain amplitude is defined in terms of the characteristic strain as

$$h_{\mathrm{n,d}}(f) \equiv \frac{h_{\mathrm{c,d}}(f)}{\sqrt{T_{\mathrm{obs}} f}}. \tag{3.28}$$

A major astrophysical source of noise in the LISA frequency range consists of the WD

Parameter	Value
Armlength	5×10^9 m
Telescope Diameter	0.3 m
Laser Wavelength	1064 nm
Laser Power	1 W
Optical Train Efficiency	0.3
Acceleration Noise	3×10^{-15} m/s^{2}Hz$^{\frac{1}{2}}$
Position Noise	2×10^{-11} m/Hz$^{\frac{1}{2}}$

Table 3.1: Standard configuration parameters[6] of the LISA spacecraft adopted by this study for estimating the instrumental sensitivity of the detector.

binaries population which is extremely abundant in the Galaxy. Their abundance in the halo of the Galaxy has been estimated to be[7] $N_{\rm WD} \sim 10^{12}$ in the LISA frequency range. This population of WD binaries is therefore a major source of gravitational waves in the Galaxy while remaining mostly unobservable through electromagnetic waves. WD binaries in this frequency range are in stable orbits far from the end of their inspirals, and are therefore essentially monochromatic gravitational wave emitters. Thus, they are particularly relevant for detecting harmonic gravitational waves from cosmic string loops in the Galaxy, and form an unresolved confusion background due to their abundance in the Galaxy.

The Galactic WD binaries background[7] has been included in fig. 3.6. The most prominent feature indicating its presence is the break at $f \sim 10^{-3}$ Hz. This feature is caused by the fact that the Galactic WD binaries background mostly contributes to frequencies below this break, and therefore the low-frequency region of the pure LISA instrumental noise curve is elevated. The fact that Galactic WD binaries mostly affect the low-frequency region of the LISA frequency range actually makes them less relevant for our purpose of detecting harmonic signal from individual cosmic string loops, because of the relatively low loop abundance in the low-frequency region since these larger loops are created later in time, as we discussed in section 2.3.2.

3.2.4 Signal-to-Noise Ratio

The general optimal signal-to-noise ratio for data analysis of gravitational wave detection is[77]

$$\varrho^2 = 4\int_0^\infty df \frac{\left|\tilde{h}(f)\right|^2}{S_{\rm n}(f)}, \tag{3.29}$$

where $\tilde{h}(f)$ is the Fourier transform of the time-domain strain of the gravitational wave signal, and $S_{\rm n}(f)$ is the noise root spectral density. Eq. 3.29 is a generic expression of the signal-to-noise ratio independent of the nature of the source emitting the gravitational wave, i.e. the functional form of $\tilde{h}(f)$. For monochromatic sources, the Dirac delta function in $\tilde{h}(f)$ kills the integral in eq. 3.29, and the signal-to-noise ratio at frequency f greatly simplifies to[77]

$$\varrho^2(f) = \frac{h(f)^2 T_{\rm obs}}{S_{\rm n}(f)}. \tag{3.30}$$

To proceed further, we turn our attention to the characteristic strain of monochromatic sources. This is achieved by analyzing the signal from a closely related type of sources of gravitational waves, inspiralling binaries[71]. These are quasi-monochromatic sources with well-defined frequencies that shift slowly over time compared to the timescale of the duration of observation. In order to calculate the characteristic strain of binary inspirals, we first compute the Fourier transform of their gravitational wave signal. Suppose that a binary inspiral emitting gravitational wave at f has strain amplitude h and slowly time-dependent phase $\phi(t)$ with $\phi(0) = 0$, then the Fourier transform of the time-domain signal is

$$\tilde{h}(f) = \frac{h}{2}\int_{-\infty}^{\infty} dt \left(e^{-i2\pi\left(f - \frac{\phi(t)}{2\pi t}\right)t} + e^{-i2\pi\left(f + \frac{\phi(t)}{2\pi t}\right)t} \right). \tag{3.31}$$

The dominant contribution to the integral eq. 3.31 comes from non-oscillating parts of the integrand, i.e. when

$$\frac{\phi(t)}{2\pi t} \sim \pm f. \tag{3.32}$$

Taylor expanding $f \pm \frac{\phi(t)}{2\pi t}$ with respect to 0, and substituting the leading term $\mathcal{O}(t)$ back into eq. 3.31, the Fourier transform becomes

$$\tilde{h}(f) \approx \frac{h}{2}\int_{-\infty}^{\infty} dt \left(e^{i2\pi\dot{f}t^2} + e^{-i2\pi\dot{f}t^2}\right) \approx \frac{h}{2\sqrt{\dot{f}}}. \tag{3.33}$$

The generic definition of the characteristic strain in terms of the Fourier transform is

$$h_{\rm c}(f)^2 \equiv 4f^2 \left|\tilde{h}(f)\right|^2. \tag{3.34}$$

Substituting the Fourier transform eq. 3.33 into eq. 3.34, the characteristic strain of a binary inspiral is[71, 94]

$$h_{\rm c}(f) \approx h(f)\sqrt{\frac{f^2}{\dot{f}}} = h(f)\sqrt{N_{\rm cyc}}, \tag{3.35}$$

where $N_{\rm cyc}$ should be interpreted as the number of wave cycles the binary inspiral emits gravitational wave in the frequency bin f.

A true monochromatic source can be thought of as a binary inspiral with $N_{\rm cyc} \to \infty$, making eq. 3.35 formally undefined. However, signal integration for monochromatic sources is still limited, just not by $N_{\rm cyc}$ but by the integration time $T_{\rm obs}$. Thus the correct identification of the characteristic strain for monochromatic sources is[71]

$$h_{\rm c}(f) = h(f)\sqrt{N_{\rm obs}} = h(f)\sqrt{T_{\rm obs}f}. \tag{3.36}$$

Now the signal-to-noise ratio for monochromatic sources at a frequency bin can be derived by substituting eq. 3.36 into eq. 3.30 and converting the noise root spectral density into characteristic strain,

$$\varrho^2(f) = \frac{h(f)^2 T_{\rm obs} f}{h_{\rm c,n}(f)^2} = \left(\frac{h_{\rm c,s}(f)}{h_{\rm c,n}(f)}\right)^2. \tag{3.37}$$

For monochromatic sources, the signal-to-noise ratio is simply the ratio of signal and noise

characteristic strains. Recall in sections 3.2.2 and 3.2.3, we defined the noise strain amplitudes $h_{\rm n,u}(f)$ (eq. 3.27) and $h_{\rm n,d}(f)$ (eq. 3.28). This is because it is more convenient practically in our simulations to divide both the numerator and the denominator of eq. 3.37 by $N_{\rm obs} = T_{\rm obs} f$. Thus, schematically the signal-to-noise ratio in our simulations is computed as

$$\varrho = \frac{h(f)}{\sqrt{\sum_i h_{\rm n,i}(f)^2}}, \tag{3.38}$$

where the sum is over all sources of noise included in the simulation. As cosmic string loops in the Galaxy are persistent sources of gravitational waves when we focus on their harmonic emission, we require a relatively low

$$\varrho \geq 3 \tag{3.39}$$

for an event to be counted.

3.3 Results

3.3.1 Signal from Nearby Loops

We first present results from the simulation illustrating the validity of the closest loops method on the signal side as discussed in section 3.1.3. The snapshots from a particular realization in the signal side simulation set with the rocket effect at $G\mu = 10^{-18}$, $\alpha = 0.1$ are plotted in fig. 3.7. For visual clarity, we select the realization with the lowest number of events satisfying the signal-to-noise requirement eq. 3.39 for this purpose. The total power of gravitational wave emission is concentrated in the fundamental mode in this section in order to avoid unnecessary complication irrelevant to the central issue of this section.

The upper panel of fig. 3.7 reflects the normal method with which our simulation is performed and its results analyzed, where the closest 10 cosmic string loops for each frequency bin are included in the signal side simulation ("decet"). There are 13 events registered in

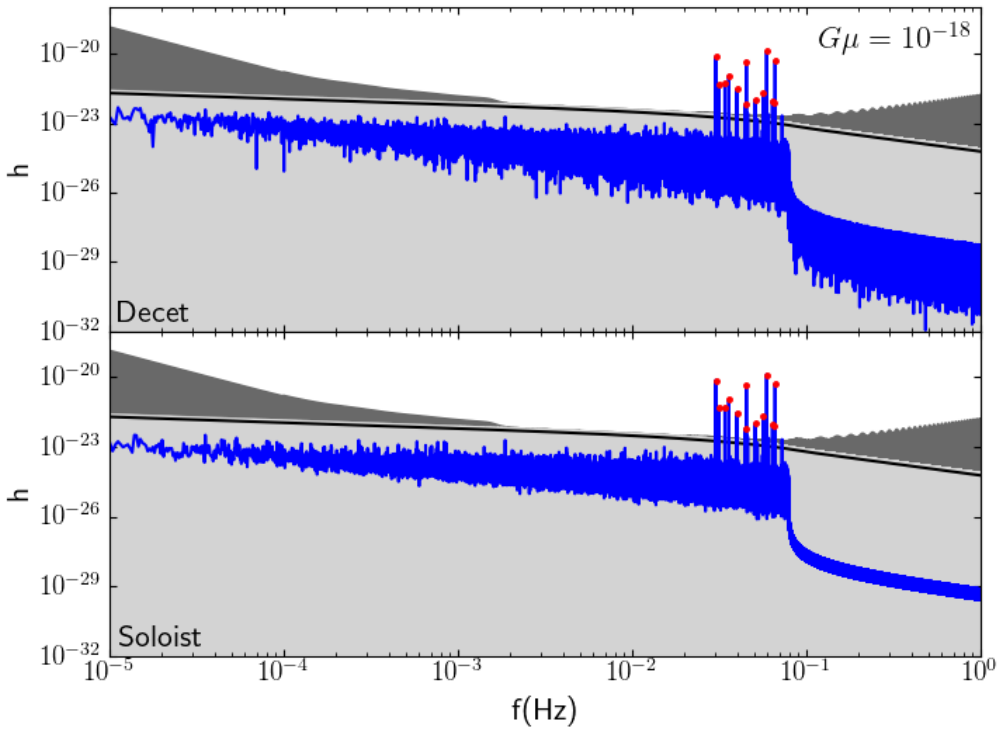

Figure 3.7: Snapshots of a particular realization in the signal side simulation set with the rocket effect at $G\mu = 10^{-18}$, $\alpha = 0.1$. The upper panel displays signal including the closest 10 loops for each frequency bin ("decet"). The lower panel displays only signal from the closest single loop for each frequency bin for the same snapshot ("soloist"). For both panels, the blue curve is the signal strain amplitude, and the black curve is the Galactic confusion background. The shaded regions from lighter to darker shades of grey represent the cumulative inclusion of sources of noise from: the Galactic confusion noise, the stochastic background, and the LISA instrumental noise merged with the Galactic WD binaries background, respectively. The red dots indicate events that satisfy the signal-to-noise requirement eq. 3.39.

total. The same data analysis process is repeated for the lower panel, where instead of being from the closest 10 loops, the signal for each frequency bin comes from only the closest single loop ("soloist") for the same snapshot. We again register 13 events in total that are identical to those in the upper panel. This comparison serves as a clear illustration that all the event signal is in fact due to just a single cosmic string loop being located extremely closely to the solar system, and is not a result of the combined contribution of gravitational waves emitted by multiple nearby loops.

The particular realization shown in fig. 3.7 is a motivating example illustrating the fact that most events registered in the simulation are attributed to signal from just the single closest cosmic string loop. To conclusively validate this fact, we compare results for all realizations in the simulation set. As the realizations are all identically prepared and independently performed, results for simulation sets are most suitably presented in a statistical fashion. The histograms in fig. 3.8 cover the same simulation set with the rocket effect at $G\mu = 10^{-18}$, $\alpha = 0.1$, with the difference that one (magenta) is generated by events registered by including contribution from the closest 10 loops for the signal side ("decet"), and the other (cyan) is generated by events registered by considering only signal from the closest single loop for the signal side ("soloist").

Visually, it is clear that the histograms in fig. 3.8 are essentially identical, with the exception of a single event in a single realization which appears to be absent when considering only signal from the closest single loop for a frequency bin. Statistically, the numbers of events computed from both histograms are also identical,

$$E_{\mathrm{D}} = 24 \pm 5; \tag{3.40}$$

$$E_{\mathrm{S}} = 24 \pm 5. \tag{3.41}$$

Thus, most of the events registered in the entire simulation set can in fact be attributed to just single cosmic string loops which happen to be located extremely closely to the solar

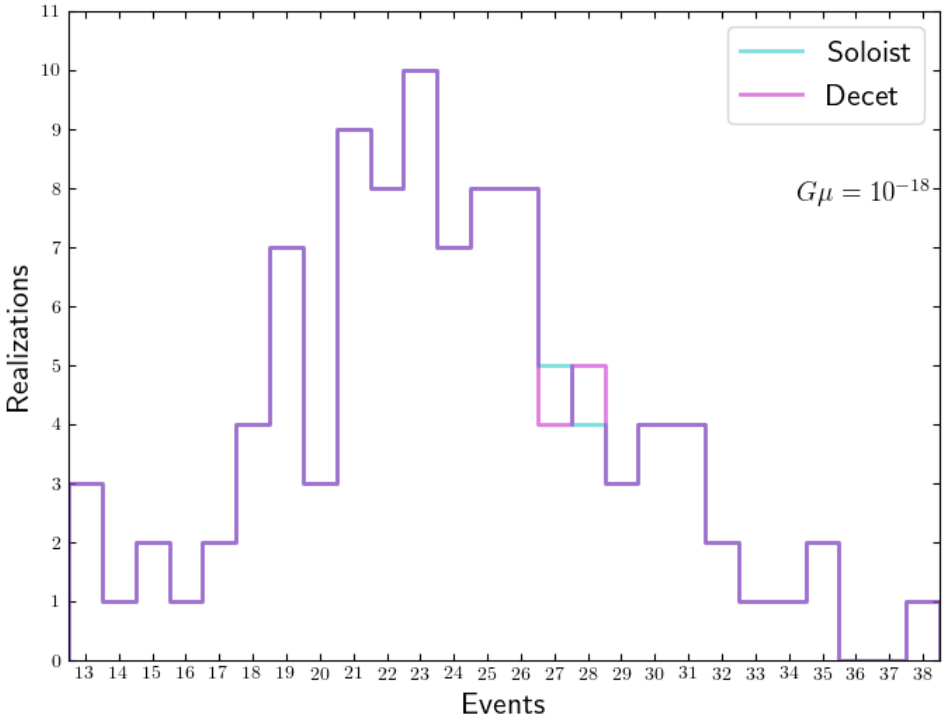

Figure 3.8: Histograms of events satisfying the signal-to-noise requirement eq. 3.39 for the simulation set with the rocket effect at $G\mu = 10^{-18}$, $\alpha = 0.1$. The histogram in magenta includes the closest 10 loops for each frequency bin ("decet"). The histogram in cyan includes only the closest loop for each frequency bin for the same simulation set ("soloist").

system. These truly are soloists in the cosmic symphony.

It will become clear in section 3.3.6 that we choose this simulation set to perform the comparison between "decets" and "soloists" because this is the part of the parameter space that is relevant, where the number of cosmic string loops in the Galaxy is very high (see section 3.1.3) and the number of events registered is plentiful. These ensure the relevance and generality of the result obtained, that the signal side of the simulation can actually be performed by tracking just the single closest loop for each frequency bin.

Physically, the result obtained means that even at such high number densities in the toy model, the probability that a single cosmic string loop happens to be located sufficiently nearby to be detected individually is still quite low, to the point that one has to be very lucky to have just one such occurrence. Since loops in the Galaxy are independent of each other, the probability of multiple such occurrences in the same frequency bin decreases exponentially. Thus, tracking not just the single closest loop, but the closest 10 loops for each frequency bin for the signal side is a configuration which safely ensures that our simulation accurately accounts for all the potential event candidates in the Galaxy. Coupled with the noise side discussion from section 3.2.1, this result makes sure that despite constraints on computational capabilities, our simulation is a reasonable representation of cosmic string loops in the Galaxy for the purpose of this study. All signal side simulation sets discussed hereafter in this manuscript are understood to include gravitational wave signal from the closest 10 loops for a frequency bin.

3.3.2 Gravitational Wave Emission Spectrum

The computationally viable means of incorporating higher harmonic modes of different gravitational wave emission spectra of cosmic string loops into our simulation is through postprocessing the fundamental strain amplitude in each realization. As discussed in section 3.1.2, the total strain amplitude at a given frequency as a result of superposition of gravitational

waves from all loops emitting at that frequency is a plane wave by the harmonic addition theorem, with total strain amplitude and overall phase given by eqs. 3.15 and 3.18, respectively. This means that for the purpose of incorporating higher harmonics into the simulation, only these two quantities are necessary. The procedure is implemented from lower to higher frequencies, and consists of first renormalizing the fundamental strain amplitude according to eq. 2.41, then distributing the power into higher harmonics according to eqs. 2.43 and 2.45, and lastly computing the superposition of these higher harmonics with existing gravitational waves at those frequencies. This procedure avoids the burden of tracking higher harmonics for each loop in the simulation, and it can be completed by postprocessing, thus enabling us to incorporate different gravitational wave emission spectra relatively easily and quickly. All relevant noises in the simulation are processed accordingly for consistency.

A disadvantage of the above method for incorporating higher harmonic modes into the simulation is that the very low-frequency region of our frequency range is missing contribution from higher harmonics of gravitational waves emitted by loops whose fundamental modes are below the frequency range. The primary effect of this is a slight reduction in the Galactic confusion in the very low-frequency region. This is unimportant for our purpose for several reasons. First, the reduction is not very significant because the fundamental mode dominates in any gravitational wave emission spectrum, and after distributing power to higher harmonics, the fundamental strain amplitude itself is only reduced by a factor of $\sim \sqrt{2}$. Second, the strain amplitudes of higher harmonics decrease rapidly as n becomes larger due to f in the denominator of eq. 2.55 in addition to the power-law spectrum itself. Thus, the underestimation to the Galactic confusion is in fact very slight, as discussed in ref. [31]. Third, the rapid decrease of the strain amplitude for higher harmonics means that this effect is only relevant for a narrow band in the low-frequency range $f \lesssim 5 \times 10^{-5}$ Hz. As will become clear in section 3.3.6, this low-frequency band is irrelevant for simulation sets in the important part of the parameter space, due to a combination of low loop number density at

those frequencies and the fact that in these simulation sets, the instrumental noise with the Galactic WD binaries background greatly dominates over the Galactic confusion at those frequencies. One final argument for the unimportance of the missing contribution of higher harmonics for very low frequencies is the fact that the effects of higher harmonics themselves are actually quite minimal for the purpose of our simulation, as will become clear below.

We now present results from the simulation illustrating any effects gravitational wave emission spectra may have on our simulation results. As an example, we select the same realization in the signal side simulation set with the rocket effect at $G\mu = 10^{-18}$, $\alpha = 0.1$ as the one selected in section 3.3.1, and present the snapshots in fig. 3.9.

The top panel displays the signal when all the power of gravitational wave emission is concentrated in the fundamental mode. This panel is in fact identical to the upper panel of fig. 3.7. There are again 13 events registered in total which satisfy the signal-to-noise requirement eq. 3.39. The lower two panels of fig. 3.9 display snapshots of the same realization when some power of gravitational wave emission is distributed in higher harmonics, with loops in the middle panel having the cusps-dominated spectrum (eq. 2.43) and those in the bottom panel having the kinks-dominated spectrum (eq. 2.45). We repeat the data analysis procedure for these two cases. In order to have a fair comparison, we configure our data analysis procedure to only look at the fundamental mode for event registration for the two cases where some power of gravitational waves exists in higher harmonics, i.e. we do not require coincident detection of higher harmonics of a fundamental mode signal even though we surely can for these two cases. We of course eliminate false events by carefully avoiding higher harmonics of events whose fundamental modes have already been registered. Such higher harmonics belonging to signal of events already registered are clearly visible at high frequency in the lower two panels. There are 11 and 12 events registered in total for signals with the cusps- and kinks-dominated spectra, respectively.

The important point here is that gravitational wave emission spectra do not have signif-

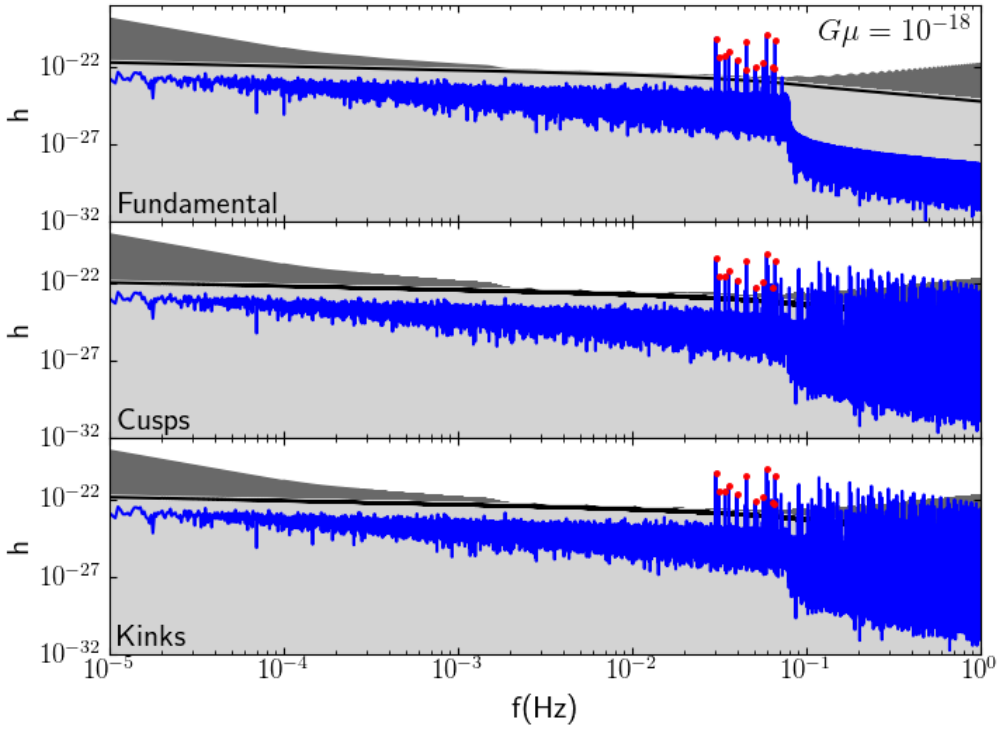

Figure 3.9: Snapshots of the same realization as that shown in fig. 3.7 in the signal side simulation set with the rocket effect at $G\mu = 10^{-18}$, $\alpha = 0.1$. Please refer to the caption of fig. 3.7 for an explanation of the layout of the plot. The panels from top to bottom display snapshots of this particular realization with three distributions of the power of gravitational wave emission by a loop: all concentrated in the fundamental mode, distributed according to the cusps-dominated spectrum, distributed according to the kinks-dominated spectrum, respectively.

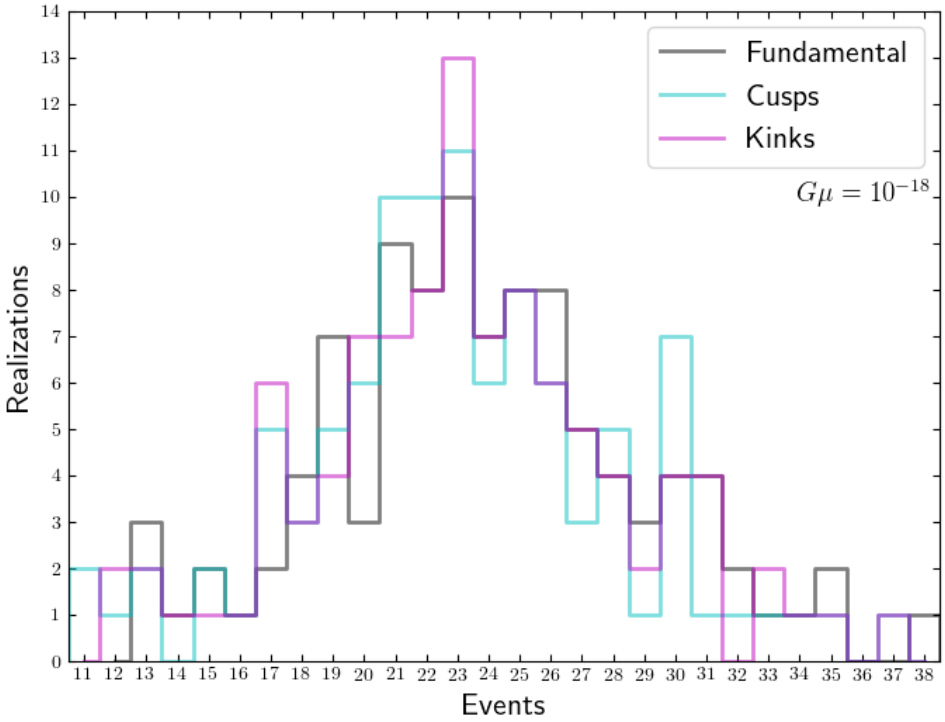

Figure 3.10: Histograms of events satisfying the signal-to-noise requirement eq. 3.39 for the simulation set with the rocket effect at $G\mu = 10^{-18}$, $\alpha = 0.1$. The histogram in grey is for when all power of gravitational wave emission is concentrated in the fundamental mode. The histograms in cyan and magenta are for when some power is distributed in higher harmonics according to the cusps- and kinks-dominated gravitational wave emission spectra, respectively.

icant effects on the results of our simulation. The slight differences in the total numbers of events registered for the three panels in fig. 3.9 can be understood quite simply. The signal-to-noise ratio is of course maximized when all the power of gravitational waves is concentrated in the fundamental mode, and hence the highest total number of events registered in that case. The signal-to-noise ratio is reduced when some power of gravitational wave emission is distributed in higher harmonics, due to both a reduction in signal strain amplitude in the fundamental mode and an enhancement in the Galactic confusion at higher frequency. This effect is more pronounced for the shallower power-law of the cusps-dominated spectrum. Thus, the case with the cusps-dominated spectrum registers the fewest events while that with the steeper kinks-dominated spectrum registers a total number of events in between those of the other two cases.

Again, the particular realization shown in fig. 3.9 is an example illustrating the fact that gravitational wave emission spectra do not have a significant effect on the results of our simulation. A full comparison of the three cases has to be made by comparing results from all realizations in the simulation set statistically, with histograms shown in fig. 3.10 for the same simulation set with the rocket effect at $G\mu = 10^{-18}$, $\alpha = 0.1$. Minor differences in the detailed features notwithstanding, the histograms for the three models of gravitational wave emission spectra have similar overall shapes and statistical properties, with total numbers of events registered

$$E_{\rm F} = 24 \pm 5; \tag{3.42}$$

$$E_{\rm C} = 23 \pm 5; \tag{3.43}$$

$$E_{\rm K} = 23 \pm 5. \tag{3.44}$$

As discussed above, the case when all the power of gravitational wave emission is concentrated in the fundamental mode maximizes the signal-to-noise ratio, and is therefore expected to

have the highest total number of events registered. However, statistically the results of our simulation are not at all sensitive to gravitational wave emission spectra when no coincident detections of higher harmonics are required.

3.3.3 Coincident Detection of Harmonic Modes

We now turn our attention to coincident detections of higher harmonic modes in the signal. A key signature of low-frequency gravitational wave signal from nearby individual cosmic string loops is its harmonic nature, i.e. the presence of higher harmonic modes at frequencies that are integer multiples of the fundamental frequency. This signature is unique to gravitational waves emitted by cosmic string loops, and cannot be replicated by any other types of astrophysical sources of gravitational waves. It would be inconceivable if we did not take advantage of this unique signature in search of harmonic signal from nearby individual loops.

As discussed in section 3.2.3, the type of astrophysical source of gravitational waves most capable of causing confusion with Galactic cosmic string loops consists of WD binaries in the Galaxy. While the confusion background formed by these sources have been incorporated into our noise model, with an abundance as high as $N_{\mathrm{WD}} \sim 10^{12}$ in the Galaxy [7], they quite possibly have the potential to mimic the signal we are looking for as well, should one happen to be located extremely nearby to the solar system. While a detailed study of the possibility of detecting such signal from WD binaries similar to this one for cosmic string loops would be beneficial for its own merit, it is not necessary for the purpose of our study. This is because WD binaries are not harmonic sources of gravitational waves. While they are also persistent sources of essentially monochromatic gravitational waves, which can certainly cause confusion with individual harmonic modes of gravitational waves emitted by cosmic string loops, they are unable to consistently mimic the higher harmonics of the latter, and therefore can easily be excluded by requiring coincident detections of higher harmonics for

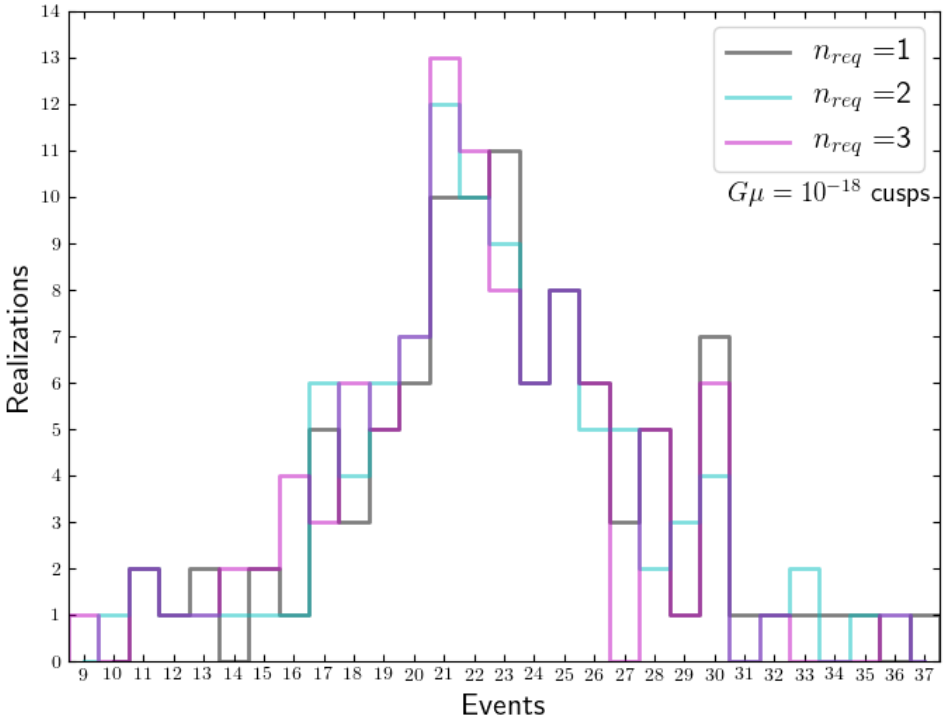

Figure 3.11: Histograms of events satisfying the signal-to-noise requirement eq. 3.39 for the simulation set with the rocket effect at $G\mu = 10^{-18}$, $\alpha = 0.1$, computed with the cusps-dominated gravitational wave emission spectrum. The histogram in grey is for when coincident detections of higher harmonics are not required for event registration. The histograms in cyan and magenta are for when coincident detections of the the first one and two harmonics are required for event registration, respectively.

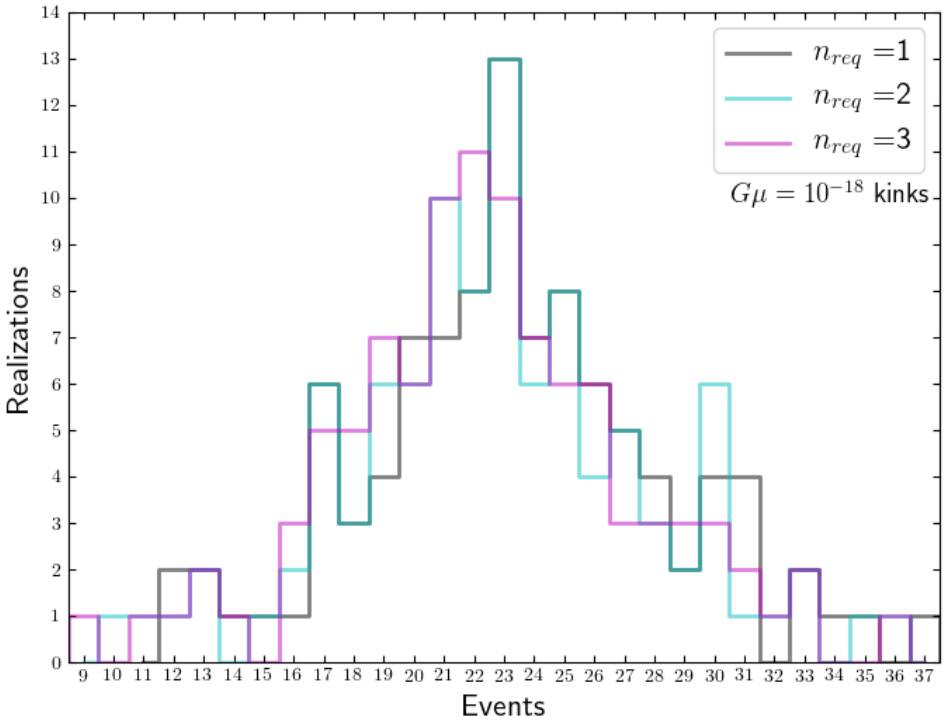

Figure 3.12: The histograms are the same as those in fig. 3.11 with the exception that they are computed with the kinks-dominated gravitational wave emission spectrum.

candidate events. Even though $N_{\rm WD} \sim 10^{12}$ appears high, our results (fig. 3.7) have already shown that even with a total number of loops in the Galaxy that is orders of magnitude higher in the toy model, the probability that a particular source happens to be located sufficiently closely to the solar system that it can be individually resolved out of even just the confusion of other such Galactic sources is still quite low. This means that we would be lucky to have a few WD binaries in the Galaxy whose gravitational wave signals are individually resolvable, and therefore the likelihood of multiple such sources consistently mimicking the harmonic signature of individual nearby cosmic string loops is negligible.

While requiring coincident detections of higher harmonics in the gravitational wave signal of nearby individual loops for event registration effectively eliminates false events caused by other types of sources with potentially confusing signal, such as WD binaries in the Galaxy, registration of real events should not be significantly affected as long as we do not require coincident detections of an excessive number of harmonic modes. As discussed earlier, strain amplitudes of harmonic modes decrease rapidly for higher harmonics, merging into noise. Thus if the coincident detection requirement is too high, legitimate events with relatively lower signal-to-noise ratios will be excluded.

We verify the statement above by comparing statistical results for the simulation set with the rocket effect at $G\mu = 10^{-18}$, $\alpha = 0.1$ with different levels of coincident detection requirements. The histograms of events for the same simulation set computed with the cusps- and kinks-dominated gravitational wave emission spectra are presented in figs. 3.11 and 3.12, respectively. We set requirements for coincident detections of higher harmonics in the signal for event registration as no requirement (grey), at most the 1st harmonic mode (cyan), at most the 2nd harmonic mode (magenta). Histograms of the first case correspond to the cyan and magenta histograms shown in fig. 3.10. The requirements for the latter two cases are "at most" to accommodate the situation when high harmonics of an event are outside of our frequency range. The signal-to-noise ratio requirement eq. 3.39 is modified

according to the relative signal strengths of higher harmonics.

We see that again, minor differences in the detailed features notwithstanding, histograms in each figure all have similar shapes and statistical properties. It is somewhat noticeable that the histogram for the case when two harmonic modes are required for event registration appears to have its peak shifted slightly to the left. The histograms give us the following event numbers

$$E_{\mathrm{C},1} = E_{\mathrm{K},1} = 23 \pm 5; \tag{3.45}$$

$$E_{\mathrm{C},2} = E_{\mathrm{K},2} = 23 \pm 5; \tag{3.46}$$

$$E_{\mathrm{C},3} = E_{\mathrm{K},3} = 22 \pm 5. \tag{3.47}$$

The results tell us that requiring coincident detection of the first harmonic for event registration appears to be the sweetspot where we can already effectively reap the benefit of being able to eliminate confusing signals from other types of gravitational wave sources, while including all legitimate events that are truly due to signal from nearby individual cosmic string loops. As expected from section 3.3.2, event registration is not sensitive to different gravitational wave emission spectra. Recall from section 2.2.2, cusps are dominant features of cosmic string loops. Thus, unless otherwise specified, we always quote results with the cusps-dominated gravitational wave emission spectrum requiring coincident detection of the first harmonic mode for event registration in later sections of this chapter.

3.3.4 Effects of Orbital Modulations

We discussed effects of signal modulations as orbiters of the LISA spacecraft travel in their heliocentric orbits in section 2.4. In order to correctly estimate the Galactic confusion as discussed in section 3.1.3, it is necessary to have some understanding of the effects orbital modulations have on the overall gravitational wave signal over a distribution of cosmic string

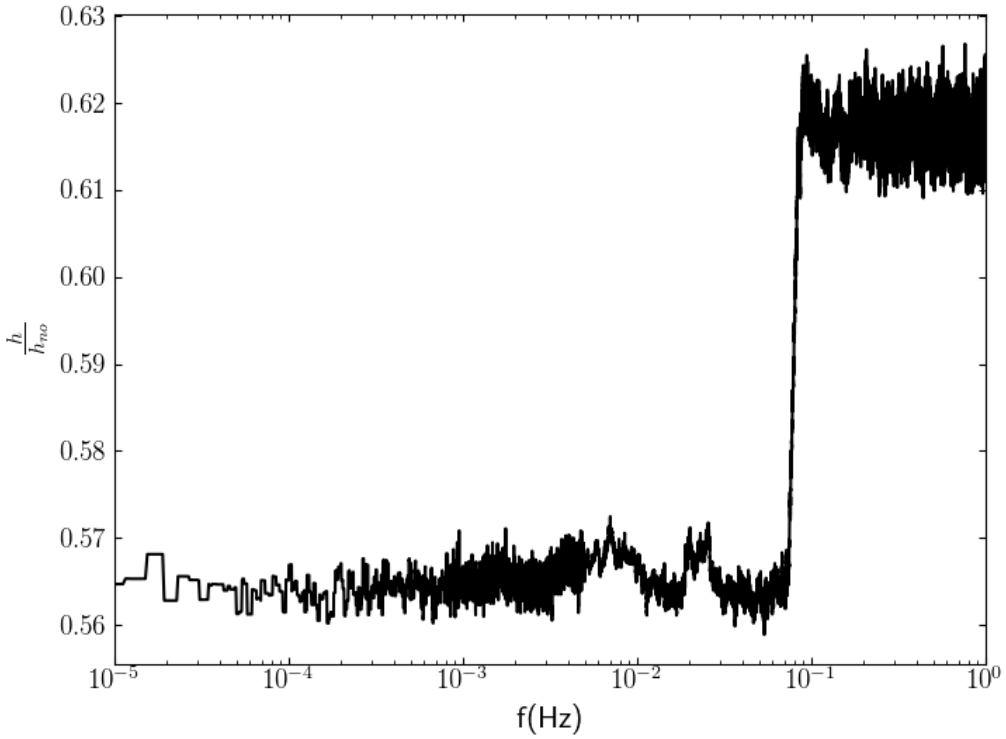

Figure 3.13: The ratio of strain amplitude modulated by LISA orbital effects over a period of $T_{\rm obs} = 1$ year over that without modulations, both from signal side simulation sets with the rocket effect at $G\mu = 10^{-18}$, $\alpha = 0.1$, averaged over all realizations.

loops. Orbital modulations on gravitational waves received from each loop are of course dependent on the exact location of that loop in the Galaxy. These are automatically incorporated into our simulation. Here we would like to take a look at the overall effect of orbital modulations over a distribution of loops in an averaged sense.

The ratio of strain amplitude with LISA orbital modulations over one orbit over that without modulations as a function of frequency is presented in fig. 3.13. Both strain amplitudes are averages over all realizations in signal side simulation sets with the rocket effect at $G\mu = 10^{-18}$, $\alpha = 0.1$. We see that the overall effects of LISA orbital modulations on gravitational waves from a distribution of loops are well-defined over the distribution, and are in fact not very strong, approximately halving the strain amplitude. One interesting feature worth noting is the sudden jump at $f \sim 0.1$ Hz. Recall from section 2.3.2, this is actually the rocket effect truncation frequency $f_\odot$. The feature probably comes as a result of the sudden change in spatial symmetry for the distribution of loops. For $f < f_\odot$, the truncation radius $r_{\rm tr}(f) > r_\odot$, and the loops are distributed around the solar system more or less isotropically with only large scale asymmetry given by the halo profile discussed in section 3.1.1. While for $f \gtrsim f_\odot$, $r_{\rm tr}(f) \lesssim r_\odot$, and all gravitational waves now come from the side where the center of the Galaxy is located. Even though the change in spatial symmetry of loop distribution is quite significant, the corresponding change to the averaged effects of LISA orbital modulations is not. Whether the reduction in strain amplitudes due to LISA orbital modulations is a factor of 0.55 or 0.6 is really not important for our purpose, as the corresponding change to the signal-to-noise ratio due to a slight shift of the Galactic confusion has little effect on the statistics of event registration. This is especially true for simulation sets in the interesting part of the parameter space where noise is not dominated by the Galactic confusion, as we will see in section 3.3.6. Effects of LISA orbital modulations are always included in all results presented.

3.3.5 String Tension

To analyze the effects varying string tension $G\mu$ has on the results of detecting harmonic gravitational wave signal from individual nearby cosmic string loops, we compare statistical results of event registration satisfying the signal-to-noise ratio requirement eq. 3.39 for simulation sets at $\alpha = 0.1$ without the rocket effect and with $G\mu$ varying from 10^{-12} to 10^{-20}. The results are presented in figs. 3.14 through 3.20. A summary of results including those presented in this section can be found in table 3.2. As will become clear in sections 3.3.6 and 3.3.7, this selection of simulation sets maximizes total numbers of events registered, thereby giving the most informative results for the main issue of this section, while precluding complications not pertinent to the main issue discussed presently.

We observe that the most prominent feature of the statistical results for these simulation sets is the fact that a relatively large number of events are registered for the case with the highest string tension $G\mu = 10^{-12}$. Then the number of events registered just falls off a cliff as $G\mu$ decreases, before it starts increasing again and peaks at $G\mu = 10^{-18}$, after which the number of events registered again drops.

To explain this feature observed, we note that a large number of events registered can be generated in two ways. The first way is to have strong gravitational wave emission from each loop. This effectively makes sources of noise other than the Galactic confusion less relevant, and the harmonic gravitational wave signal from an individual nearby loop can be detected without requiring this loop to be located in extreme proximity to the solar system, as the signal only has to stand out over the Galactic confusion. The probability that a loop is located sufficiently closely to the solar system to be able to overwhelm the Galactic confusion is not dependent on the strength of gravitational wave emission from each loop, as the Galactic confusion is just the collective emission of all loops. As $h \propto G\mu$ from eq. 2.55, this way favors higher string tension to ensure that sources of noise other than the Galactic confusion are subdominant. The second way of having a large number of events registered

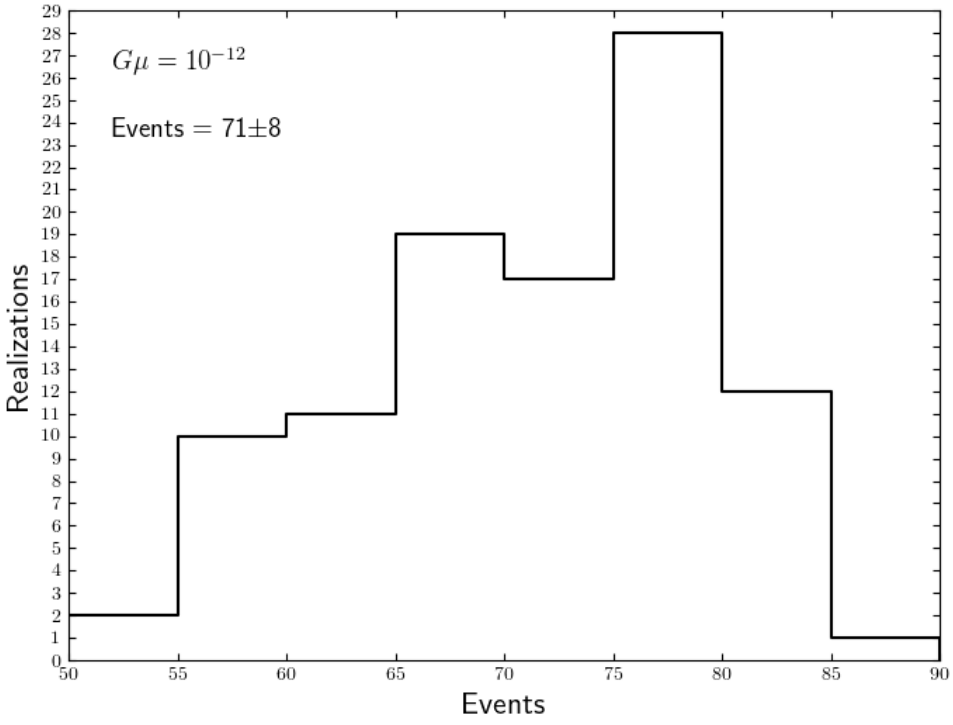

Figure 3.14: Histogram of events satisfying the signal-to-noise requirement eq. 3.39 for the simulation set without the rocket effect at $G\mu = 10^{-12}$, $\alpha = 0.1$.

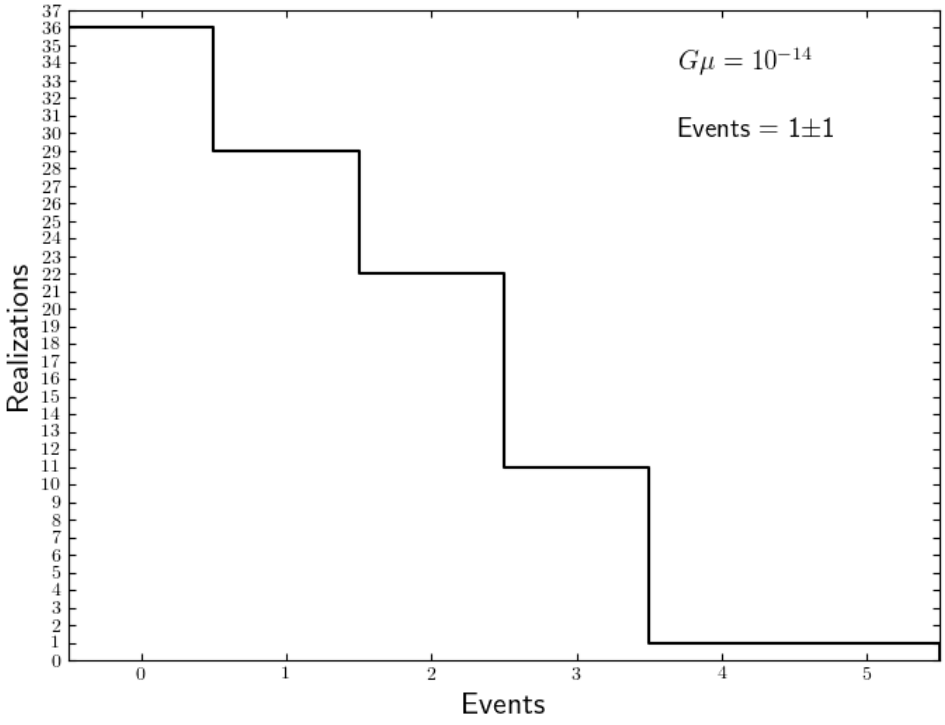

Figure 3.15: The same histogram as that shown in fig. 3.14 except that the simulation is performed with $G\mu = 10^{-14}$.

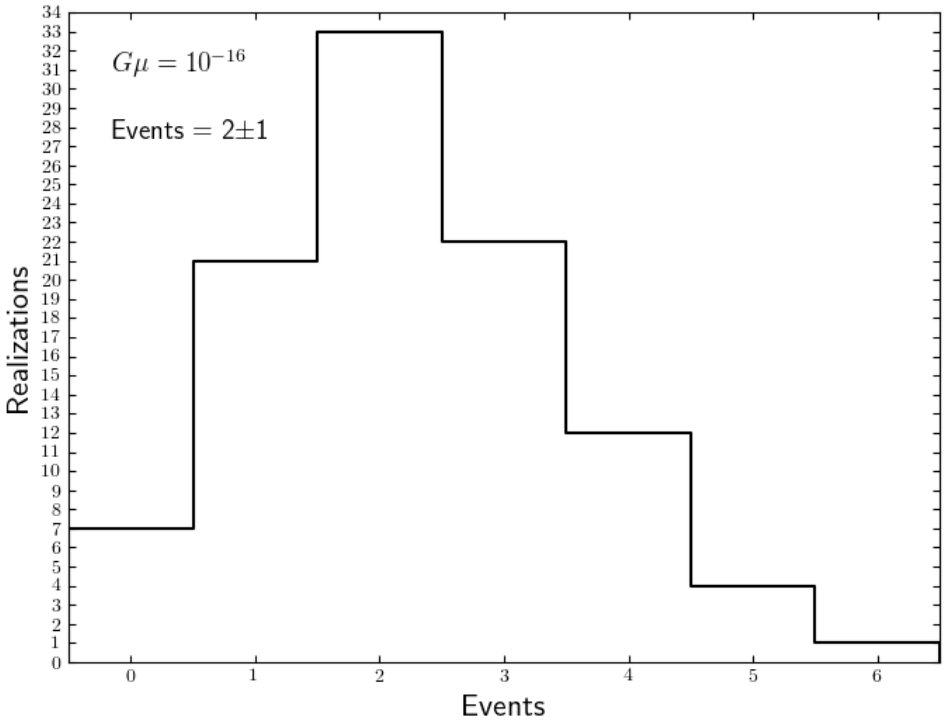

Figure 3.16: The same histogram as that shown in fig. 3.14 except that the simulation is performed with $G\mu = 10^{-16}$.

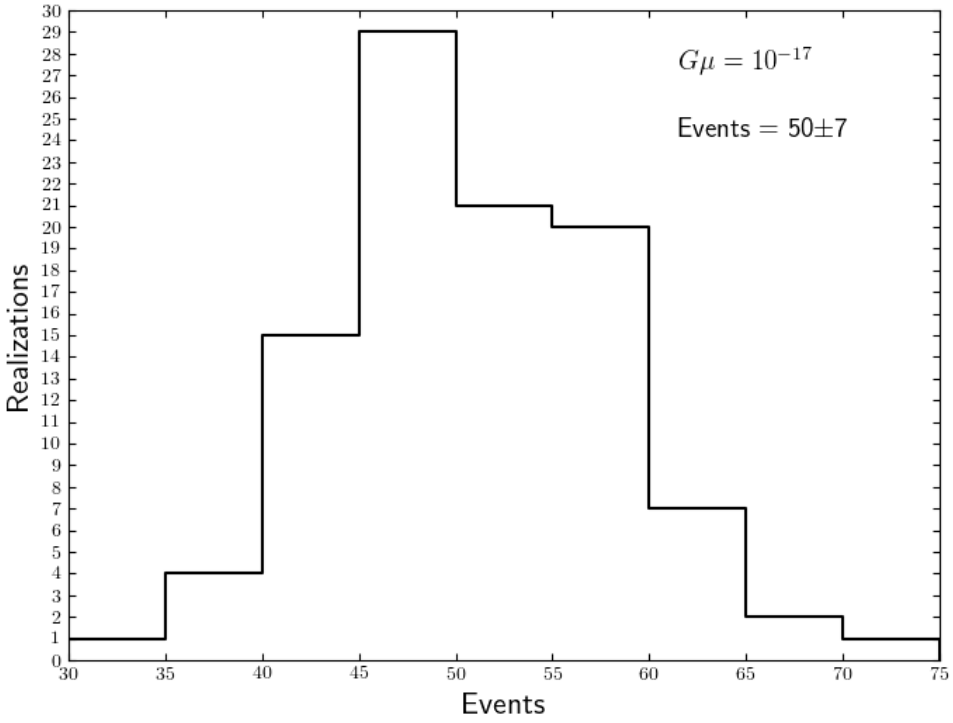

Figure 3.17: The same histogram as that shown in fig. 3.14 except that the simulation is performed with $G\mu = 10^{-17}$.

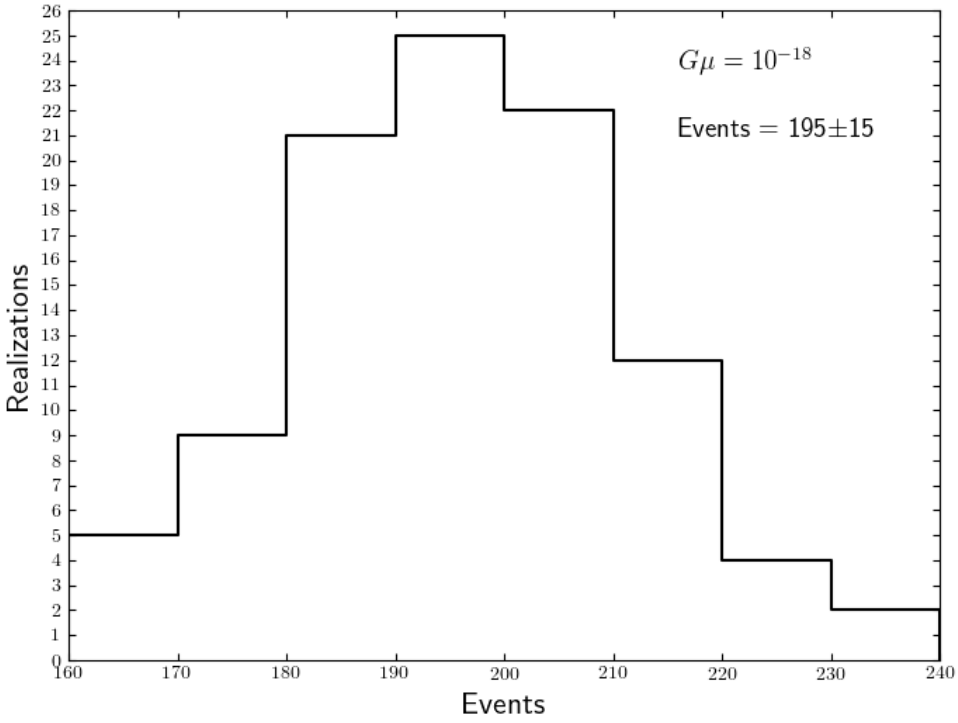

Figure 3.18: The same histogram as that shown in fig. 3.14 except that the simulation is performed with $G\mu = 10^{-18}$.

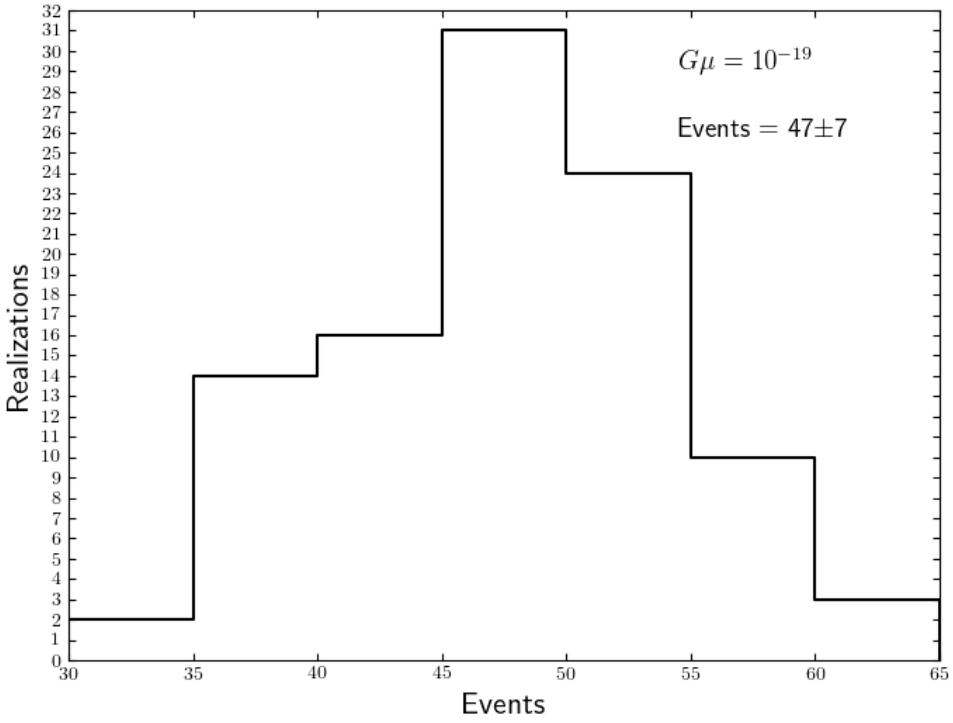

Figure 3.19: The same histogram as that shown in fig. 3.14 except that the simulation is performed with $G\mu = 10^{-19}$.

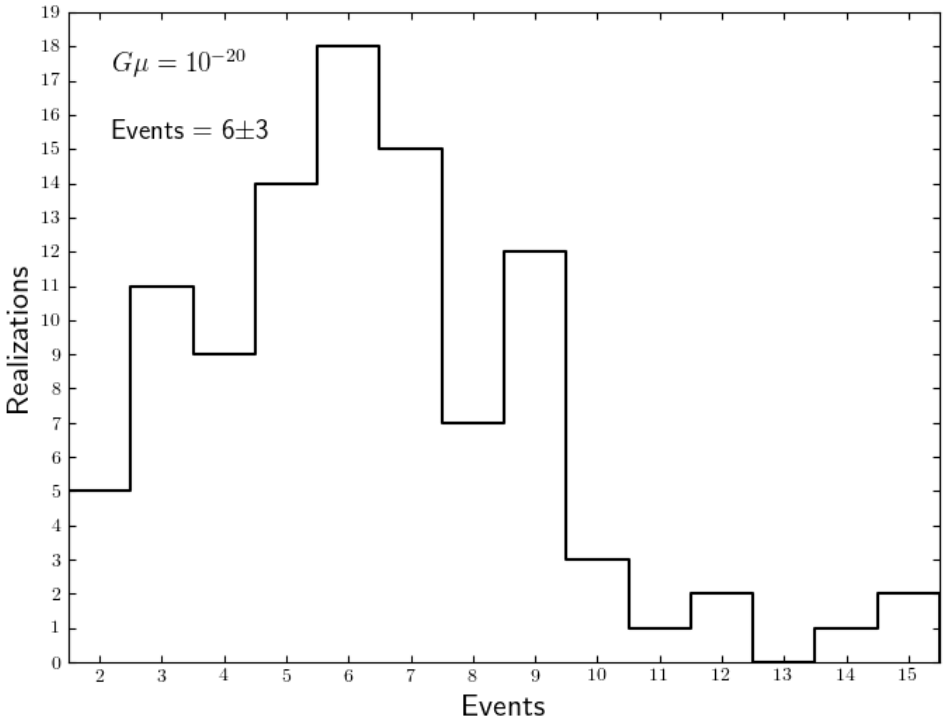

Figure 3.20: The same histogram as that shown in fig. 3.14 except that the simulation is performed with $G\mu = 10^{-20}$.

is to have a very large number of loops in the Galaxy. This increases the likelihood that a loop happens to be present in extreme proximity to the solar system that its harmonic gravitational wave signal overwhelms all sources of noise. From fig. 3.1 we see that this way favors lower string tension, up to a point.

The discussion above tells us that the number of events registered really comes as a result of the tension between the strength of gravitational wave emission of each loop and the total number of loops in the Galaxy. The ideal scenario for event registration would of course be the case when loops with strong gravitational wave emission are present in the Galaxy with high abundance. But fig. 3.1 tells us that we do not have that case, not even in the toy model. In our simulation, for the two sides of the tension described above, the former favors higher string tension whereas the latter favors lower string tension, up to a point. This tension explains the feature observed in numbers of events registered for simulation sets with different string tensions.

At $G\mu = 10^{-12}$, the Galactic confusion is the dominant source of noise, and gravitational wave emission from each loop is the strongest. Thus, despite low abundance of cosmic string loops in the Galaxy in this simulation set, detecting harmonic gravitational wave signal from individual nearby loops is not very difficult because these loops are not required to be located extremely closely to the solar system. They just have to be nearby relative to the rest of the loop population at their frequency in the Galaxy. We therefore register a relatively large number of events at this string tension. The "soloists" in this simulation set get heard by singing very loudly.

As string tension decreases, the strain amplitude of gravitational waves emitted by each loop decreases, and other sources of noise take over. It now becomes impossible to detect harmonic gravitational wave signal from individual nearby loops that are just moderately closer to the solar system relative to the other loops. But on the other hand, the numbers of loops in the Galaxy for cases with these values of the string tension are still far too low

to enable an appreciable number of loops to be located in extreme proximity to the solar system. Thus, very few events are registered in simulation sets with $G\mu = 10^{-14}$ and 10^{-16}.

The number of loops in the Galaxy increases as string tension decreases further, contributing to a higher number of events registered. This reaches a peak for the simulation set with $G\mu = 10^{-18}$, where the number of events registered is very large. Gravitational wave emission by loops with such low string tension is weak, this also means that decay is slow for these loops, and gives rise to the fact that starting from this string tension and below, cosmic string loops emitting gravitational waves with frequencies observable by LISA are not significantly affected by loop decay. The resultant great abundance of cosmic string loops in this simulation set enables many loops to be located extremely closely to the solar system, to the point that their harmonic gravitational wave signal can be directly detected over all sources of noise despite the fact that such signal comes from loops with relatively weak gravitational wave emission. The "soloists" in this simulation set sing quietly, but can be heard by being present very nearby.

The number of events registered drops again as string tension is decreased even further, because enhancement to the number of loops in the Galaxy for cases with even lower string tension starts becoming less significant. The number of loops at a given frequency is, by itself, not dependent on string tension as can be seen from eq. 2.18. Thus, loop abundance in the Galaxy stops increasing as string tension decreases once loop decay ceases being significant for observable loops. We therefore obtain less significant enhancements to the number of loops in the Galaxy at $G\mu = 10^{-19}$ and 10^{-20}, while gravitational wave emission by loops in these simulation sets still becomes weaker with lower string tension. This means that the requirement of proximity to the solar system for harmonic gravitational wave signal from a nearby loop to be detected gets higher, while loops in these simulation sets are not much more likely to be located more closely to the solar system. Thus, we find low numbers of events registered in these simulation sets. More importantly, the number of events registered will

only become even fewer should simulation sets with even lower string tension be performed.

The results discussed in this section tell us that when the rocket effect is not considered, $G\mu \lesssim 10^{-17}$ appears to be the best region in the parameter space for detecting harmonic gravitational wave signal from nearby individual cosmic string loops, while $G\mu \sim 10^{-12}$ also seems to be a viable region.

3.3.6 The Rocket Effect

In section 2.3.2, we discussed the rocket effect which refers to the constant acceleration cosmic string loops in the Galaxy experience as a result of the recoil of their gravitational wave emission. The ultimate effect of this constant acceleration is loop ejection from the Galaxy over time, starting with loops located higher up in the gravitational potential well of the dark matter halo. This is to say that over time, the rocket effect ejects loops in the Galaxy from the outside inwards. This fact enabled us to define in section 2.3.2 the truncation radius $r_{\rm tr}$ given by eq. 2.58.

As loop ejection occurs over time, older loops which have smaller sizes and therefore emitting gravitational waves at higher frequency have smaller truncation radii. We therefore also defined in section 2.3.2 the truncation frequency $f_\odot$ indicating the frequency at which loop ejection has reached the orbit of the solar system in the Galaxy. Also recall from eq. 2.56 that the acceleration due to the rocket effect is stronger if loops have higher string tension due to their correspondingly stronger gravitational wave emission. This translates into lower $f_\odot$ for simulation sets with higher string tension.

As the rocket effect ejects all loops in the Galaxy beyond the truncation radius. Our expectation for its effects on simulation results is quite simple, that is, no event registration should be possible whatsoever when $f > f_\odot$. We expect this because when $f > f_\odot$, $r_{\rm tr}(f) < r_\odot$, and it is just impossible for any cosmic string loop to be located particularly closely to the solar system. The truncation radius imposes a lower bound on the minimum distance to

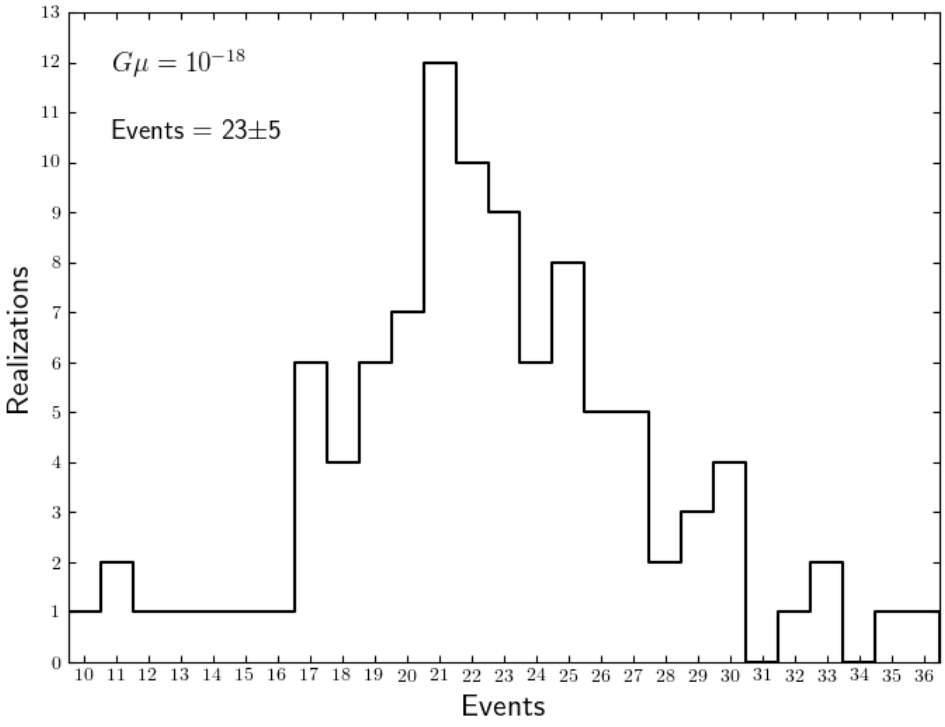

Figure 3.21: Histogram of events satisfying the signal-to-noise requirement eq. 3.39 for the simulation set with the rocket effect at $G\mu = 10^{-18}$, $\alpha = 0.1$.

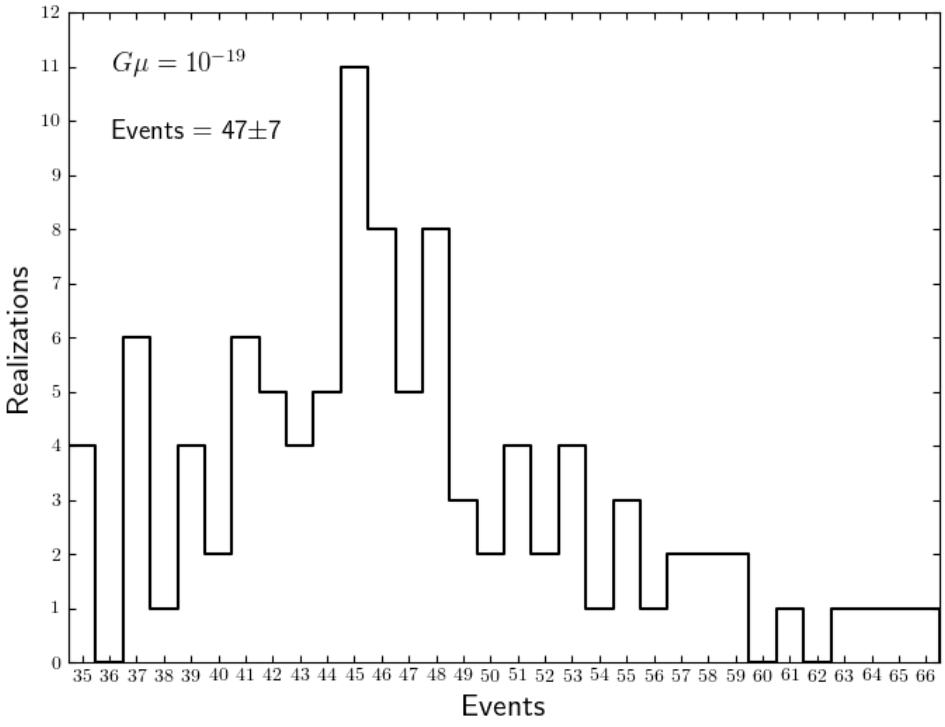

Figure 3.22: The same histogram as that shown in fig. 3.21 except that the simulation is performed with $G\mu = 10^{-19}$.

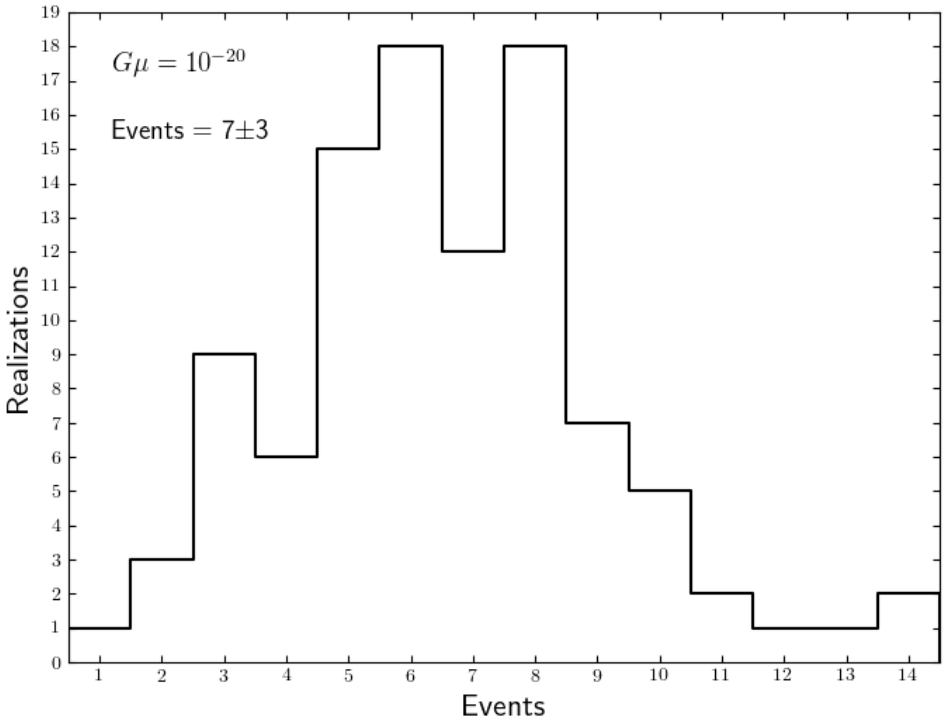

Figure 3.23: The same histogram as that shown in fig. 3.21 except that the simulation is performed with $G\mu = 10^{-20}$.

loops from the solar system. This strict elimination of signal should severely constrain event registration for simulation sets with all but the lowest string tension in the parameter space.

We verify our expectation described above by analyzing results of simulation sets with the rocket effect, again at $\alpha = 0.1$ so that they can be compared with results from the previous section shown in figs. 3.14 through 3.20, with string tension again varying from 10^{-12} to 10^{-20}. We present results which register statistically significant numbers of events in figs. 3.21 through 3.23. Again, a summary of results including those already presented can be found in table 3.2.

In accordance with our expectation, all events are completely eliminated by the rocket effect for the simulation set with $G\mu = 10^{-12}$. This is especially significant when compared with the simulation set with the same string tension but without the rocket effect, which does register a relatively large number of events. The reason is that with string tension this high, $f > f_{\odot} \forall f$ in the frequency range. All loops in the Galaxy are bound by the truncation radius, and none of them is permitted to be located very closely to the solar system. There simply are not any loops around.

For simulation sets with lower string tension, the truncation frequency increases, and the impact of the rocket effect on event registration diminishes, as larger portions of the frequency range become capable of registering events. We therefore start recovering significant numbers of events registered for simulation sets with $G\mu \lesssim 10^{-18}$.

Recall from section 2.3.2, that the truncation frequency more or less tracks the beginning of the decay regime, because both the rocket effect and loop decay have similar dependence on the age of loops, and because the solar system just happens to have such an interesting orbital radius in the Galaxy. Thus, just as is the case for loop decay, rocket effect also starts becoming irrelevant for $G\mu \lesssim 10^{-19}$, with $f < f_{\odot}$ covering most if not all of the frequency range. For this reason, simulation sets with $G\mu \lesssim 10^{-19}$ register similar numbers of events with and without the rocket effect. The fact that in the case of $G\mu = 10^{-20}$, the simulation

set with the rocket effect even registers slightly more events may be attributed to the fact that when $r_{\rm tr} \gtrsim r_{\odot}$, the rocket effect is actually beneficial to event registration, because it largely removes the Galactic confusion coming from the side facing the outside of the Galaxy as illustrated by the upper panel of fig. 2.6, while the probability of individual loops being located in extreme proximity to the solar system remains unaffected.

Results presented in this section confirm our expectation that the rocket effect prevents detection of harmonic gravitational wave signal from nearby individual cosmic string loops unless string tension is quite low. It therefore eliminates $G\mu = 10^{-12}$ as a viable region in the parameter space, and the sweetspot for signal detection in LISA frequency range is therefore $G\mu \lesssim 10^{-18}$. This is the region of the parameter space where our attention should be focused on for physical results.

3.3.7 Initial Loop Sizes

On the surface, the cosmic string loop formation number density of the one-scale model eq. 2.18 appears to suggest that if the one-scale model is set with a smaller initial loop size α, the number density should increase. This is true for loops with a given formation time $t_{\rm c}$. However, for this study, the observation frequency range is fixed, and therefore simulation sets performed with a smaller α include loops that are created later in time. These loops are in fact created with a lower number density because the Hubble volume at their time of formation $H\left(t_{\rm c}\right)^{-3}$ is larger. This fact is reflected in the numbers of loops in the Galaxy for simulation sets without the rocket effect performed with various string tensions and $\alpha = 10^{-5}$ shown in fig. 3.24. Compared with the same quantities for simulation sets performed with $\alpha = 0.1$ shown in fig. 3.1, we see that the numbers in the former figure are consistently lower than those in the latter figure by about two orders of magnitude. We again exclude the rocket effect in our analysis in this section to eliminate complications from effects not pertinent to the issue discussed presently.

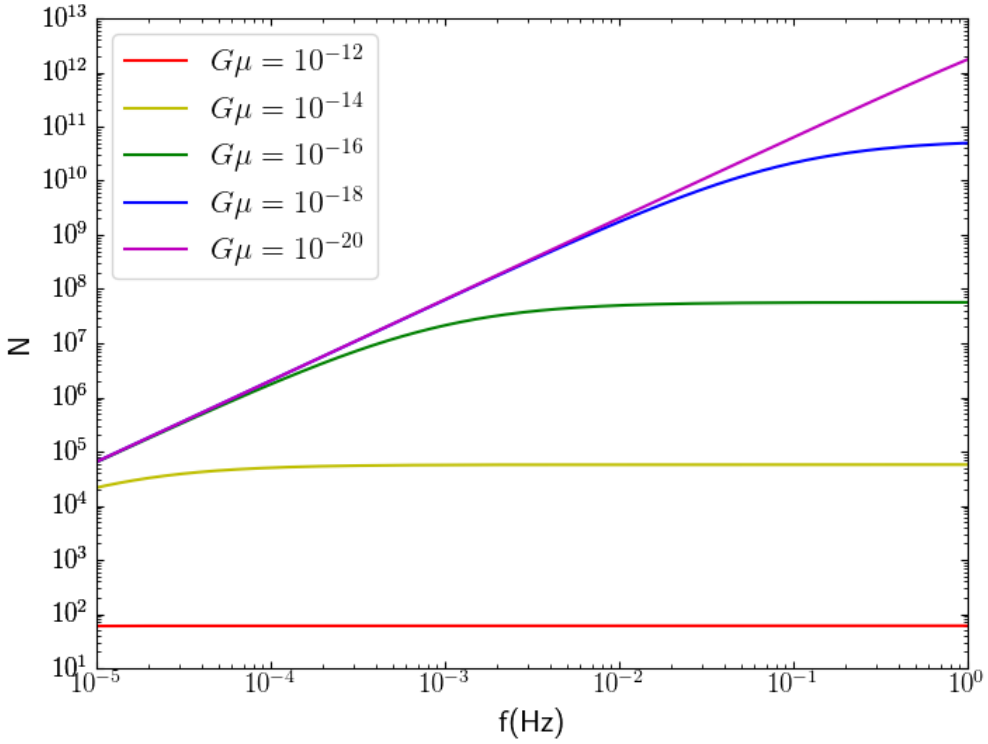

Figure 3.24: The same as fig. 3.1 except that cosmic string loops are created following the one-scale model with $\alpha = 10^{-5}$.

Another feature to note when comparing figs. 3.24 and 3.1 is the fact that decay regimes remain the same for both values of α. This is because the decay regime is really determined by the relative values of αt_c and $\Gamma G\mu\,(t - t_c)$, where we used eq. 2.47. Recall from sections 2.3.2 and 3.3.6, the first quantity is independent of α. For the second quantity, even though overall loops in simulations sets with $\alpha = 10^{-5}$ are younger relative to those in simulation sets with $\alpha = 0.1$, the difference in formation times is completely negligible when compared to the current age of the universe. Thus, loops with both values of α are at similar stages of decay. Also, we mentioned in section 3.3.6 that the rocket effect has its truncation frequency at about the same frequency where the decay regime begins, due to a combination of the nature of the rocket effect and the rather interesting orbital radius of the solar system in the Galaxy. This remains true for $\alpha = 10^{-5}$, because even though the truncation radius

eq. 2.58 seems to be dependent on α, the combination αt_c does not with a fixed frequency range and therefore loop sizes, as we mentioned in section 2.3.2. Thus, both loop decay and the rocket effect work the same way in simulation sets performed with different values of α. The primary difference between simulation sets performed with different values of α for our purpose of detecting harmonic gravitational waves from individual nearby loops therefore manifests in the different numbers of loops in the Galaxy.

As changing α essentially changes the number of loops in the Galaxy for our purpose, we now ask the question, for a given frequency bin, how does changing the number of loops in the Galaxy affect the probability that a loop is located sufficiently closely to the solar system for its harmonic gravitational wave signal to be directly detected, assuming that we are still in the regime where this probability is low so that the possibility of multiple events in the same bin can be neglected? A detailed full answer to this question is likely to be quite complicated, and is not essential to our study. Heuristically, there are three scenarios to be analyzed depending on the relative dominance of the Galactic confusion among all sources of noise.

The first scenario applies to when other sources of noise strongly dominate over the Galactic confusion. In this case, detections of harmonic gravitational waves from nearby individual loops are very low probabilistic events, and any contribution is essentially due to the shell of closest cosmic string loops around the solar system. The number of loops in this shell is proportional to $N^{\frac{2}{3}}$. The probability of event registration for a frequency bin should be proportional to the mean scattering of the distribution of distances to these closest loops in the shell, and this scattering in the distribution of distances is a random walk and therefore its mean should be proportional to $\sqrt{N^{\frac{2}{3}}} = N^{\frac{1}{3}}$. As the overall noise level is strongly dominated by sources of noise other than the Galactic confusion, it remains fixed as N varies. We therefore need to take into account the contribution from geometry. Then the probability of event registration for a frequency bin should also be inversely proportional to

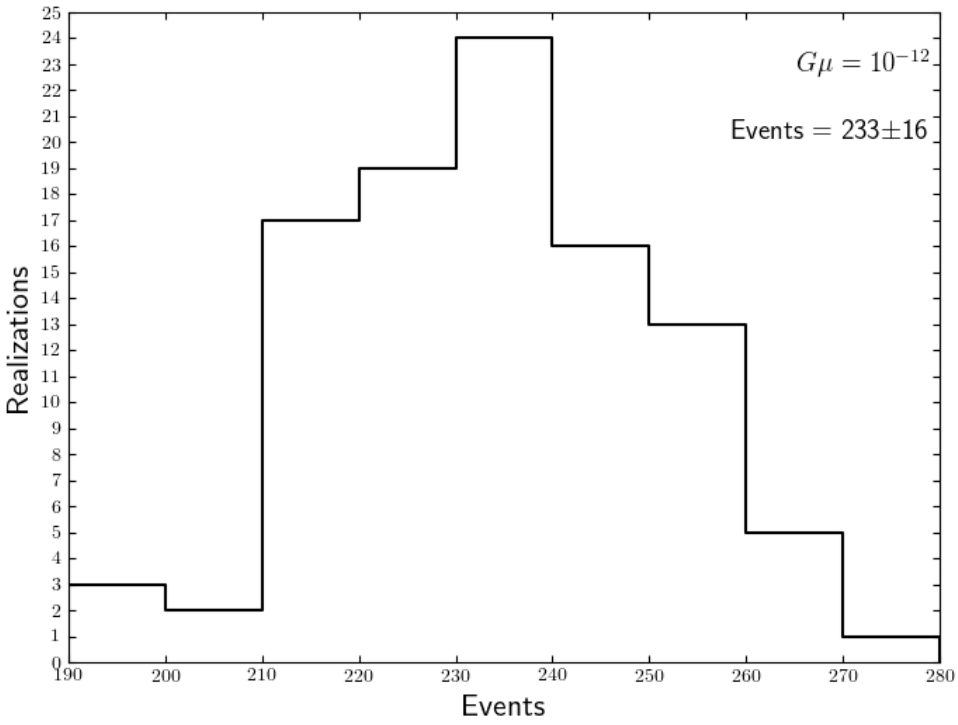

Figure 3.25: Histogram of events satisfying the signal-to-noise requirement eq. 3.39 for the simulation set without the rocket effect at $G\mu = 10^{-12}$, $\alpha = 10^{-5}$.

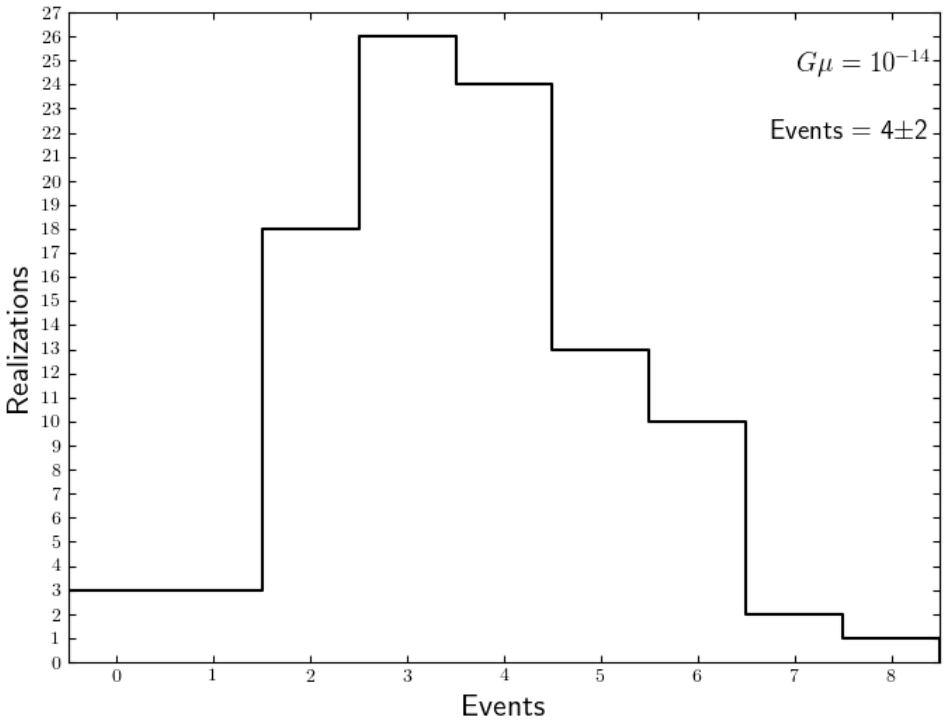

Figure 3.26: The same histogram as that shown in fig. 3.25 except that the simulation is performed with $G\mu = 10^{-14}$.

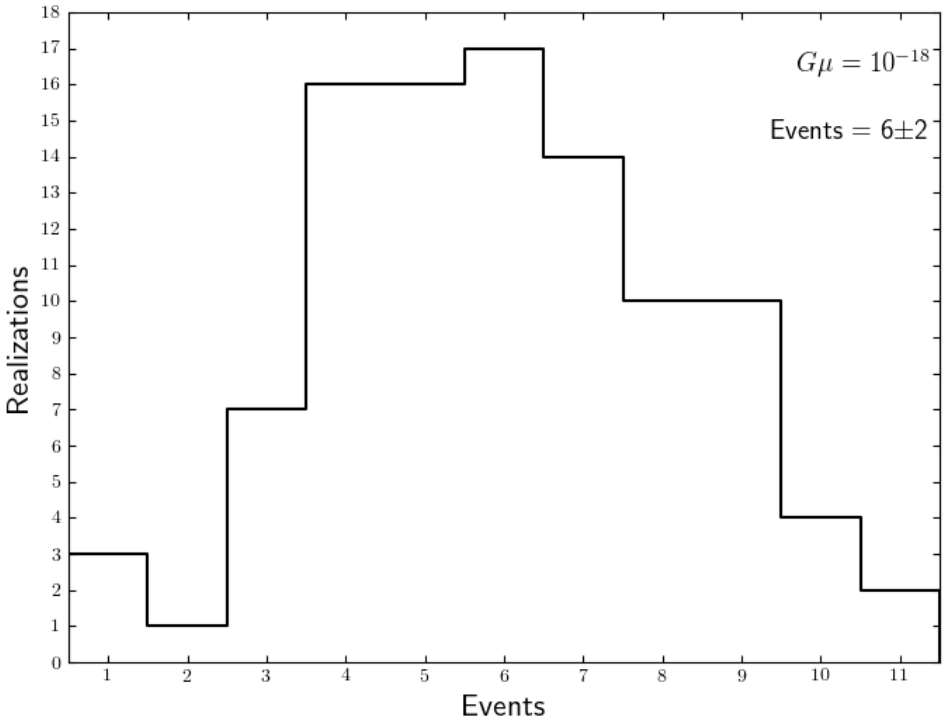

Figure 3.27: The same histogram as that shown in fig. 3.25 except that the simulation is performed with $G\mu = 10^{-18}$.

the average distance to this shell of closest loops, i.e.

$$p_{\rm det} \propto \frac{s_{\rm shell}}{d_{\rm shell}} \propto \frac{N^{\frac{1}{3}}}{N^{-\frac{1}{3}}} = N^{\frac{2}{3}}. \tag{3.48}$$

The second scenario applies to when other sources of noise only weakly dominate over or are somewhat comparable to the Galactic confusion. It is now easier for the nearby distribution of loops to be detected, and therefore instead of a shell, detections are due to contribution from a nearby volume of loops. Thus, the scattering in the distribution of distances to these loops now just scales as $\sqrt{N}$. The contribution of geometry remains the same as that in the first scenario. The scaling of the probability of event registration for a frequency bin therefore becomes

$$p_{\rm det} \propto \frac{s_{\rm vol}}{d_{\rm vol}} \propto \frac{N^{\frac{1}{2}}}{N^{-\frac{1}{3}}} = N^{\frac{5}{6}}. \tag{3.49}$$

The third scenario applies to when the Galactic confusion is the dominant source of noise. In this case, detections are relatively easy as a loop only has to stand out relative to the other loops in the Galaxy to be detected. Thus, detections are still due to contribution from a nearby volume of loops, with a scaling of $\sqrt{N}$. Unlike the other two scenarios described above however, the overall noise level now changes with N. Combining eqs. 3.23 and 3.24, we see that the noise level also scales as $\sqrt{N}$ modulated by geometry. We therefore disregard geometry, and see that we do not expect the probability of event registration for a frequency bin to depend strongly on the number of loops in the Galaxy when noise is dominated by the Galactic confusion.

We analyze the effects of changing α in the one-scale model of the simulation by computing statistical results of event registration for simulation sets without the rocket effect and with $\alpha = 10^{-5}$. Results for simulation sets with statistically significant numbers of events registered are presented in figs. 3.25 through 3.27. These should be compared with figs. 3.14

through 3.20. Again, a summary of all results of event registration presented in this chapter can be found in table 3.2.

When string tension is high, simulation sets with $\alpha = 10^{-5}$ register more events than those with $\alpha = 0.1$, by a factor of ~ 3. In simulation sets with these values of string tension, gravitational wave emission from each loop is strong, and the Galactic confusion dominates the noise. The heuristic argument given above indicates that in this case, there should not be large differences in numbers of events registered between simulation sets with different values of α. These results are consistent with the heuristic argument given that the numbers of loops in the Galaxy with these two values of α differ by about two orders of magnitude, while the corresponding numbers of events only differ by a factor of ~ 3. Moreover, simulation sets with $\alpha = 10^{-5}$ and high string tension contain relatively few loops in the Galaxy, with only $N \sim \mathcal{O}(60)$ at each frequency when $G\mu = 10^{-12}$. Also, keep in mind from the discussion in section 3.1.3 that even this N is already overestimated. With so few loops distributed in the Galaxy, the Galactic confusion itself becomes somewhat less well-defined. In this scenario, conceivably it is relatively easy for harmonic gravitational waves emitted by an individual loop to become detectable just by virtue of this loop being located just somewhat more closely to the solar system relative to the other loops in the Galaxy, without actually being very close. Thus, for simulation sets with high string tension where loop abundance in the Galaxy is low, decreasing α and therefore numbers of loops in the Galaxy may generate some minor enhancement in numbers of events registered.

Just as with results of simulation sets with $\alpha = 0.1$ from section 3.3.5, the number of events registered in simulation sets with $\alpha = 10^{-5}$ first drops as string tension decreases, because gravitational wave emission from each loop becomes weaker, and other sources of noise start becoming dominant. It then stages a rebound as string tension decreases further, due to the enhancement to detection probability for each frequency bin caused by the great abundance of loops in the Galaxy. However, in the case of $\alpha = 10^{-5}$, the rebound in the

number of events for simulation sets with low string tension is far less significant compared to that in the case of $\alpha = 0.1$. This comes as a direct result of the lower numbers of loops in the Galaxy for the former. Thus, for simulation sets with $\alpha = 10^{-5}$, the only potentially viable region in the parameter space is $G\mu \sim 10^{-12}$. We can already sense that when coupled with the rocket effect, this result will make having smaller initial loop sizes disadvantageous for our purpose of detecting harmonic gravitational wave signal from individual cosmic string loops, as we will see in section 3.3.8.

3.3.8 Summary

	$\alpha = 0.1$		$\alpha = 10^{-5}$	
$-\log(G\mu)$	R	NR	R	NR
12	0	71 ± 8	0*	233 ± 16
14	0	1 ± 1	0	4 ± 2
16	0	2 ± 1	0	0*
17	0*	50 ± 7	-	-
18	23 ± 5	195 ± 15	0*	6 ± 2
19	47 ± 7	47 ± 7	-	-
20	7 ± 3	6 ± 3	0*	0*

Table 3.2: Numbers of events satisfying the signal-to-noise requirement eq. 3.39 for all 24 simulation sets of the toy model at a frequency resolution corresponding to $T_{\rm obs} = 1$ month covering the parameter space. Columns R contain results for simulation sets with the rocket effect, and NR for those without. An event number of 0* indicates that not all realizations in the simulation set register 0 events, but the total statistical result for the simulation set remains consistent with 0.

We summarize in table 3.2 numbers of events satisfying the signal-to-noise requirement eq. 3.39 for all 24 simulation sets of the toy model covering the parameter space. Recall from section 3.1.4, due to limitations on computing resources, these simulations sets are performed at a frequency resolution corresponding to $T_{\rm obs} = 1$ month, while noises other than the Galactic confusion are all configured for a mission duration of $T_{\rm obs} = 1$ year. As we discussed at the beginning of this chapter, the objective we would like to achieve with our toy models is twofold. First, the toy models are well-behaved as the number of

cosmic string loops in the Galaxy in the toy models is well-defined for all frequency bins, even those in the decay regime. The exact meaning of this statement will become clear in section 4.2.2. This provides a suitable platform upon which the framework of our simulation can be developed, along with the various necessary methodologies. Second, the toy models physically represent a hypothetical Galaxy with a great overabundance of cosmic string loops, by orders of magnitude for most frequency bins. Results obtained from simulation sets of the toy models can provide guidance on potentially interesting regions of the parameter space where computational efforts should be focused on for predicting physical results of our Galaxy. Additionally, these results can in fact be renormalized to provide insight on the expectation we should have for physical results, as we will discuss in section 3.3.9.

We discussed in section 3.3.7 that with an initial loop size $\alpha = 10^{-5}$ for the one-scale model, the rebound in numbers of events registered in simulation sets without the rocket effect and with low string tension is not significant, due to insufficient loop abundance in the Galaxy. This is disadvantageous for our purpose of detecting harmonic gravitational wave signal from individual loops because the rocket effect is less significant in simulation sets with lower string tension, implying that all simulation sets with $\alpha = 10^{-5}$ may not be able to register many events. This expectation is confirmed by results shown in table 3.2, where rather dramatically, the large number of events registered in the simulation set without the rocket effect and with $G\mu = 10^{-12}$ are basically wiped out when the rocket effect is incorporated. The total result is simply that no significant numbers of events can be registered for all simulation sets with $\alpha = 10^{-5}$.

Recall from section 2.3.1 that clumping of cosmic string loops in the Galaxy is reduced when α is small, because these loops are younger and therefore have had less time for velocity damping. In our simulation, perfect clumping of loops in the Galaxy is always assumed, meaning that loop abundance in the Galaxy in simulation sets with $\alpha = 10^{-5}$ has been somewhat overestimated. This implies that results for simulation sets with $\alpha = 10^{-5}$ are

already overestimations, making event registration in these simulation sets even less likely than what our results already suggest.

Unlike the simple one-scale model of loop formation which has the normalization factor of loop number density scaling as α^{-1} as can be seen from eq. 2.18, results from the most state-of-the-art loop formation simulation[3] effectively produce a steeper scaling of the normalization factor as $\alpha^{-\frac{3}{2}}$, meaning that smaller loops are more abundant in that model. Coupled with discussions above, this means that in the LISA frequency range, the number of loops in the Galaxy with that model stays approximately the same at about the level with $\alpha = 10^{-5}$ in our model, as α decreases until the cutoff at the gravitational backreaction scale $\alpha \sim \Gamma G\mu$. Thus, we see that still, no significant number of events can be registered with the loop formation model from the most state-of-the-art loop formation simulation, despite the increased abundance of smaller loops. This is even without considering the fact that clumping of loops in the Galaxy is greatly reduced for small loops.

We discussed in section 2.1.2 that while our selection of initial loop sizes correspond to characteristic initial loop sizes from the big-loop paradigm, there exists also a small-loop paradigm, with a great overabundance of tiny loops with initial loop sizes below the gravitational backreaction scale $\alpha \lesssim 20(G\mu)^{1+2\chi}$. These are extremely small loops given how low string tension has been constrained. In this model, instead of being cutoff by gravitational backreaction, production of very small loops below that scale continues, and the normalization factor of loop number density effectively levels off[50]. This however, still means a reduction in the number of loops in the Galaxy emitting gravitational waves in the LISA frequency range. Coupled with the fact that such tiny loops do not clump well at all in the Galaxy, we see that event registration is not possible with these tiny loops from the small-loop paradigm.

Our attention should be focused on the parameter space with big loops, $\alpha = 0.1$, where the hope of detection rests upon. We discussed in section 3.3.6 that in this region of the

parameter space, significant numbers of events are registered in simulation sets with low string tension. Loops in simulation sets in this region of the parameter space mostly do not suffer from loop decay and the rocket effect. The viable region of the parameter space for LISA detection of harmonic gravitational wave signal from individual loops is therefore $G\mu \lesssim 10^{-18}$ and $\alpha = 0.1$.

One more thing to note is that despite the fact that the 24 simulation sets of the toy model whose results are shown in table 3.2 are performed at a frequency resolution corresponding to $T_{\rm obs} = 1$ month, the guidance they provide on the interesting region of the parameter space for further analysis should be applicable to our eventual goal of predicting detections for a LISA mission duration of $T_{\rm obs} = 1$ year.

To see the point described above, we first note that in the limit when the probability for a frequency bin to register an event is low, which we established previously is always the case in our simulation, even in the toy models, directly increasing the frequency resolution without rebinning loop abundance just increases the number of events registered correspondingly. This fact is verified by the result shown in fig. 3.28 from the simulation set with the rocket effect at $G\mu = 10^{-18}$, $\alpha = 0.1$, in the alternative toy model performed with a frequency resolution corresponding to $T_{\rm obs} = 1$ year as we described in section 3.1.4. The number of events registered in this simulation set

$$E_{\rm D,1y} = 283 \pm 15 \tag{3.50}$$

is computed without incorporating higher harmonics, and should therefore be compared with eq. 3.40. Clearly, the difference is consistent with a factor of 12.

Recall from the description of the toy models at the beginning of this chapter, rebinning the number of loops in the Galaxy for each frequency bin from the toy models into the physical model results in reductions by orders of magnitude as shown in eq. 3.54, especially at higher frequency where LISA instrumental noise and the WD binaries background are

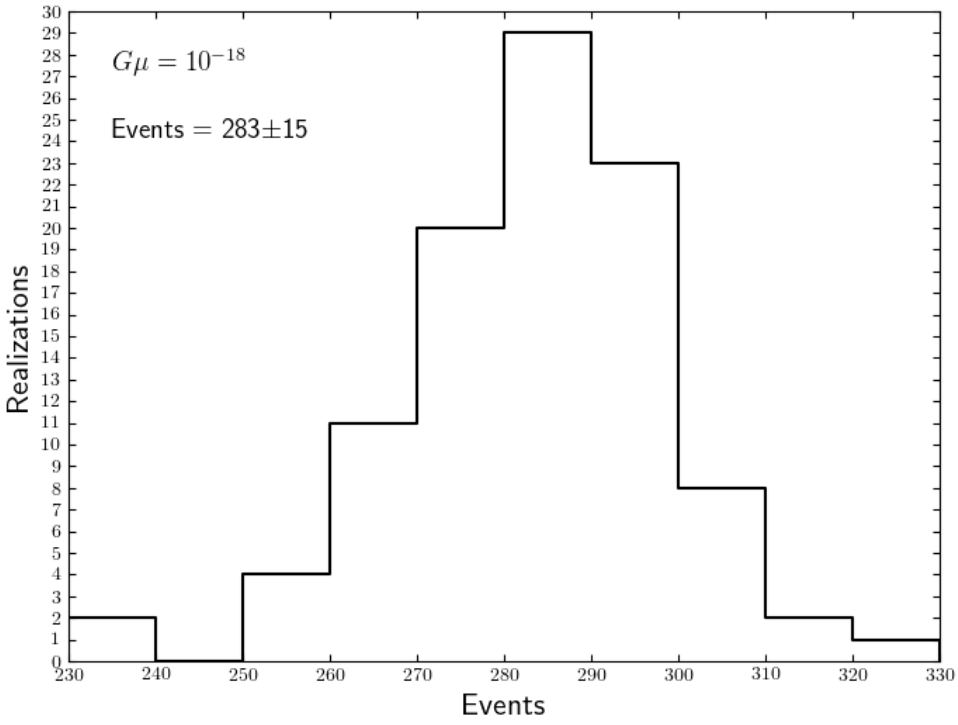

Figure 3.28: Histogram of events satisfying the signal-to-noise requirement eq. 3.39 for the simulation set with the rocket effect at $G\mu = 10^{-18}$, $\alpha = 0.1$ in the alternative toy model performed with a frequency resolution corresponding to $T_{\rm obs} = 1$ year.

lower and hence where most events are registered. From the discussion in section 3.3.7, for simulation sets in the interesting region of the parameter space, the corresponding reduction in the probability of event registration for a frequency bin should be by a significant power-law of that factor which can be up to $\sim 10^{-7}$. This reduction more than offsets the enhancement discussed earlier, and therefore results from the 24 simulation sets in the toy model performed at a frequency resolution corresponding to $T_{\rm obs} = 1$ month are already overestimations even for physical simulation sets performed with a mission duration of $T_{\rm obs} = 1$ year. This point will be elaborated further in section 3.3.9.

3.3.9 Implication on Physical Results

We discussed at the beginning of this chapter as well as in section 3.3.8 that even though on the surface, our toy models represent hypothetical versions of the Galaxy containing a great overabundance of cosmic string loops, results obtained from these models not only can provide guidance on the interesting region of the parameter space for further analysis, but can also provide direct insight into the expectation that we should have for simulation sets with the physical model of the Galaxy. In fact, we have already outlined the basics for renormalizing results obtained from simulation sets with the toy models into those for the physical Galaxy at the end of section 3.3.8. In this section, we offer a concrete description of the renormalization procedure, and perform the procedure for simulation sets in the interesting region of the parameter space, thereby obtaining insights into the expected physical results for the Galaxy.

Recall from section 2.1.1 that the formation number density of cosmic string loops eq. 2.18 is naturally binned in log-scale of loop formation time, because the total length of loops created at any given time is a scaling solution of the horizon size. This means that loops created at later times should be binned in correspondingly larger formation time bins to maintain the simple normalization of the scaling solution. In particular, eq. 2.18 is

normalized with $\Delta t_{\rm c} = 0.1 t_{\rm c}$. The binning in formation time translates into a binning in frequency of gravitational wave emission by the loops when we rewrite the number density as a function of frequency in section 2.2.3. We differentiate with respect to loop formation time to calculate the binning in frequency

$$\left|\frac{d\ln f}{dt_{\rm c}}\right| = \left|\frac{d\ln l}{dt_{\rm c}}\right| = \frac{1}{l}\frac{dl}{dt_{\rm c}} = \frac{\alpha + \Gamma G\mu}{l} \simeq \frac{\alpha}{l} \simeq \frac{\alpha}{\alpha t_{\rm c} - \Gamma G\mu\,(t - t_{\rm c})}, \tag{3.51}$$

where we used eqs. 2.30 and 2.47, and the fact that $\alpha \gg \Gamma G\mu$ for loops created following the big-loop paradigm. When loop decay is not significant, meaning that the frequency range of observation is outside of the decay regime,

$$\alpha t_{\rm c} \gg \Gamma G\mu\,(t - t_{\rm c})\,, \tag{3.52}$$

and eq. 3.51 simplifies to the expected relation

$$\frac{\Delta f}{f} \simeq \frac{\Delta t_{\rm c}}{t_{\rm c}} = 0.1. \tag{3.53}$$

This is the binning of loop number density as a function of frequency of gravitational wave emission by the loops. We see that in the decay regime where the condition eq. 3.52 is not satisfied, natural frequency bins are no longer regular log bins. In fact, when loop decay is significant, natural frequency bins can become enormous according to eq. 3.51, meaning that the already reduced population of loops in the Galaxy of the decay regime actually emits gravitational waves spanning a wide range of frequencies. Also note that the frequency in derivations above always refers to the fundamental frequency, as higher harmonics are incorporated later through postprocessing, as described in section 3.3.2. Recall from discussions in sections 3.3.7 and 3.3.8, the relation eq. 3.53 is largely applicable to all simulation sets in the interesting region of the parameter space $G\mu \lesssim 10^{-18}$, $\alpha = 0.1$. We

focus our attention on this region of the parameter space in all later derivations for the rest of this section.

The total numbers of events registered in simulation sets in the toy models are summations of events registered in all frequency bins. Recall from discussions in sections 3.1.3 and 3.3.7, a given frequency bin i can register either no event or one event with some small probability p_i. This means that the total number of events registered for a simulation set can therefore be interpreted as the summation of outcome values of a collection of Bernoulli trials (random trials with two possible outcomes, such as flipping a coin) with probabilities p_i for outcome value 1 and $1 - p_i$ for outcome value 0.

Recall that the toy models are configured by taking the loop number density eq. 2.18 and directly evaluating this expression at frequency resolutions $\Delta f_{\text{obs}} = \frac{1}{T_{\text{obs}}}$, the loop number density in a frequency bin f in the toy models therefore corresponds to that in the much larger frequency bin with size $\Delta f = 0.1f$ in the physical model. Thus, rebinning the number of loops in the Galaxy as a function of frequency from the toy models into the physical model reduces the number of loops in the frequency bin f by a bin reduction factor

$$\eta(f) = \frac{\Delta f_{\text{obs}}}{\Delta f} = \frac{\frac{1}{T_{\text{obs}}}}{0.1f} = \frac{10}{T_{\text{obs}} f} \ll 1. \tag{3.54}$$

The actual probability of event registration for a frequency bin in simulation sets in the toy models p_i is unknown. However, from eqs. 3.48 and 3.49, we know that p_i is roughly reduced by a power-law of loop abundance which can be represented by a factor $\eta(f)^\kappa$ after rebinning for simulation sets in the interesting region of the parameter space, when the Galactic confusion is not the most dominant source of noise. The scaling parameter $\kappa = \frac{2}{3}$ when other sources of noise strongly dominate over the Galactic confusion, and $\kappa = \frac{5}{6}$ when they only dominate weakly. From results of simulation sets without the rocket effect and with $G\mu = 10^{-18}$ from table 3.2 for both values α, we see that the simulation set with smaller initial loop sizes has registered a lower total number of events by a factor of ~ 33

compared to that with larger initial loop sizes. Recall that the difference in numbers of loops in the Galaxy is by about two orders of magnitude, we see that the actual simulation sets in fact contain a mixture of scenarios corresponding to the two values of κ. As we discussed in section 3.3.8, the Galactic confusion is not the dominant source of noise for simulation sets in the interesting region of the parameter space. We therefore compute predictions for physical detection probabilities for the two scenarios when other sources of noise are dominant, and the results should be estimates on bounds of physical detection probabilities.

Recall that in simulation sets in the toy models, event registration in the frequency bins is represented by Bernoulli trials with probabilities p_i and outcome values 1 and 0, and that a set of n Bernoulli trials follows the binomial distribution with the expectation value np. Adopting a frequentist interpretation, we can therefore effectively account for this rebinning from the toy models into the physical model without knowing p_i by changing the success outcome value for frequency bin f from 1 to $\eta(f)^\kappa$, effectively altering n. Then the total number of detections in a simulation set in the physical model predicted by rebinning the corresponding simulation set in the toy models is

$$N_{\mathrm{P}} \sim \sum_i \eta\left(f_i\right)^\kappa = \langle \eta(f)^\kappa \rangle N_{\mathrm{T}}, \tag{3.55}$$

where the sum is over all events registered in the simulation set in the toy models. The more straightforward but less rigorous way of interpreting eq. 3.55 is to think of $\eta\left(f_i\right)^\kappa$ as effective detection numbers for frequency bins in simulation sets in the physical model.

Recall from discussions and results in previous sections of this chapter, such as the result presented in fig. 3.7, most events registered in simulation sets in the toy models are at higher frequencies due to a combination of enhanced loop abundance in the Galaxy and reduced LISA instrumental noise and the Galactic WD binaries background. Thus, the bin reduction factors in the sum eq. 3.55, $\eta\left(f_i\right)$, are very small, and the corresponding total detection number for the simulation set in the physical model is less than unity. It is therefore

more suitable to interpret the total detection number for the simulation set in the physical model, $N_{\rm P}$, as the total detection probability for the whole simulation set, defined as the probability that at least one detection is made in the entire observed frequency range of the simulation set over the course of the mission. The more proper way of estimating the detection probability is

$$p_{\rm det} \sim 1 - \prod_i \left(1 - \eta \left(f_i\right)^\kappa\right), \tag{3.56}$$

where the index of the product i is over all frequency bins which register an event in the simulation set in the toy models.

This interpretation with $\eta \left(f_i\right)^\kappa$ in eq. 3.56 is well-defined in the limit $\eta \left(f_i\right)^\kappa \ll 1$ to the point that $N_{\rm P}$ is less than unity, because

$$p_{\rm det} \sim 1 - \prod_i \left(1 - \eta \left(f_i\right)^\kappa\right) \approx \sum_i \eta \left(f_i\right)^\kappa \sim N_{\rm P} \tag{3.57}$$

when we expand eq. 3.56 and only keep terms up to linear order in $\eta \left(f_i\right)^\kappa$. We should also clarify that in writing down eq. 3.56, we are not taking $\eta \left(f_i\right)^\kappa$ to be the detection probability for the frequency bin. If the actual physical detection probability for each frequency bin, $p_{{\rm p},k}$, were known, then the expression for the total detection probability of the simulation set would be

$$p_{\rm det} = 1 - \prod_{k \in \text{all bins}} \left(1 - p_{{\rm p},k}\right), \tag{3.58}$$

where the index k is over all frequency bins. Clearly, $\eta \left(f_i\right)^\kappa \gg p_{{\rm p},k}$, as otherwise

$$N_{\rm P} = \sum_{k \in \text{all bins}} p_{{\rm p},k} \gg 1 \tag{3.59}$$

from eq. 3.54, and the condition for eq. 3.56 is not satisfied. In writing eq. 3.56 with $\eta \left(f_i\right)^\kappa$, we are in fact implicitly estimating $p_{{\rm p},k}$ through the overall statistics of event registration in the simulation set in the toy models modulated by $\eta \left(f_i\right)^\kappa$ as a result of rebinning into

the physical model. The more intuitive and less rigorous way of interpreting eq. 3.57 is simply that if the expected detection number for a simulation set in the physical model is less than unity, say 0.1, then we reasonably expect to repeat the simulation set 10 times before a detection is made, i.e. the probability that a detection is made by performing the simulation set once can be said to be 0.1.

The detection probability eq. 3.56 assumes that the $T_{\rm obs}$ used to bin the simulation set in the toy models is the actual LISA mission duration. It is therefore only applicable to the single simulation set in the alternative toy model with the rocket effect and with $G\mu = 10^{-18}$, $\alpha = 0.1$, performed at a frequency resolution corresponding to $T_{\rm obs} = 1$ year. Simulation sets whose results are summarized in table 3.2 are performed at a frequency resolution corresponding to $T_{\rm obs} = 1$ month, and therefore some further manipulation is necessary for making predictions on detection probabilities for simulation sets in the physical model with $T_{\rm obs} = 1$ year.

To obtain a correct estimate on physical detection probabilities from these simulation sets in the toy model performed at a lower frequency resolution, we first compute the bin reduction factor $\eta(f)$ with $T_{\rm obs} = 1$ year. This produces the correct reduction factors for the physical model. The problem now is just a lack of the number of frequency bins, i.e. a lack of the number of Bernoulli trials. The solution is then to effectively duplicate each frequency bin 12 times in eq. 3.56. This procedure produces reasonable estimates of physical detection probabilities, because the number of loops in the Galaxy is a smooth and slowly varying function of frequency, and therefore detection probabilities as well as bin reduction factors in nearby bins do not differ significantly. Then the physical detection probability estimated from simulation sets in the toy model performed at a lower frequency resolution corresponding to $T_{\rm obs} = 1$ month is

$$p_{\rm det} \sim 1 - \prod_j \left(1 - \eta\left(f_j\right)^{\kappa}\right)^{12}, \tag{3.60}$$

where we use a different index j from that in eq. 3.56 to indicate that the product is now over frequency bins with event registration in simulation sets in the toy model at a resolution corresponding to $T_{\rm obs} = 1$ month.

We verify results derived above that predictions can be made for the physical detection probability for a LISA mission duration of $T_{\rm obs} = 1$ year, by directly comparing results from eqs. 3.60 and 3.56. We compute separately values of the predicted physical detection probability for the scenario with $\kappa = \frac{2}{3}$, from simulation sets with $G\mu = 10^{-18}$, $\alpha = 0.1$, one from the simulation set in the toy model performed at a frequency resolution corresponding to $T_{\rm obs} = 1$ month, one from that in the other toy model performed at a frequency resolution corresponding to $T_{\rm obs} = 1$ year. The same as in section 3.3.8, all power of gravitational waves emitted by cosmic string loops is concentrated in the fundamental mode for the latter case. We therefore use the same configuration for the former for consistency. Of course, as we discussed in section 3.3.2, this should not have any significant effects on results.

Histograms of the predicted physical detection probability for both cases are presented in fig. 3.29. We first recall that these two simulation sets which are really from two different toy models as discussed in section 3.1.4, have very different numbers of events registered as can be seen by comparing eqs. 3.40 and 3.50. However, histograms computed from results of these simulation sets using eqs. 3.60 and 3.56 are centered at similar values. In fact, statistically they basically produce the same prediction for the physical detection probability for a LISA mission duration of $T_{\rm obs} = 1$ year

$$p_{\rm det,m} = (10 \pm 2)\%; \tag{3.61}$$

$$p_{\rm det,r} = (10.1 \pm 0.6)\%. \tag{3.62}$$

Thus, we in fact can make predictions for results of simulation sets in the physical model from those of simulation sets in the toy model performed with a different frequency resolution. The result obtained from the simulation set in the toy model with a higher frequency resolution

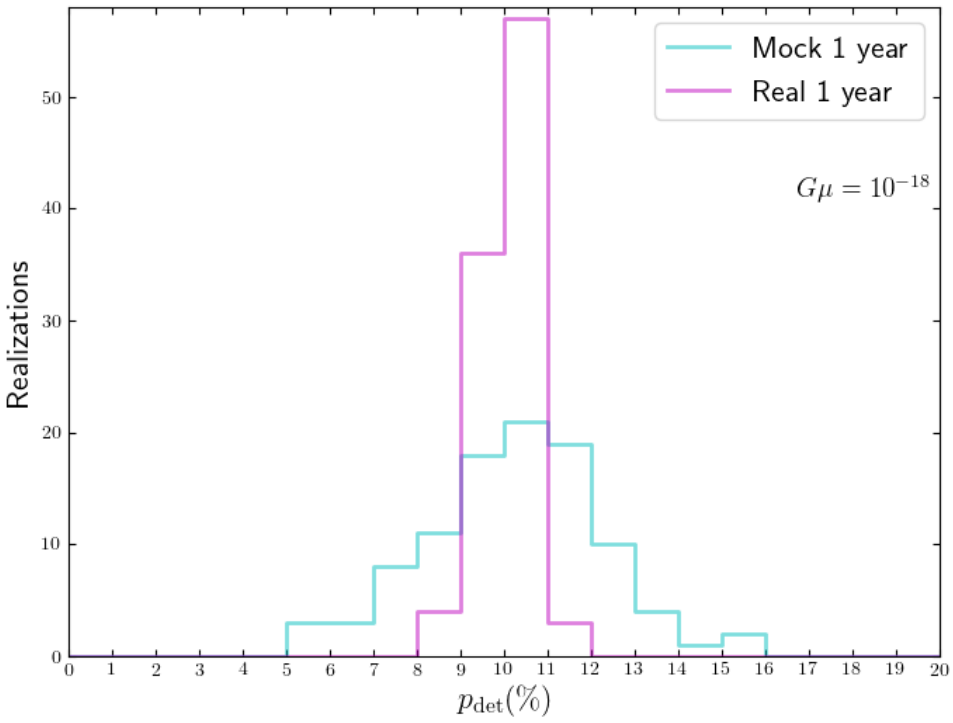

Figure 3.29: Histograms of the predicted physical detection probability for the scenario with $\kappa = \frac{2}{3}$, from simulation sets with $G\mu = 10^{-18}$, $\alpha = 0.1$, for a LISA mission duration of $T_{\rm obs} = 1$ year. The histograms in cyan and magenta are computed using eqs. 3.60 and 3.56 from simulation sets in the toy models performed at frequency resolutions corresponding to $T_{\rm obs} = 1$ month and $T_{\rm obs} = 1$ year, respectively.

simply has better statistics as can be seen from histograms shown in fig. 3.29 and the predicted physical detection probabilities eqs. 3.61 and 3.62. However, as we will discuss below, excellent statistics does not actually provide us with any advantage for this purpose.

Before we start making predictions for the physical detection probabilities, we first need to explain an important point to keep in mind when interpreting predictions made by eq. 3.60. We remarked earlier in this section that the simulation set with the rocket effect with $G\mu = 10^{-18}$, $\alpha = 0.1$ in the toy model actually contains a mixture of both scenarios corresponding to the two values of κ. Gravitational wave emission by loops with this string tension is already sufficiently strong, that at frequencies where the LISA instrumental noise and the Galactic WD binaries background are low, they already do not dominate strongly over the Galactic confusion. On the other hand, renormalizing into the physical model greatly reduces the Galactic confusion because the numbers of loops in the Galaxy are greatly reduced, meaning that simulation sets in the physical model do belong to the scenario corresponding to $\kappa = \frac{2}{3}$. Thus, during the process of renormalization from the toy model into the physical model for this simulation set, the probabilities of event registration for frequency bins where the domination of other sources of noise is initially weak first scale with $\kappa = \frac{5}{6}$, and then transition into $\kappa = \frac{2}{3}$. From eq. 3.60, we see that the former corresponds to a steeper reduction of the probability. Thus, making predictions on the physical detection probability with $\kappa = \frac{5}{6}$ tends to underestimate, while predictions made with $\kappa = \frac{2}{3}$ tend to overestimate. These predictions should therefore be viewed more as lower and upper bounds on the physical detection probability, respectively. We note that simulation sets with lower string tension have lower Galactic confusion, thus we expect the prediction made with $\kappa = \frac{2}{3}$ to be a better estimate of the physical detection probability at the very low end of string tension in the parameter space, $G\mu = 10^{-20}$.

We are now able to make predictions for the probabilities of detecting harmonic gravitational wave signal from individual nearby cosmic string loops for simulation sets in the

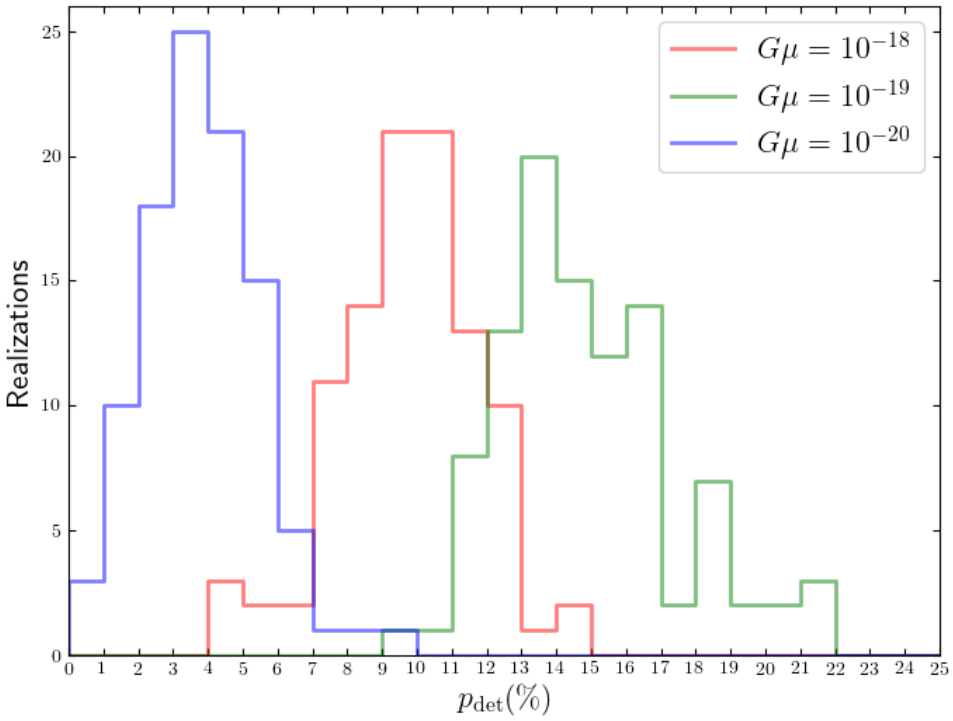

Figure 3.30: Histograms of predicted physical detection probabilities for the scenario with $\kappa = \frac{2}{3}$, from simulation sets with $\alpha = 0.1$ for a LISA mission duration of $T_{\mathrm{obs}} = 1$ year, computed from simulation sets in the toy model performed with a frequency resolution corresponding to $T_{\mathrm{obs}} = 1$ month using eq. 3.60. Histograms in orange, green, and blue are computed from simulation sets with $G\mu = 10^{-18}$, 10^{-19}, and 10^{-20}, respectively.

physical model with a LISA mission duration of $T_{\rm obs} = 1$ year, for the interesting region of the parameter space as discussed in section 3.3.8, $G\mu \lesssim 10^{-18}$, $\alpha = 0.1$. The histograms of the predictions in the scenario corresponding to $\kappa = \frac{2}{3}$ are presented in fig. 3.30. At 3σ level, the predicted bounds of the physical detection probabilities are

$$0\% \lesssim \quad p_{\rm det,18} \quad \lesssim 16\%; \tag{3.63}$$

$$0\% \lesssim \quad p_{\rm det,19} \quad \lesssim 22\%; \tag{3.64}$$

$$0\% \lesssim \quad p_{\rm det,20} \quad \lesssim 9\%, \tag{3.65}$$

where the lower bounds are computed using eq. 3.60 for the scenario corresponding to $\kappa = \frac{5}{6}$, and are all consistent with zero. We expect the result for $G\mu = 10^{-20}$, eq. 3.65 to be a more decent estimate of the actual physical detection probability, while the actual physical detection probabilities for simulation sets with the other values of the string tension are probably far lower than the upper bounds in eqs. 3.63 and 3.64.

Recall from the discussion at the beginning of this chapter, simulation sets in the toy models contain a great overabundance of cosmic string loops in the Galaxy compared to those in the physical model. The process of renormalization described above effectively converts simulation sets in the toy models into simulation sets in the physical model with more realizations. This is the underlying reason that allows us to make statistical predictions on the physical detection probability from simulation sets in the toy models. The statistics of the predictions really comes as a result of sampling of subsets of these effective realizations. However, as we discussed above, the conversion itself is far from accurate, and the predictions can therefore only serve as estimates of the upper and lower bounds of the physical detection probability. Even though the estimates given in eqs. 3.63 through 3.65 do seem rather unpromising, we still need to perform the simulation for the physical Galaxy as part of our quest for real answers.

CHAPTER 4

PHYSICAL RESULTS

4.1 Results for the Physical Model

4.1.1 Simulation Setup

As we discussed at the beginning of chapter 3, the toy models provide us with a well-defined framework which enables the development of the entirety of the methodology of our simulation. The extremely high abundance of cosmic string loops in the Galaxy in the toy models proves to be both a challenge and a blessing for our simulation. High loop abundance in the Galaxy is a challenge because it renders the straightforward method of tracking every single loop in the Galaxy an absolute impossibility. This challenge is overcome by utilizing the closest loops method discussed in section 3.1.3. This method is necessary even in the case of simulating the physical Galaxy, as the physical abundance of cosmic string loops in the Galaxy can still make tracking each individual loop a practice that is beyond current computational capabilities, especially for the potentially interesting region of the parameter space for detecting harmonic gravitational wave signals from nearby individual loops, where loop abundance in the Galaxy is very high and is in fact the reason behind the enhanced likelihood of making detections. The extremely high loop abundance in the Galaxy in the toy models is also a blessing because it enables the registration of many events in simulation sets. Based on these events, we are then able to thoroughly analyze the characteristic behavior of simulating cosmic string loops in the Galaxy for detecting harmonic gravitational wave signals from nearby loops, as we discussed in detail in section 3.3. By analyzing results from simulation sets in the toy models, we are now equipped with the knowledge of the physical reasoning behind our objective, as well as an expectation for results from simulation sets configured for the physical Galaxy. One of the most direct benefits from results from simulation sets in the toy models is the guidance they provide for the potentially interesting

region of the parameter space to focus our attention on, as we discussed in section 3.3.8.

We showed in section 3.3.9 that in going from the toy models to the physical Galaxy, the reduction in the number of loops in a frequency bin can be severe, by up to a factor of $\sim 3 \times 10^{-7}$ for a LISA mission duration of $T_{\rm obs} = 1$ year as can be seen from eq. 3.54. We should note that unlike the case of estimating detection of gravitational wave burst signal from cosmic string loops in the Galaxy where the detection rate simply scales with loop number density in the Galaxy[11], the relationship between detection rate and loop abundance in the Galaxy is not a simple one for our objective of estimating detection of harmonic gravitational wave signals from nearby loops. This is because in the latter case, detection is not due to there existing many distant loops in the Galaxy which just contribute to the Galactic background, but is caused by a loop which by chance happens to be located especially closely to the solar system in relation to distances to other loops in the Galaxy. The detection rate manifests as the result of a complex relationship between the Galactic background and other fixed sources of noise such as the detector instrumental noise. What makes the relationship between the expected detection rates from simulation sets in the toy models and from those of the physical Galaxy even more complex is the fact that the reduction in loop abundance in converting from the former to the latter is frequency dependent. Even though we provided estimates of the expectation for simulation sets of the physical Galaxy in section 3.3.9 based on heuristic arguments eqs. 3.56 and 3.60, and that such estimates in fact indicate that detection of harmonic gravitational wave signal from nearby individual loops is not very promising, we should still apply the simulation machinery to the physical Galaxy, so that we know for sure.

With the obvious exception of loop abundance in the Galaxy, the configuration and methodology for simulation sets for the physical Galaxy are identical to those in the toy models, described in section 3.1.4. We perform simulations with the rocket effect for the interesting region of the parameter space $G\mu \in [10^{-18}, 10^{-19}, 10^{-20}]$, $\alpha = 0.1$, all with

the LISA mission duration $T_{\rm obs} = 1$ year. The same as for simulation sets in the toy models, we perform 100 realizations for each simulation set. The Galactic confusion noise is obtained from the Galactic confusion background using the closest loops method discussed in section 3.1.3 with fitting relations already computed from noise-side simulation sets in the toy models. For all data analysis of results from simulation sets for the physical Galaxy, the total power of gravitational wave emission from cosmic string loops is concentrated in the fundamental mode. We have seen from section 3.3.2 that including higher harmonic modes in the simulation makes essentially no difference to the detection results obtained, and any difference is such that concentrating all power of gravitational wave emission from the loops in the fundamental mode results in a very slight overestimation in the number of detections. We adopt the same requirement on the signal-to-noise ratio eq. 3.39 for a detection as that of results from simulation sets in the toy models.

4.1.2 Results

Given that simulation sets for the physical Galaxy have loop abundance in the Galaxy that is so much lower than that in simulation sets in the toy models as we discussed in section 4.1.1, coupled with the numbers of events registered in the latter summarized in table 3.2, it truly makes one wonder if there can be any detection at all in the former. The answer is that though quite few, there still are detections. An example of such a detection captured by a realization in the simulation set for the physical Galaxy with the rocket effect at $G\mu = 10^{-20}$, $\alpha = 0.1$ is presented in fig. 4.1. We can see that with relatively low loop abundance in the physical Galaxy, the overall Galactic background is simply drowning in the LISA instrumental noise with the Galactic WD binaries background. However, there is a loop which by chance happens to be located extremely closely to the solar system, to the point that its harmonic gravitational wave emission greatly overwhelms everything else, in the Galaxy, in the universe, and in the detector itself. In fact, this detection is registered with

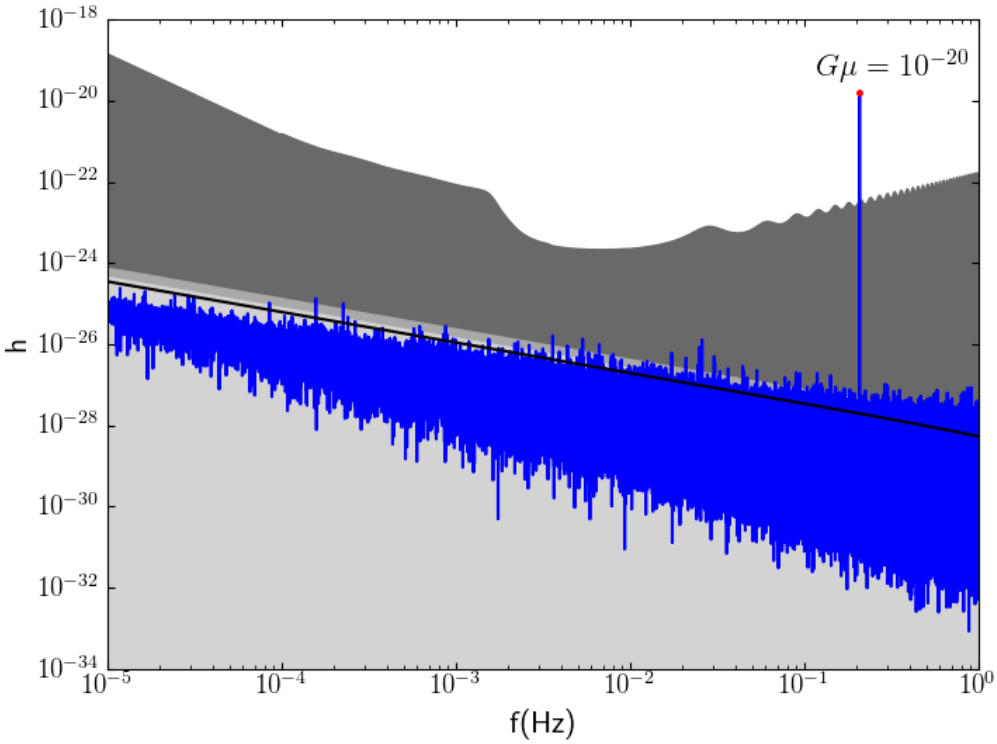

Figure 4.1: Snapshot of a particular realization capturing a detection in the simulation set for the physical Galaxy with the rocket effect at $G\mu = 10^{-20}$, $\alpha = 0.1$. The composition of the figure is identical to that of fig. 3.7.

a signal-to-noise ratio $\varrho \sim 450$, making it unmissable as a persistent source of gravitational waves.

Another feature to note in fig. 4.1 is the fact that without the artificially inflated loop abundance in the Galaxy in simulation sets in the toy models, the stochastic background as a source of confusion noise is now quite noticeable. In fact, we can see that the Galactic background emitted by cosmic string loops in the physical Galaxy is approximately comparable to the stochastic background from loops in the universe. Of course, both become quite unimportant for loops in simulation sets with these low values of string tension, where LISA instrumental noise with the Galactic WD binaries background absolutely dominates.

The overall statistical results for these simulation sets however, do not look as optimistic as that particular detection shown in fig. 4.1 does. With the low abundance of cosmic string loops in the physical Galaxy, such a detection is ultimately a rare event. First of all, we do not detect harmonic gravitational waves from individual nearby loops at all in the simulation set with $G\mu = 10^{-18}$. The number of detections increases for lower values of string tension, but remains low compared to the number of realizations in a simulation set. By a similar reasoning as that which led to eq. 3.57, with such low detection statistics, the total number of detections over the total number of realizations in a simulation set can be interpreted as the probability that any detection can be made over the course of the mission with duration $T_{\rm obs} = 1$ year. In fact, this interpretation is exact for the simulation set with $G\mu = 10^{-20}$ where no realization contains more than one detection.

We obtain estimates of statistics on detection probabilities for the two simulation sets with nonzero numbers of detections by bootstrapping detection numbers from realizations within simulation sets. Histograms generated by bootstrapping with 10^4 samples are presented in fig. 4.2, for simulation sets with $G\mu = 10^{-19}$ and 10^{-20}. We have verified that similar statistics can be obtained by bootstrapping with 10^3 samples, and therefore for these histograms, the bootstrapping process has fully converged. We mentioned above that no re-

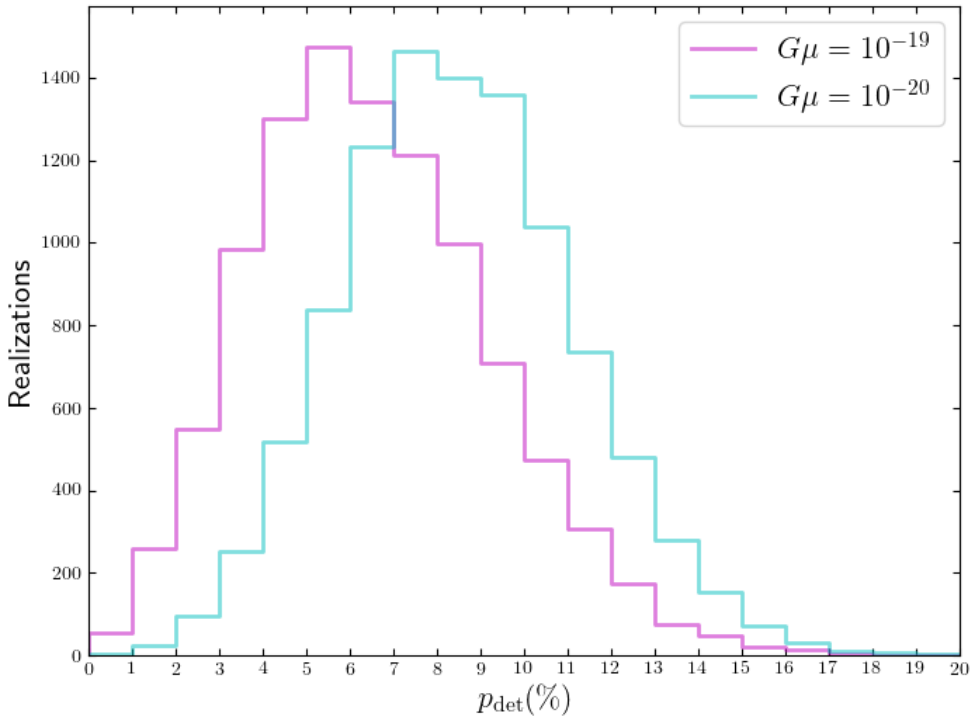

Figure 4.2: Histograms produced by bootstrapping the numbers of detections from realizations in simulation sets for the physical Galaxy with the rocket effect at $\alpha = 0.1$. Histograms in magenta and cyan represent results from simulation sets with $G\mu = 10^{-19}$ and 10^{-20}, respectively.

$-\log(G\mu)$	$p_{\rm det}$
$\lesssim 18$	$< 1\%$
19	$(6 \pm 3)\%$
20	$(8 \pm 3)\%$
21^*	$(6 \pm 2)\%$
22^*	$(1 \pm 1)\%$
$\gtrsim 23^*$	$< 1\%$

Table 4.1: Probability of detecting harmonic gravitational wave signal from nearby individual cosmic string loops with $\alpha = 0.1$ in the physical Galaxy by LISA with $T_{\rm obs} = 1$ year. Values marked with * are estimated from the simulation set at $G\mu = 10^{-20}$.

alization contains more than one detection in the simulation set with $G\mu = 10^{-20}$, meaning that bootstrapping is actually unnecessary for that simulation set, as the uncertainty should simply be $\Delta p_{\rm det} \sim \sqrt{p_{\rm det}}$.

We discussed in section 3.3.5 that further decreasing string tension beyond $G\mu = 10^{-20}$ provides no benefit to enhancing detection probability, because by $G\mu = 10^{-20}$, all loops emitting gravitational waves in the LISA frequency range are fully out of the rocket effect and decay regimes, and decreasing string tension further does not result in significant enhancement to loop abundance in the Galaxy. While on the other hand, gravitational wave emission from loops becomes weaker as string tension decreases as shown by eq. 2.55. This enables us to estimate detection probabilities for loops with $G\mu < 10^{-20}$ from the simulation set with $G\mu = 10^{-20}$ by effectively increasing the requirement for the signal-to-noise ratio. We also perform bootstrapping for these estimated detection probabilities to obtain statistics.

Complete results for the probability of detecting harmonic gravitational wave signal from nearby individual cosmic string loops in the physical Galaxy by LISA with $T_{\rm obs} = 1$ year are summarized in table 4.1. It is clear that as string tension decreases, the true sweetspot in the parameter space for making detections starts at $G\mu \sim 10^{-19}$ and diminishes gradually for $G\mu < 10^{-20}$ with $\alpha = 0.1$, for reasons outlined below.

Unlike results from simulations sets in the toy models, for simulation sets of the physical

Galaxy, increasing string tension from $G\mu = 10^{-20}$ decreases detection probability. We have in fact already touched on this issue in section 3.3.9. The reason is the absolute dominance of the LISA instrumental noise with the Galactic WD binaries background over other sources of noise in simulation sets for the physical Galaxy, while the dominance is not so strong for $G\mu \gtrsim 10^{-19}$ in simulation sets in the toy models. For this reason, we remarked in section 3.3.9 that the reduction in detection probability for simulation sets for the physical Galaxy from those in the toy models is expected to be steeper than $\kappa = \frac{2}{3}$ and closer to $\kappa = \frac{5}{6}$. Physically, loops emitting harmonic gravitational waves in the LISA frequency range with $G\mu > 10^{-19}$ cannot be easily resolved individually as a result of low loop abundance in the Galaxy, because they suffer significantly from the rocket effect and loop decay.

We discussed above that loops emitting gravitational waves in the LISA frequency range with $G\mu < 10^{-20}$ are not significantly more abundant in the Galaxy than those with $G\mu = 10^{-20}$, while they do have weaker gravitational wave emission. Thus, the detection probability is expected to decrease when string tension is decreased beyond $G\mu \sim 10^{-20}$. Loops emitting gravitational waves in the LISA frequency range with $G\mu \sim 10^{-19}$ - 10^{-21} have gravitational wave emission that is just sufficiently weak to keep them outside of the rocket effect and decay regimes, and therefore this region represents the sweetspot in the parameter space for detection. Unfortunately, we have confirmed our prediction from section 3.3.9 based on results from simulation sets in the toy models, that direct detection of harmonic gravitational waves from individual nearby cosmic string loops by LISA is simply not very likely even under the most favorable conditions, as shown by the summary of physical detection probabilities in table 4.1.

4.2 Results with Massless Neutrinos

4.2.1 Detection of Signal from Individual Loops

We present in this section results with the standard ΛCDM cosmological model and massless neutrinos, often adopted by other studies on detecting gravitational waves from cosmic string loops[35, 31, 29]. Compared to this model, our treatment of the neutrino mass in the evolution of the universe described in section 3.1.1 effectively overestimates the radiation energy density in the universe today, resulting in a greater loop abundance in the Galaxy by about a factor of ~ 10. Given that with our cosmological model, the probabilities of directly detecting harmonic gravitational waves from nearby individual loops summarized in table 4.1 are already low, this exercise is undertaken mostly in the spirit of completeness and for the ease of direct comparisons to other studies on detecting gravitational waves from cosmic string loops, as we already know from results presented in section 4.1.2 that such detections by LISA are unlikely.

Given the reduction in loop abundance in the Galaxy with standard cosmology and massless neutrinos, we know that detection probabilities will be reduced further from those in table 4.1. An estimate can be obtained by using the heuristic method of estimating the detection probability developed in section 3.3.9 for making predictions for the physical Galaxy based on results from simulation sets in the toy models. Using eq. 3.56 with $\kappa = \frac{2}{3}$ and results from table 4.1, we see that for a reduction in loop abundance in the Galaxy by a factor of ~ 10, we should expect $\sim 8/10^{\frac{2}{3}} \approx 2$ detections out of the total of 100 realizations for the simulation set with $G\mu = 10^{-20}$, and up to ~ 1 detection for the simulation set with $G\mu = 10^{-19}$. Of course the requirement for the signal-noise-ratio eq. 3.39 stays the same as for all other detections.

For these simulations sets, we adopt standard ΛCDM cosmology with massless neutrinos

and fiducial values of cosmological parameters from Planck 2018 results[95, 29],

$$H_0 = 67.8 \text{ km/s/Mpc}; \tag{4.1}$$

$$\Omega_{\text{m},0} = 0.308; \tag{4.2}$$

$$\Omega_{\text{r},0} = 9.1476 \times 10^{-5}; \tag{4.3}$$

$$\Omega_{\Lambda,0} = 1 - \Omega_{\text{m},0} - \Omega_{\text{r},0}. \tag{4.4}$$

The actual results from simulation sets for the physical Galaxy with the standard cosmology described above are in good agreement with our expectation. We have no detection at all from the simulation set with $G\mu = 10^{-19}$, and indeed two detections out of the 100 realizations in the simulation set with $G\mu = 10^{-20}$. Thus, we can conclude that with standard ΛCDM cosmology and massless neutrinos, direct detection of harmonic gravitational waves from nearby individual cosmic string loops by LISA is very unlikely, with

$$p_{\text{det},20} \sim 2\% \tag{4.5}$$

if loops are created with $G\mu = 10^{-20}$. In a universe containing loops created with all other values of string tension, we expect $p_{\text{det}} < 1\%$.

4.2.2 Detection of the Galactic Background

As a side result, we compute the total background gravitational wave strain amplitude from all cosmic string loops clumped in the dark matter halo of the Galaxy taking into consideration loop ejection as a result of the rocket effect, with loops created following the one-scale model eq. 2.18 with $\alpha = 0.1$. For these calculations we adopt the same standard ΛCDM cosmology with massless neutrinos as that described in section 4.2.1.

The Galactic gravitational wave background from cosmic string loops correctly binned

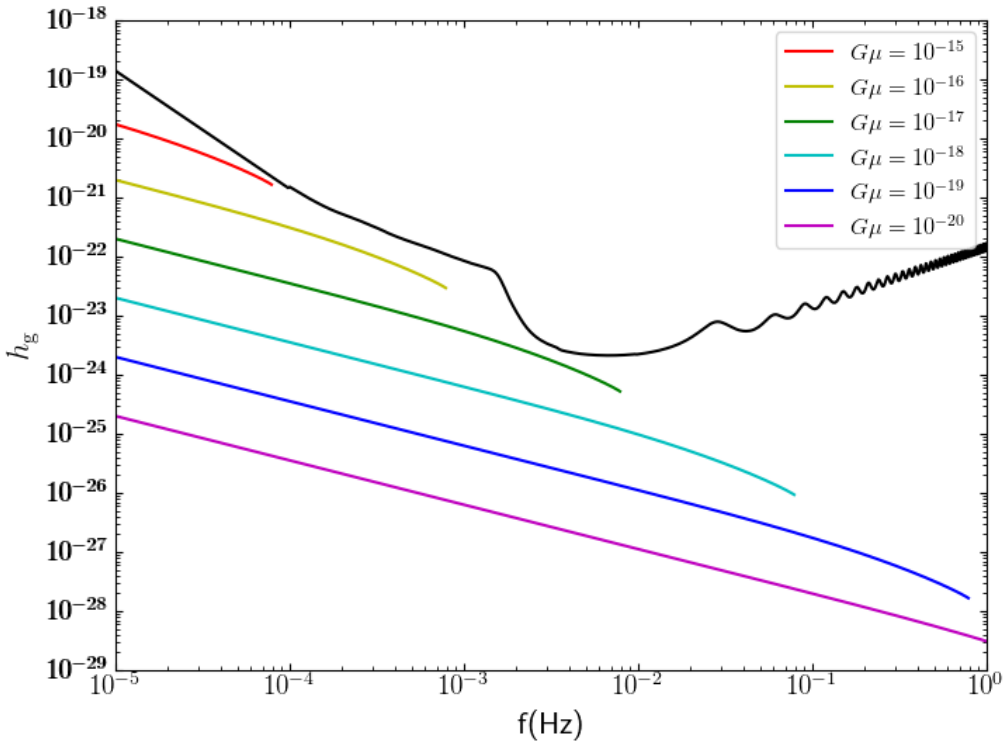

Figure 4.3: The total background gravitational wave strain amplitude from all cosmic string loops in the Galaxy with standard cosmology and massless neutrinos, plotted in colors following the rainbow order from $G\mu = 10^{-15}$ to 10^{-20} with $\alpha = 0.1$. The black curve represents LISA instrumental noise with the Galactic WD binaries background, for $T_{\rm obs} = 1$ year.

for the observation duration $T_{\rm obs} = 1$ year is presented in fig. 4.3 for $G\mu = 10^{-15}$ to 10^{-20} with colors following the rainbow order. LISA instrumental noise for a mission duration $T_{\rm obs} = 1$ year with the Galactic WD binaries background is also plotted for comparison. Detailed configurations behind this source of noise is discussed in section 3.2.3. Clearly, the very first impression we have from the figure is that the Galactic background cannot be detected by LISA.

The curves for the Galactic background in fig. 4.3 are terminated at the frequency where loops in the Galaxy enter the decay regime. As we discussed in sections 2.3.2 and 3.3.6, for the orbit of the solar system in the Galaxy, this is essentially the same as the truncation frequency $f_\odot$. For loops in the decay regime, the simple rebinning eq. 3.53 is no longer valid and the correct relation to use is eq. 3.51. We can see clearly from the latter that as a loop enters the decay regime, the denominator quickly becomes very small, and the number density of loops emitting gravitational waves in a LISA frequency bin decreases rapidly. This means that loops created at similar times which, without significant loop decay should emit gravitational waves in the same frequency bin, are now stretched across many frequency bins because their sizes now differ significantly, greatly reducing loop number density in a frequency bin. This is basically a manifestation of loop evaporation as they come close to the end of their lives. Thus, beyond termination points in the decay regime, the Galactic background just drops rapidly, and there is really no meaning in calculating it at those frequencies for our purpose. In fact, the unresolved Galactic background itself may become undefined in the decay regime given the large reduction in loop abundance in the Galaxy. For all practical purposes, the Galactic background basically vanishes quickly beyond the termination frequency. Loops with $G\mu = 10^{-20}$ decay sufficiently slowly due to weak gravitational wave emission that those emitting gravitational waves in the LISA frequency range have not decayed significantly, as we discussed in earlier sections, most recently in section 4.1.2. Loops with $G\mu > 10^{-15}$ emitting gravitational waves in the LISA

frequency range are all in the decay regime.

For the possibility of detection of the Galactic gravitational wave background from cosmic string loops by LISA, the above discussion has little relevance, as even if we ignored loop decay and insisted on using eq. 3.53, the change in slope of the Galactic background strain amplitude as a function of frequency due to loop truncation by the rocket effect at these termination frequencies in fig. 4.3, means that the Galactic background still would not be detectable by LISA.

Recall from section 3.2.3, that the low-frequency part of the noise curve in fig. 4.3 is primarily due to the Galactic WD binaries background, causing a cliff-like feature at $f \sim 10^{-3}$ Hz when the LISA instrumental noise becomes dominant at higher frequencies. Thus, the Galactic background from loops with higher string tension is simply not detectable because of the confusion from the Galactic WD binaries background.

Comparing the Galactic background fig. 4.3 to the stochastic background fig. 3.5 reduced by a factor of ~ 3 to account for cosmology, we see that the Galactic background emitted by loops outside of the decay regime is about comparable to the stochastic background. This is the same conclusion we made in section 4.1.2 by observing fig. 4.1. However, for the Galactic background, we are only receiving gravitational waves emitted by loops in the Galaxy at the present time, and not from the past. This is the reason that the Galactic gravitational wave background from cosmic string loops is not detectable by LISA, while the stochastic background from loops can possibly be detected. For loops that are well clumped in the Galaxy, this relation between the Galactic background and the stochastic background should be more or less general across different loop formation models.

We are therefore led to the conclusion that despite the significant clumping of cosmic string loops in the Galaxy discussed in section 2.3.1, detection of gravitational waves emitted by cosmic string loops in the Galaxy by LISA is likely only possible for very strong gravitational wave signal emitted by individual loops. This can either be harmonic grav-

itational waves from loops with low string tension located in close proximity to the solar system as we analyze in this work, or high frequency burst signal from background loops with higher string tension analyzed in the work of ref. [11].

CHAPTER 5

CONCLUSION

We developed through this study, a robust framework for numerically simulating cosmic string loops that have clumped in the Galaxy taking into account effects due to loop recoil caused by anisotropy in gravitational wave emission by loops, and generating the expected gravitational wave signal observable by LISA for a one-year mission. The methodology we developed to accomplish this task is highly flexible and can be adapted relatively easily to produce results from simulations configured with any reasonable cosmic string loop formation and cosmological models. Moreover, the toolset in our simulations represents particularly efficient methods for simulating cosmic string loops in the Galaxy for the purpose of detecting harmonic gravitational waves from resolved loops located in close proximity to the solar system, even with extremely high loop abundance in the Galaxy, as evidenced by simulations of the toy models presented in chapter 3. Along the way, we also derived a method for estimating the results to be expected from simulations configured with a set of loop formation and cosmological models based on results already obtained from simulations configured with another set of models.

Compared to the power and adaptability of the simulation methodology developed to accomplish our objective of predicting the detectability of harmonic gravitational waves from nearby individual cosmic string loops, the actual results obtained from simulation sets of loops in the physical Galaxy are arguably less exciting. The immediate conclusion we can draw based on results presented in section 4.1.2 and summarized in table 4.1, as well as results presented in section 4.2.1, is that detection of harmonic gravitational waves from resolved loops in the Galaxy by LISA is unlikely for field theory cosmic string loops anywhere in the parameter space, even with the most favorable loop formation and cosmological models.

Moreover, we can further conclude based on results shown in fig. 4.3 in section 4.2.2, that LISA will also not be able to detect the unresolved gravitational wave background from

the collective gravitational wave emission of all cosmic string loops in the Galaxy, despite complete clumping of loops in the Galaxy following the dark matter density profile.

In our approach of directly resolving signal from individual loops which focuses on harmonic gravitational waves from loops, the critical ingredient for detection is the possibility of individual loops being located in extreme proximity to the solar system. This requirement essentially eliminates models with higher string tension $G\mu \gtrsim 10^{-18}$ because of decreased loop abundance in the Galaxy due to loop decay, and even more importantly, because of the rocket effect which completely prevents detection when the truncation radius falls below the solar system orbit in the Galaxy. For loops with such low string tension, their overall gravitational wave emission from both the Galactic and the stochastic backgrounds is weak, and the noise is strongly dominated by LISA instrumental noise and the Galactic WD binaries background. When this is the case, results from our simulation have shown that resolving harmonic signal from individual loops strongly prefers higher loop abundance in the Galaxy and therefore a very low string tension $10^{-21} \lesssim G\mu \lesssim 10^{-19}$, despite the associated weaker gravitational wave emission from loops.

This conclusion on string tension for our approach presented above should be contrasted to that of the other approach of directly resolving signal from individual loops which focuses on detecting burst signals from loops in the Galaxy, as we discussed in chapter 1. For burst detection, a relatively higher string tension $G\mu > 10^{-15}$ is preferred instead[11]. This is because for the same detector frequency range, the target loops for burst detection are large and emitting very low frequency harmonic gravitational waves, and such large loops are not significantly affected by loop decay and the rocket effect even with higher string tension, though they do have a lower number density at formation. Thus, in the case of burst detection, a relatively high string tension is preferred for the stronger gravitational wave emission of such loops.

For initial loops sizes at formation, both approaches of resolving gravitational wave signal

from individual loops prefer loops created with large initial size $\alpha = 0.1$, because for a given frequency range, these loops have higher number density at formation, and more importantly, they clump much better in the Galaxy than those created with small initial sizes do, further enhancing the abundance of loops with large initial size in the Galaxy significantly.

We have tested the effect of cosmological models and presented results in chapter 4, where we concluded that configuring simulations with the standard ΛCDM cosmology with massless neutrinos results in significant further reduction in probabilities of directly detecting harmonic signal from individual loops by LISA.

We will now discuss the meaning of our results presented above with respect to loop formation models. Recall from section 2.1.2 where we remarked that compared to the distribution of initial loop sizes produced by the most state-of-the-art loop formation simulation[3], our one-scale model overestimates loop number density for $\alpha > 10^{-5}$ by up to about two orders of magnitude at $\alpha = 0.1$, and is effectively in agreement at $\alpha \sim 10^{-5}$. We can immediately see that with the distribution of initial loop sizes from the loop formation simulation, loops created with large initial sizes cannot contribute to detection of harmonic signal from individual loops in the Galaxy.

We now turn our attention to loops with small initial sizes. The reason for the varying differences in effective normalization factors between the two models for loops with different initial sizes is because, for the distribution of initial loops sizes from the loop formation simulation, effectively $n \propto \alpha^{-\frac{3}{2}}$, whereas for the one-scale model, $n \propto \alpha^{-1}$. Thus, compared to the former, the latter underestimates loop number density at formation for $\alpha < 10^{-5}$ due to the extra $\frac{1}{2}$ power on α. However, for a given detector frequency range, loop abundance in the Galaxy decreases when α decreases because such loops are created later in time. This approximately offsets the extra $\frac{1}{2}$ power on α for loop abundance in the Galaxy. The overall effect is that with the distribution of initial loop sizes from the loop formation simulation, loop abundance in the Galaxy remains approximately the same when α is varied, at a level

similar to that of the one-scale model at $\alpha = 10^{-5}$. Our results already show that detection of harmonic signal from individual loops is not possible with the one-scale model at $\alpha = 10^{-5}$. Given that loops with even smaller initial sizes also clump poorly in the Galaxy, we can therefore conclude that resolving harmonic gravitational waves from nearby loops by LISA will be even more unlikely than that suggested by our results, if cosmic string loops are created following the most state-of-the-art loop formation simulation.

In section 2.3.2, we mentioned that the rocket effect incorporated into our simulation is derived[4] with the cusps-dominated gravitational wave emission spectrum, which is associated with the highest degree of anisotropy in the direction of emission, as we discussed in section 2.2.2. This maximizes the recoil experienced by loops from emitting gravitational waves, meaning that the quantity characterizing the momentum transfer to loops due to the rocket effect, Γ_P in eq. 2.56, is maximized. Moreover, the derivation also assumes that the overall direction of momentum transfer as a result of the rocket effect remains constant over time, and therefore making this the Stark problem of cosmic string loops. However, loop trajectories can be complicated, as we discussed in section 2.2.1 that the solution is very general. In reality, cosmic string loops probably encompass a wide range of loop trajectories with various small-scale features, i.e. cusps and kinks, present along the loop. The overall direction of anisotropy in the total gravitational wave emission can also quite possibly change over time. Thus, the treatment of the rocket effect incorporated into our simulation is a strong version, which effectively corresponds to a scenario relatively optimized for loop ejection from the Galaxy[11]. For the orbit of the solar system in the Galaxy however, the possibility of reduced loop ejection due to the rocket effect being somewhat weaker in reality than that incorporated in our simulation does not have a significant effect on the results. We discussed in sections 2.3.2 and 3.3.6 that at the solar system orbit, the rocket effect essentially tracks loop decay for our purpose, i.e. that $f_\odot$ is at the beginning of the decay regime as frequency increases. We also discussed in section 4.2.2 that loop abundance in the physi-

cal Galaxy drops quickly in the decay regime, making this frequency range unimportant for direct detection of harmonic gravitational wave from resolved loops. These facts combined mean that incorporating an overall weaker version of the rocket effect will have little effect on detection statistics, because the signal will be eliminated by loop decay anyway in the decay regime, even when $f < f_{\odot}$ as a result of the weaker rocket effect. The situation will of course be different if the solar system is located further away from the center of the Galaxy, there having a weaker version of the rocket effect should indeed lead to higher detection statistics. We discussed in section 2.3.1 that the rocket effect acts against loop clumping in the Galaxy, and therefore a weaker version of the rocket effect should enable better clumping. But we discussed there that for the low values of string tension in our simulation, loops are already well clumped even with the relatively strong rocket effect. This fact led us to incorporate complete clumping of loops in the Galaxy, which is already the best-case scenario that cannot be further enhanced by having a weaker version of the rocket effect. Thus, the possibility that the rocket effect may be weaker in reality than that incorporated into our simulation has no significant effect on predictions of detection statistics obtained for the physical Galaxy.

We discussed earlier that in the favored region of the parameter space, noise is dominated by LISA instrumental noise with the Galactic WD binaries background. Detection of gravitational waves from individual loops primarily occurs at higher frequencies where loop is more abundant in the Galaxy, outside of the region dominated by the Galactic WD binaries background. Thus, noise is essentially dominated by LISA instrumental noise. We can then ask the question, will resolving harmonic signal from individual loops be likely if we have a perfect detector with no noise at all? To answer this question, we analyze the simulation set at $G\mu = 10^{-20}$, $\alpha = 0.1$ without LISA instrumental noise. The Galactic WD binaries background is also turned off, but that should have no significant effect as discussed above. The answer is yes, with the histogram of detections presented in fig. 5.1. We see that every

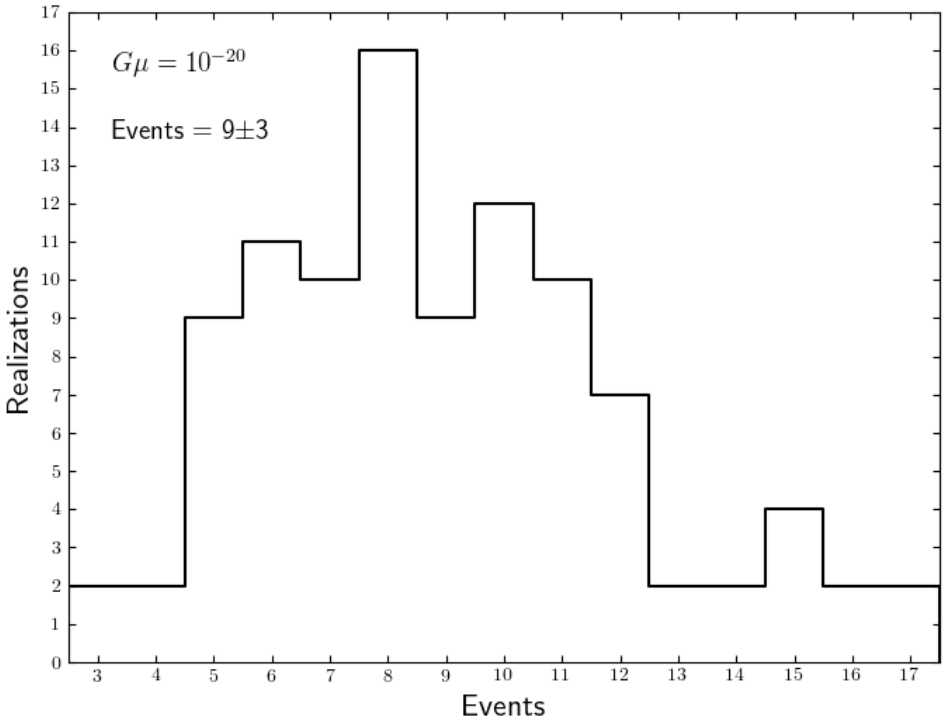

Figure 5.1: Histogram of detections satisfying the signal-to-noise requirement eq. 3.39 for the simulation set of the physical Galaxy with the rocket effect at $G\mu = 10^{-20}$, $\alpha = 0.1$, without LISA instrumental noise and the Galactic WD binaries background.

single realization out of a total of 100 realizations in the simulation set has detections, with the total expected number of detections $N_{\rm det,tho} = 9 \pm 3$. From the discussion in section 3.3.7, we see that this expected detection number without LISA instrumental noise should be more or less independent of loop formation and cosmological models. Thus, a future LISA-like gravitational wave detector with an improvement in sensitivity in strain amplitude by $\gtrsim 2$ orders of magnitude will very likely be able to detect harmonic gravitational waves from individual loops in the Galaxy if $G\mu \sim 10^{-19}$ - 10^{-20}.

While a LISA-like gravitational wave detector with improved sensitivity may only exist in the distant future at the time this manuscript is prepared, advanced LIGO (aLIGO) already exists today. Cosmic string loops emitting harmonic gravitational waves in the LIGO frequency range must have very low string tension $G\mu \lesssim 10^{-22}$ to avoid the rocket effect and loop decay. When operating at design sensitivity[96], a one-year observation on aLIGO can reach down to the strain amplitude $h \sim 5 \times 10^{-28}$. Projecting the curves in fig. 4.3, we see that this is insufficient for detecting the Galactic background from loops. However, the difference between aLIGO sensitivity and the Galactic background from loops with $G\mu \lesssim 10^{-22}$ is not very different from that between LISA sensitivity and the Galactic background from loops with $G\mu \lesssim 10^{-19}$, while the number of loops in the Galaxy emitting harmonic gravitational waves in a frequency bin is enhanced by one to two orders of magnitude in the LIGO frequency range. On the surface, it appears that detection of harmonic gravitational waves from individual loops in the Galaxy by aLIGO operating at design sensitivity is a real possibility, if string tension is very low $G\mu \lesssim 10^{-22}$, and the loops are created with large initial size $\alpha \sim 0.1$. To make quantitative predictions, this possibility should be systematically explored through numerical simulations in a future study similar to this one in nature.

Last but not least, an important avenue for future exploration is provided by string theory. We mentioned in chapter 1 that cosmic superstrings can easily be created at the

end of various brane inflation scenarios[24], and that the richness of the theory allows for greatly relaxed theoretical restrictions on the characteristics of cosmic superstrings. An important such property of cosmic superstrings is the intercommutation probability $P_{\rm int}$, which unlike field theory cosmic strings, is now permitted to be much less than 1 as we mentioned in section 2.1.1, down to the very low value of $P_{\rm int} \sim 10^{-3}$[97, 24]. It may be somewhat counterintuitive that in the scaling solution of loop formation, a reduction in $P_{\rm int}$ actually leads to an enhancement in loop number density at formation. This is a property of the scaling solution, and a heuristic argument[37] can be offered. The initial loop size in the scaling solution $l = \alpha t$ is a measure of the intercommutation rate of infinite strings, and therefore a reduction in $P_{\rm int}$ from unity will tend to reduce initial loop size by $P_{\rm int}$. Then to maintain the scaling solution, the intercommutation rate of infinite strings must be boosted by $P_{\rm int}^{-1}$ to compensate, resulting in an enhancement to loop number density by $P_{\rm int}^{-1}$. The actual amount of enhancement varies depending on the details of the loop formation model[98, 99, 100, 11], and can be as high as $P_{\rm int}^{-2}$[98, 11], resulting in an enhancement to loop number density by a factor of 10^6. From our method for estimating detection probabilities eq. 3.56 and results in table 4.1, we see that taking into account cosmological models, such an enhancement to loop abundance in the Galaxy means that direct detection of harmonic gravitational waves from nearby individual loops by LISA will basically be a certainty for loops outside of the rocket effect and decay regimes, $G\mu \lesssim 10^{-15}$ down to at least $G\mu \sim 10^{-22}$. In fact, detection of the Galactic background itself will be likely down to $G\mu \sim 10^{-20}$. Even for a more conservative enhancement $P_{\rm int}^{-\frac{2}{3}}$[100, 11], we can estimate using eq. 3.56 that the probability of resolving harmonic signal from individual loops in the Galaxy will be close to $\sim 50\%$ for loops with $G\mu \sim 10^{-20}$ with standard ΛCDM cosmology and massless neutrinos. The richness of the string theory framework leaves the door to direct detection of harmonic gravitational waves from cosmic string loops wide open. Future studies are necessary to explore the possibility of detecting such signal with various models of cosmic

superstrings. For a loop formation model, LISA observations will place combined constraints on the $(G\mu, P_{\rm int})$ parameter space, regardless of whether detection of cosmic string loops is made. These observations will finally start experimentally testing string theory.

REFERENCES

[1] C. Ringeval, Adv. Astron. **2010**, 1–28 (2010), URL http://dx.doi.org/10.1155/2010/380507.

[2] A. Vilenkin and E. P. S. Shellard, *Cosmic strings and other topological defects* (Cambridge University Press, 1994).

[3] J. J. Blanco-Pillado, K. D. Olum, and B. Shlaer, Phys. Rev. D **89**, 023512 (2014), URL https://link.aps.org/doi/10.1103/PhysRevD.89.023512.

[4] D. F. Chernoff, *Clustering of superstring loops* (2009), 0908.4077.

[5] K. Danzmann, *Laser interferometer space antenna: A cornerstone mission for the observation of gravitational waves, esa system and technology study report* (2000).

[6] S. L. Larson, W. A. Hiscock, and R. W. Hellings, Phys. Rev. D **62**, 062001 (2000), URL https://link.aps.org/doi/10.1103/PhysRevD.62.062001.

[7] W. A. Hiscock, S. L. Larson, J. R. Routzahn, and B. Kulick, Astrophys. J. **540**, L5–L8 (2000), URL http://dx.doi.org/10.1086/312867.

[8] I. Chuang, R. Durrer, N. Turok, and B. Yurke, Science **251**, 1336 (1991), URL https://science.sciencemag.org/content/251/4999/1336.

[9] T. W. B. Kibble, J. Phys. A: Math. Gen. **9**, 1387 (1976).

[10] R. Durrer, M. Kunz, and A. Melchiorri, Phys. Rep. **364**, 1 (2002), URL http://www.sciencedirect.com/science/article/pii/S0370157302000145.

[11] D. F. Chernoff and S.-H. H. Tye, J. Cosmol. Astropart. Phys. **2018**, 002 (2018).

[12] Planck Collaboration, Ade, P. A. R., Aghanim, N., Armitage-Caplan, C., Arnaud, M., Ashdown, M., Atrio-Barandela, F., Aumont, J., Baccigalupi, C., Banday, A. J., et al., Astron. Astrophys. **571**, A25 (2014), URL https://doi.org/10.1051/0004-6361/201321621.

[13] T. Charnock, A. Avgoustidis, E. J. Copeland, and A. Moss, Phys. Rev. D **93**, 123503 (2016), URL https://link.aps.org/doi/10.1103/PhysRevD.93.123503.

[14] D. F. Chernoff and S.-H. H. Tye, *Cosmic string detection via microlensing of stars* (2007), 0709.1139.

[15] J. L. Christiansen, E. Albin, K. A. James, J. Goldman, D. Maruyama, and G. F. Smoot, Phys. Rev. D **77**, 123509 (2008), URL https://link.aps.org/doi/10.1103/PhysRevD.77.123509.

[16] J. L. Christiansen, E. Albin, T. Fletcher, J. Goldman, I. P. W. Teng, M. Foley, and G. F. Smoot, Phys. Rev. D **83**, 122004 (2011), URL https://link.aps.org/doi/10.1103/PhysRevD.83.122004.

[17] J. K. Bloomfield and D. F. Chernoff, Phys. Rev. D **89**, 124003 (2014), URL https://link.aps.org/doi/10.1103/PhysRevD.89.124003.

[18] R. H. Cyburt, B. D. Fields, K. A. Olive, and E. Skillman, Astropart. Phys. **23**, 313 (2005), URL http://www.sciencedirect.com/science/article/pii/S092765050500006X.

[19] S. Ölmez, V. Mandic, and X. Siemens, Phys. Rev. D **81**, 104028 (2010), URL https://link.aps.org/doi/10.1103/PhysRevD.81.104028.

[20] C. Hogan and M. Rees, Nature **311**, 109 (1984).

[21] J. J. Blanco-Pillado, K. D. Olum, and X. Siemens, Phys. Lett. B **778**, 392 (2018), URL http://www.sciencedirect.com/science/article/pii/S0370269318300583.

[22] B. P. Abbott, R. Abbott, T. D. Abbott, F. Acernese, K. Ackley, C. Adams, T. Adams, P. Addesso, R. X. Adhikari, V. B. Adya, et al. (LIGO Scientific Collaboration and Virgo Collaboration), Phys. Rev. D **97**, 102002 (2018), URL https://link.aps.org/doi/10.1103/PhysRevD.97.102002.

[23] B. P. Abbott, R. Abbott, T. D. Abbott, S. Abraham, F. Acernese, K. Ackley, C. Adams, V. B. Adya, C. Affeldt, M. Agathos, et al. (LIGO Scientific and Virgo Collaboration), Phys. Rev. D **100**, 061101 (2019), URL https://link.aps.org/doi/10.1103/PhysRevD.100.061101.

[24] D. F. Chernoff and S. H. H. Tye, Int. J. Mod. Phys. **D24**, 1530010 (2015).

[25] C. Ringeval, M. Sakellariadou, and F. R. Bouchet, J. Cosmol. Astropart. Phys. **2007**, 023 (2007).

[26] A. H. Guth, Phys. Rev. D **23**, 347 (1981), URL https://link.aps.org/doi/10.1103/PhysRevD.23.347.

[27] A. Linde, Phys. Lett. B **108**, 389 (1982), URL http://www.sciencedirect.com/science/article/pii/0370269382912199.

[28] E. W. Kolb and M. S. Turner, *The Early Universe* (Westview Press, 1990).

[29] P. Auclair, J. J. Blanco-Pillado, D. G. Figueroa, A. C. Jenkins, M. Lewicki, M. Sakellariadou, S. Sanidas, L. Sousa, D. A. Steer, J. M. Wachter, et al., *Probing the gravitational wave background from cosmic strings with lisa* (2019), 1909.00819.

[30] P. Amaro-Seoane, H. Audley, S. Babak, J. Baker, E. Barausse, P. Bender, E. Berti, P. Binetruy, M. Born, D. Bortoluzzi, et al., *Laser interferometer space antenna* (2017), 1702.00786.

[31] M. R. DePies and C. J. Hogan, *Harmonic gravitational wave spectra of cosmic string loops in the galaxy* (2009), 0904.1052.

[32] T. Vachaspati and A. Vilenkin, Phys. Rev. D **31**, 3052 (1985), URL https://link.aps.org/doi/10.1103/PhysRevD.31.3052.

[33] T. Damour and A. Vilenkin, Phys. Rev. D **64**, 064008 (2001), URL https://link.aps.org/doi/10.1103/PhysRevD.64.064008.

[34] T. Kibble, Nucl. Phys. B **252**, 227 (1985), URL http://www.sciencedirect.com/science/article/pii/0550321385904390.

[35] M. R. DePies and C. J. Hogan, Phys. Rev. D **75**, 125006 (2007), URL https://link.aps.org/doi/10.1103/PhysRevD.75.125006.

[36] M. R. Depies, *Gravitational waves and light cosmic strings* (2009), 0908.3680.

[37] C. J. Hogan, Phys. Rev. D **74**, 043526 (2006), URL https://link.aps.org/doi/10.1103/PhysRevD.74.043526.

[38] R. R. Caldwell and B. Allen, Phys. Rev. D **45**, 3447 (1992), URL https://link.aps.org/doi/10.1103/PhysRevD.45.3447.

[39] C. J. A. P. Martins and E. P. S. Shellard, Phys. Rev. D **65**, 043514 (2002), URL https://link.aps.org/doi/10.1103/PhysRevD.65.043514.

[40] C. J. A. P. Martins and E. P. S. Shellard, Phys. Rev. D **54**, 2535 (1996), URL https://link.aps.org/doi/10.1103/PhysRevD.54.2535.

[41] J. N. Moore, E. P. S. Shellard, and C. J. A. P. Martins, Phys. Rev. D **65**, 023503 (2001), URL https://link.aps.org/doi/10.1103/PhysRevD.65.023503.

[42] C. J. A. P. Martins, J. N. Moore, and E. P. S. Shellard, Phys. Rev. Lett. **92**, 251601 (2004), URL https://link.aps.org/doi/10.1103/PhysRevLett.92.251601.

[43] V. Vanchurin, K. Olum, and A. Vilenkin, Phys. Rev. D **72**, 063514 (2005), URL https://link.aps.org/doi/10.1103/PhysRevD.72.063514.

[44] V. Vanchurin, K. D. Olum, and A. Vilenkin, Phys. Rev. D **74**, 063527 (2006), URL https://link.aps.org/doi/10.1103/PhysRevD.74.063527.

[45] K. D. Olum and V. Vanchurin, Phys. Rev. D **75**, 063521 (2007), URL https://link.aps.org/doi/10.1103/PhysRevD.75.063521.

[46] C. J. A. P. Martins and E. P. S. Shellard, Phys. Rev. D **73**, 043515 (2006), URL https://link.aps.org/doi/10.1103/PhysRevD.73.043515.

[47] J. Polchinski and J. V. Rocha, Phys. Rev. D **74**, 083504 (2006), URL https://link.aps.org/doi/10.1103/PhysRevD.74.083504.

[48] J. Polchinski and J. V. Rocha, Phys. Rev. D **75**, 123503 (2007), URL https://link.aps.org/doi/10.1103/PhysRevD.75.123503.

[49] F. Dubath, J. Polchinski, and J. V. Rocha, Phys. Rev. D **77**, 123528 (2008), URL https://link.aps.org/doi/10.1103/PhysRevD.77.123528.

[50] L. Lorenz, C. Ringeval, and M. Sakellariadou, J. Cosmol. Astropart. Phys. **2010**, 003 (2010).

[51] C. Ringeval and T. Suyama, J. Cosmol. Astropart. Phys. **2017**, 027 (2017).

[52] J. J. Blanco-Pillado, K. D. Olum, and B. Shlaer, Phys. Rev. D **83**, 083514 (2011), URL https://link.aps.org/doi/10.1103/PhysRevD.83.083514.

[53] T. Kibble and N. Turok, Phys. Lett. B **116**, 141 (1982), URL http://www.sciencedirect.com/science/article/pii/0370269382909935.

[54] D. Garfinkle and T. Vachaspati, Phys. Rev. D **36**, 2229 (1987), URL https://link.aps.org/doi/10.1103/PhysRevD.36.2229.

[55] J. J. Blanco-Pillado, K. D. Olum, and B. Shlaer, Phys. Rev. D **92**, 063528 (2015), URL https://link.aps.org/doi/10.1103/PhysRevD.92.063528.

[56] J. M. Quashnock and D. N. Spergel, Phys. Rev. D **42**, 2505 (1990), URL https://link.aps.org/doi/10.1103/PhysRevD.42.2505.

[57] J. J. Blanco-Pillado and K. D. Olum, Phys. Rev. D **96**, 104046 (2017), URL https://link.aps.org/doi/10.1103/PhysRevD.96.104046.

[58] J. M. Wachter and K. D. Olum, Phys. Rev. Lett. **118**, 051301 (2017), URL https://link.aps.org/doi/10.1103/PhysRevLett.118.051301.

[59] J. M. Wachter and K. D. Olum, Phys. Rev. D **95**, 023519 (2017), URL https://link.aps.org/doi/10.1103/PhysRevD.95.023519.

[60] N. Turok, Nucl. Phys. B **242**, 520 (1984), URL http://www.sciencedirect.com/science/article/pii/0550321384904073.

[61] D. DeLaney, K. Engle, and X. Scheick, Phys. Rev. D **41**, 1775 (1990), URL https://link.aps.org/doi/10.1103/PhysRevD.41.1775.

[62] S. Weinberg, *Gravitation and Cosmology: Principles and Applications of the General Theory of Relativity* (John Wiley and Sons, 1972).

[63] B. Allen and P. Casper, Phys. Rev. D **50**, 2496 (1994), URL https://link.aps.org/doi/10.1103/PhysRevD.50.2496.

[64] P. Binétruy, A. Bohé, T. Hertog, and D. A. Steer, Phys. Rev. D **82**, 126007 (2010), URL https://link.aps.org/doi/10.1103/PhysRevD.82.126007.

[65] A. L. Chen, D. A. DiCarlo, and S. A. Hotes, Phys. Rev. D **37**, 863 (1988), URL https://link.aps.org/doi/10.1103/PhysRevD.37.863.

[66] R. R. Caldwell, R. A. Battye, and E. P. S. Shellard, Phys. Rev. D **54**, 7146 (1996), URL https://link.aps.org/doi/10.1103/PhysRevD.54.7146.

[67] B. Allen and E. P. S. Shellard, Phys. Rev. D **45**, 1898 (1992), URL https://link.aps.org/doi/10.1103/PhysRevD.45.1898.

[68] M. R. Anderson, *The mathematical theory of cosmic strings: Cosmic strings in the wire approximation* (CRC Press, 2003).

[69] S. Kuroyanagi, K. Miyamoto, T. Sekiguchi, K. Takahashi, and J. Silk, Phys. Rev. D **86**, 023503 (2012), URL https://link.aps.org/doi/10.1103/PhysRevD.86.023503.

[70] S. Kuroyanagi, K. Miyamoto, T. Sekiguchi, K. Takahashi, and J. Silk, Phys. Rev. D **87**, 023522 (2013), URL https://link.aps.org/doi/10.1103/PhysRevD.87.023522.

[71] C. J. Moore, R. H. Cole, and C. P. L. Berry, Class. Quant. Grav. **32**, 015014 (2015), URL http://dx.doi.org/10.1088/0264-9381/32/1/015014.

[72] S. A. Balbus, Proc. Nat. Acad. Sci. **113**, 11662 (2016), URL https://www.pnas.org/content/113/42/11662.

[73] J. B. Hartle, *Gravity : an introduction to Einstein's general relativity* (Addison Wesley, 2003).

[74] F. Biscani and D. Izzo, Mon. Not. R. Astron. Soc. **439**, 810 (2014), URL https://doi.org/10.1093/mnras/stt2501.

[75] G. Lantoine and R. Russell, Celest. Mech. Dyn. Astr. **109**, 333 (2011).

[76] J. P. Vinti, in *The Theory of Orbits in the Solar System and in Stellar Systems*, edited by G. I. Kontopoulos (1966), vol. 25 of *IAU Symposium*, p. 355.

[77] M. Maggiore, *Gravitational Waves. Vol. 1: Theory and Experiments*, Oxford Master Series in Physics (Oxford University Press, 2007), URL http://www.oup.com/uk/catalogue/?ci=9780198570745.

[78] N. J. Cornish and L. J. Rubbo, Phys. Rev. D **67**, 022001 (2003), URL https://link.aps.org/doi/10.1103/PhysRevD.67.022001.

[79] N. J. Cornish and L. J. Rubbo, Phys. Rev. D **67**, 029905 (2003), URL https://link.aps.org/doi/10.1103/PhysRevD.67.029905.

[80] N. J. Cornish and S. L. Larson, Class. Quant. Grav. **20**, S163–S170 (2003), URL http://dx.doi.org/10.1088/0264-9381/20/10/319.

[81] N. J. Cornish and S. L. Larson, Phys. Rev. D **67**, 103001 (2003), URL https://link.aps.org/doi/10.1103/PhysRevD.67.103001.

[82] P. A. R. Ade, N. Aghanim, M. Arnaud, M. Ashdown, J. Aumont, C. Baccigalupi, A. J. Banday, R. B. Barreiro, J. G. Bartlett, and et al., Astron. Astrophys. **594**, A13 (2016), URL http://dx.doi.org/10.1051/0004-6361/201525830.

[83] The Astropy Collaboration, Robitaille, Thomas P., Tollerud, Erik J., Greenfield, Perry, Droettboom, Michael, Bray, Erik, Aldcroft, Tom, Davis, Matt, Ginsburg, Adam, Price-Whelan, Adrian M., et al., Astron. Astrophys. **558**, A33 (2013), URL https://doi.org/10.1051/0004-6361/201322068.

[84] The Astropy Collaboration, A. M. Price-Whelan, B. M. Sipőcz, H. M. Günther, P. L. Lim, S. M. Crawford, S. Conseil, D. L. Shupe, M. W. Craig, N. Dencheva, et al., Astron. J. **156**, 123 (2018).

[85] E. Komatsu, K. M. Smith, J. Dunkley, C. L. Bennett, B. Gold, G. Hinshaw, N. Jarosik, D. Larson, M. R. Nolta, L. Page, et al., Astrophys. J. Suppl. Ser. **192**, 18 (2011).

[86] J. F. Navarro, C. S. Frenk, and S. D. M. White, Astrophys. J. **462**, 563 (1996), URL http://dx.doi.org/10.1086/177173.

[87] P. J. McMillan, Mon. Not. R. Astron. Soc. **414**, 2446–2457 (2011), URL http://dx.doi.org/10.1111/j.1365-2966.2011.18564.x.

[88] A. Klypin, H. Zhao, and R. S. Somerville, Astrophys. J. **573**, 597–613 (2002), URL http://dx.doi.org/10.1086/340656.

[89] W. Dehnen, D. E. McLaughlin, and J. Sachania, Mon. Not. R. Astron. Soc. **369**, 1688–1692 (2006), URL http://dx.doi.org/10.1111/j.1365-2966.2006.10404.x.

[90] E. D'Onghia, V. Springel, L. Hernquist, and D. Keres, Astrophys. J. **709**, 1138–1147 (2010), URL http://dx.doi.org/10.1088/0004-637X/709/2/1138.

[91] J. M. Shull, Astrophys. J. **784**, 142 (2014), URL http://dx.doi.org/10.1088/0004-637X/784/2/142.

[92] N. Oo and W.-S. Gan, Int. J. Comput. Commun. Eng. **1**, 200 (2012).

[93] J. J. Blanco-Pillado, K. D. Olum, and X. Siemens, Phys. Lett. B **778**, 392–396 (2018), URL http://dx.doi.org/10.1016/j.physletb.2018.01.050.

[94] L. S. Finn and K. S. Thorne, Phys. Rev. D **62**, 124021 (2000), URL https://link.aps.org/doi/10.1103/PhysRevD.62.124021.

[95] Planck Collaboration, N. Aghanim, Y. Akrami, M. Ashdown, J. Aumont, C. Baccigalupi, M. Ballardini, A. J. Banday, R. B. Barreiro, N. Bartolo, et al., *Planck 2018 results. vi. cosmological parameters* (2018), 1807.06209.

[96] D. V. Martynov, E. D. Hall, B. P. Abbott, R. Abbott, T. D. Abbott, C. Adams, R. X. Adhikari, R. A. Anderson, S. B. Anderson, K. Arai, et al., Phys. Rev. D **93**, 112004 (2016), URL https://link.aps.org/doi/10.1103/PhysRevD.93.112004.

[97] M. G. Jackson, N. T. Jones, and J. Polchinski, J. High Energy Phys. **2005**, 013 (2005).

[98] N. T. Jones, H. Stoica, and S.-H. Tye, Phys. Lett. B **563**, 6 (2003), URL http://www.sciencedirect.com/science/article/pii/S0370269303005926.

[99] M. Sakellariadou, J. Cosmol. Astropart. Phys. **2005**, 003 (2005).

[100] A. Avgoustidis and E. P. S. Shellard, Phys. Rev. D **73**, 041301 (2006), URL https://link.aps.org/doi/10.1103/PhysRevD.73.041301.